Charles University in Prague
Faculty of Mathematics and Physics

DOCTORAL THESIS

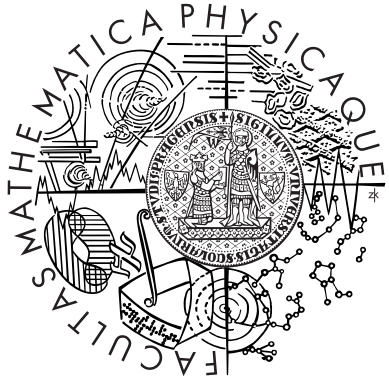

Pavel Řezníček

Measurement of the B_d^0 meson lifetime at ATLAS detector

Institute of Particle and Nuclear Physics

Supervisor of the doctoral thesis: **Dr. Zdeněk Doležal**
Co-supervisor: **Dr. Mária Smižanská**[1]
Study programme: **Physics**
Specialization: **Subnuclear Physics**

Prague 2012

[1]Lancaster University, UK

Univerzita Karlova v Praze
Matematicko-fyzikální fakulta

DISERTAČNÍ PRÁCE

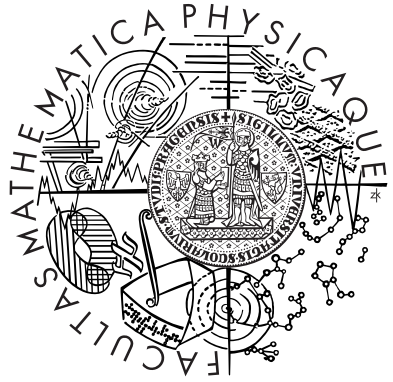

Pavel Řezníček

Měření doby života mesonu B_d^0 na detektoru ATLAS

Ústav částicové a jaderné fyziky

Vedoucí disertační práce: **Doc. RNDr. Zdeněk Doležal, Dr.**
Konzultantka: **RNDr. Mária Smižanská, CSc.**[1]
Studijní program: **Fyzika**
Studijní obor: **Subjaderná fyzika**

Praha 2012

[1]Lancaster University, UK

I would like to thank to my supervisors Zdeněk Doležal and Mária Smižanská for their leadership of my doctoral studies and for all the consultations and also the patience in pushing me to finish the thesis.

I am also very grateful to the members of the Lancaster University and Munich Excellence Cluster group, especially to James Catmore, Alastair Dewhurst, Jochen Schieck and Louise Oakes for the discussions about the analyses.

So does belong many thanks to the present and former members and students of the Institute of Particle and Nuclear Physics MFF UK, especially to Tomáš Davídek, Zbyněk Drásal, Jan and Daniel Scheirch, Peter Kodyš, Peter Kvasnička, Jana Nováková, Honza Brož, Petr Kubík and many others for all the technical, physics and friendly discussions.

Finally I must not forget to mention the great support and patience from my family (including ŠeTe).

Prohlašuji, že jsem tuto disertační práci vypracoval samostatně a výhradně s použitím citovaných pramenů, literatury a dalších odborných zdrojů.

Beru na vědomí, že se na moji práci vztahují práva a povinnosti vyplývající ze zákona č. 121/2000 Sb., autorského zákona v platném znění, zejména skutečnost, že Universita Karlova v Praze má právo na uzavření licenční smlouvy o užití této práce jako školního díla podle §60 odst. 1 autorského zákona.

I declare that I carried out this doctoral thesis independently, and only with the cited sources, literature and other professional sources.

I understand that my work relates to the rights and obligations under the Act No. 121/2000 Coll., the Copyright Act, as amended, in particular the fact that the Charles University in Prague has the right to conclude a license agreement on the use of this work as a school work pursuant to Section 60 paragraph 1 of the Copyright Act.

In Prague, 26th June 2012

Pavel Řezníček

Název práce: Měření doby života mesonu B_d^0 na detektoru ATLAS

Autor: Pavel Řezníček

Katedra (ústav): Ústav částicové a jaderné fyziky

Vedoucí disertační práce: Doc. RNDr. Zdeněk Doležal, Dr.

E-mail vedoucího: Zdenek.Dolezal@mff.cuni.cz

Abstrakt: S využitím dat experimentu ATLAS z proton-protonových srážek o energii 7 TeV (v těžišťovém systému) na urychlovači LHC byla změřena doba života mesonu B_d^0 v rozpadovém kanálu $B_d^0 \to J/\psi K^{*0}$. Hodnota získaná metodou maximální věrohodnosti na souboru dat invariantní hmoty a doby rozpadu zrekonstruovaných B_d^0 mesonů je 1.51 ± 0.04 (stat.) $\pm$ 0.04 (syst.) ps. Pozorováno bylo celkem 2750 ± 90 (stat.) skutečných případů rozpadu $B_d^0 \to J/\psi K^{*0}$. Uvedená metoda také umožnila změřit klidovou hmotu B_d^0 mesonu: 5363.7 ± 1.2 (stat.) MeV. Extrahovné hodnoty doby života i klidové hmoty B_d^0 mesonu se v rámci chyb měření shodují se současnými nejpřesnějšími měřeními, ačkoli dosažená přesnost neumožnujě, aby k nim významně přispěly. Tato práce však byla důležitá k otestování použité metody a k prověření vlastností detektoru ATLAS.

Klíčová slova: CERN, LHC, ATLAS, B-fyzika, B-hadron, Doba života

Title: Measurement of the B_d^0 meson lifetime at ATLAS detector

Author: Pavel Řezníček

Department: Institute of Particle and Nuclear Physics

Supervisor of the doctoral thesis: Dr. Zdeněk Doležal

Supervisor's e-mail address: Zdenek.Dolezal@mff.cuni.cz

Abstract: The lifetime of B_d^0 mesons is determined from their decays $B_d^0 \to J/\psi K^{*0}$ reconstructed in ATLAS experiment at the LHC using pp collision data at a center-of-mass energy of 7 TeV and corresponding to integrated luminosity of 40 pb^{-1}. The lifetime, extracted from the simultaneous unbinned maximum likelihood mass-lifetime fit, is 1.51 ± 0.04 (stat.) ± 0.04 (syst.) ps. A total number of 2750 ± 90 (stat.) signal B_d^0 decays are observed in the measurement, with a fitted B_d^0 mass of 5363.7 ± 1.2 (stat.) MeV. Both the extracted B_d^0 meson mass and lifetime are within the determined errors consistent with the world average values. Although the achieved precision is still significantly lower than the one of the world average value, the measurement successfully tested the feasibility of the fit-method and allowed to cross-check ATLAS detector performance.

Keywords: CERN, LHC, ATLAS, B-physics, B-hadron, Lifetime

Contents

1 Introduction

The Standard Model (SM) is a relativistic quantum gauge field theory of fundamental particles and their interactions. In its current form, it was developed in 1960s and over the years it has been tested by numerous experiments, so far with great success. Except of Higgs boson all the SM particles has been observed. However, although many of the SM predictions have been confirmed with an astonishing precision, there are still several open questions the SM theory does not explain. The SM has currently 19 free parameters. It does not include gravity, does not explain the different masses of fermions, neither number of generations nor the origin of CP violation (CPV).

A number of theories beyond SM were constructed in the attempt to solve these issues. However, due to the precise SM experimental confirmation, they have to be largely compatible with it. Therefore most of these new theories predict for the experimental results only tiny differences w.r.t. to the SM calculations, or predict larger differences but in rare processes. The latest attempt to put the beyond-SM theories under test has been made by the construction of the world largest hadron collider - the LHC with its four dedicated experiments.

This thesis describes my contribution to the tests of SM prediction, namely of the CP violation, using data from the ATLAS experiment at the LHC. Standing just at the beginning of the LHC operation, the work is focused on testing the performance properties relevant for B-decays by measuring physics quantities, such as mass and lifetime of B-meson, that will become part of the high precision measurement of CP violation. The methods of analysis and statistical treatment of data used in current measurements presented in this thesis are similar to those that will be used in CP violation studies. Testing of these methods is important part of preparation.

The analysis in this thesis presents the extraction of $B_d^0 \to J/\psi K^{*0}$ decay from the early ATLAS data and the measurement of the B_d^0 lifetime in this particular decay channel. The analysis is part of the ATLAS B-physics programme, that consists of measurement of production cross sections and production mechanisms of heavy flavors hadrons, and of studies of selected exclusive B-hadron decays.

Due to sharing the decay topology and helicity structure, but at the same time providing significantly larger statistics, the $B_d^0 \to J/\psi K^{*0}$ decay serves as a reference channel and a testing ground for the measurement of $B_s^0 \to J/\psi\phi$ decay channel and for semileptonic rare B-decays (in particular the $B_d^0 \to \mu^+\mu^- K^{*0}$). The study of $B_s^0 \to J/\psi\phi$ decay is of high interest to the particle physicists as it allows the measurement of the B_s^0 mixing phase, which is responsible for the CP violation in this decay channel. Since the size of the CP violation predicted by the Standard Model is small (of the order of $\mathcal{O}(10^{-2})$), any measured larger deviation would be a clear indication of New Physics (NP). The $B_d^0 \to J/\psi K^{*0}$ decay can not only be used for preparing and testing the analysis procedure for $B_s^0 \to J/\psi\phi$, but since the flavour of the B_d^0 meson can be determined on statistical basis from the K^{*0} final state, the B_d^0 decay will also be used for obtaining independently the B-flavour tagging performance.

Lastly, the lifetime measurement is an excellent probe of the performance of the ATLAS detector, especially of the vertex reconstruction.

The content of the thesis is structured in the following: The introduction chapter **1)** presents the ATLAS B-physics programme, with more details provided for the CPV in $B_s^0 \to J/\psi\phi$ for which the B_d^0 lifetime measurement is the direct forerunner. In the chapter **2)**, the ATLAS detector subsystems and the data taking at the LHC are briefly described. The chapter **3)** deals with the ATLAS trigger system, focused on the B-physics trigger algorithms, to which deve-lopment I have contributed, especially in the data-taking monitoring aspects. The next chapter **4)** is introducing the Monte Carlo (MC) simulation machi-nery of the physics processes and of the detector. The chapter **5)** is describing the general analysis scheme and tools used by the B-physics group at ATLAS. I significantly contributed to the development and implementation of the analysis tools. The next two chapters are presenting the main subject of this thesis: the analysis for the $B_d^0 \to J/\psi K^{*0}$ extraction from the data in the chapter **6)**, and the B_d^0 lifetime measurement in the chapter **7)**. As is mentioned in the summary chapter **8)**, the $B_d^0 \to J/\psi K^{*0}$ measurement in 2010 ATLAS data was a joint project with similar $B_s^0 \to J/\psi\phi$ analysis and thus the experience in the analyses were shared within the $B_s^0 \to J/\psi\phi$ team. However, I was responsible for the $B_d^0 \to J/\psi K^{*0}$ measurement and thus have dominant contribution to the described analysis (the only subsections with my smaller contributions are the determinations of the systematics errors connected with the model of the lifetime fit in sections 7.3.1, 7.3.2, 7.3.3 and the appendix B.2). Finally, there are also attached two appendix sections **A)** and **B)**, providing more, mostly technical, details and cross-checks for the analyses in the two main chapters 6) and 7).

Thorough whole the thesis, the usual particle-physics convention of $c = 1$ is used for all the units.

1.1 B-Physics at ATLAS

ATLAS is designed as a general purpose detectors. There is a B-physics dedicated LHCb experiment at the LHC accelerator, but ATLAS can still provide competitive results in some of the B-physics areas, despite a missing kaon/pion separation and worse lifetime resolution at low transverse momenta, where the B-physics dominates. The construction of the ATLAS detector and the luminosity conditions determine the ATLAS B-physics programme. LHCb limits the instantaneous luminosity to $< 2 \cdot 10^{32}$ cm^{-2}s^{-1} in order to keep low-level of background (pile-up interaction, see section 2.1), while ATLAS is running on the maximum luminosity LHC provides. Hence allowing to collect larger statistics, which is in particular important for measurement of decays with very low branching ratios (BR).

The ATLAS B-physics programme covers two main aspect of the heavy flavor physics. First is a measurement of production cross sections and production mechanisms of heavy flavors hadrons, either opened (B-hadrons, Charm hadrons) or hidden (Onia). This programme has been very successful and has lead to interesting new results:

- The charm cross section at the LHC energy is larger than anticipated. Using $D^{*\pm}$, $D^{\pm}$ and $D_s^{\pm}$ mesons, ATLAS measured the weighted mean of the three values calculated from the $D^{*\pm}$, $D^{\pm}$ and $D_s^{\pm}$ cross sections and obtained

a total $c\bar{c}$ cross-section at 7 TeV [1]:

$$\sigma_{c\bar{c}}^{\mathrm{tot}} = 7.13 \pm 0.28(\mathrm{stat.})^{+0.90}_{-0.66}(\mathrm{syst.}) \pm 0.78(\mathrm{lumi.})^{+3.82}_{-1.90}(\mathrm{extr.})\ \mathrm{mb}$$

The measurement is in agreement with both the LHCb and CMS results.

- The B-cross-section has been measured in ATLAS using channel $pp \to B + X \to J/\psi X$ [2]. In fiducial volume of the J/ψ rapidity $|y_{J/\psi}| < 2.4$ and transverse momentum $p_{\mathrm{T}}^{J/\psi} > 7$ TeV the measured value of the cross-section is:

$$\mathrm{BR}(J/\psi \to \mu^+\mu^-) \cdot \sigma(pp \to B + X \to J/\psi) = \\ 23.0 \pm 0.6(\mathrm{stat.}) \pm 2.8(\mathrm{syst.}) \pm 0.2(\mathrm{spin}) \pm 0.8(\mathrm{lumi.})\ \mathrm{nb}$$

- Direct Onia cross-sections of J/ψ and Υ were measured [3] and confirmed predictions of QCD calculations using Colour Octet model.

- ATLAS was also the first experiment to discover existence of the predicted χ_b state and measured its mass: $10.530 \pm 0.005(\mathrm{stat.}) \pm 0.009(\mathrm{syst.})$ GeV [4].

The very successfull series of the B-production measurements are being continued by measurement of polarisations using data collected by ATLAS in 2011 run.

The second major part of B-physics activities in ATLAS are exclusive decays of B-hadrons. Since B-cross-section in the ATLAS fiducial volume: ~ 40 μb (based on the $B \to J/\psi$ measurement above) corresponds to 40 kHz at luminosity of 10^{33} cm^{-2}s^{-1}, it is too large in comparison to what can be recorded (~ 20 Hz). The ATLAS programme is therefore dedicated to channels with two muons in final state: $B^0_{s,d} \to \mu^+\mu^-$ and $B \to J/\psi(\mu^+\mu^-)X$, that are potentially sensitive to contributions from New Physics. On the other hand the di-muon channels have favorite trigger signature and so can be collected efficiently with trigger rates that would correspond to the trigger rate limitations and still give competitive statistics in comparison to LHCb. In comparison with ATLAS, LHCb is covering a forward region, where the B-physics cross section is approximately 2× larger than in ATLAS, e.g. the measured B-cross section at LHCb (in pseudo-rapidy region $2 < \eta < 6$) is $75.3 \pm 5.4(\mathrm{stat.}) \pm 13.0(\mathrm{syst.})$ μb [5]. On the other side LHCb reach of B-physics events is limited by the lower instantaneous luminosity. In B-decays ATLAS has provided (or is working on) these measurements:

- Limit on $B^0_s \to \mu^+\mu^-$ decay branching ratio was measured in ATLAS using 2011 data (2.4 fb^{-1}) [6]:

$$\mathrm{BR}(B^0_s \to \mu^+\mu^-) < 2.2(1.9) \times 10^{-8} \text{ at 95\% (90\%) confidence level.}$$

The Standard Model prediction of the branching ratio is extremely small: $(3.5 \pm 0.3) \cdot 10^{-9}$. However, the process can be substantially enhanced by coupling to non-SM heavy particles and thus any significant excess of the observed $B^0_s \to \mu^+\mu^-$ would be a clear indication of New Physics.

- Using the 2010 data, ATLAS has measured B-mass of all B-hadrons and verified the excellent calibration of p_{T} scale at low-energy tracking. Measurements of B-lifetimes in ATLAS (B^0_d, B^0_s and inclusive $b\bar{b} \to J/\psi X$

in [7,8]) manifested very good calibration of distances in the ATLAS detector and precision of vertexing tools. Both the mass and lifetime measurements were important stage in preparations of ATLAS towards the CPV studies that require a precise measurement of both these variables. This thesis is describing one of these measurements.

- Measurement of semileptonic rare B-decay $B_d^0 \to \mu^+\mu^- K^{*0}$ is under preparation with 2011 data. Forbidden at tree level in the SM, the branching ratio of the decay is of the order of $\sim 10^{-6}$, but with potential of significant contributions of beyond-SM particles to the measured differential cross-section, resp. the angular distribution of the decay products [9].

- CP violation studies in $B_s^0 \to J/\psi\phi$ decay are running using the 2011 data [10]. As this thesis topic was mostly intended as the forerunner of the CPV measurement, the motivation and brief description of the analysis method for the CPV studies is described in the next section.

1.1.1 Measurement of $B_s^0 \to J/\psi\phi$

In the $B_s^0 \to J/\psi\phi$ decay, both the B_s^0 and $\bar{B}_s^0$ can decay to the same final state. This allows for the CP violation to occur through interference between the $B_s^0 \longleftrightarrow \bar{B}_s^0$ mixing and the decay amplitudes. The oscillation frequency of B_s^0 meson mixing is characterized by mass difference Δm_s between "heavy" (B_H) and "light" (B_L) mass eigenstates and by CP-violating phase ϕ_s. In the absence of direct CP violation, the B_H state would correspond exactly to the CP-odd state and B_L to the CP-even. In the Standard Model the phase ϕ_s is predicted to be small and can be related to the CKM quark mixing matrix elements as follows:

$$\phi_s \simeq -2\beta_s = -2 \cdot \arg\left(-\frac{V_{ts}V_{tb}^*}{V_{cs}V_{cb}^*} \right) \tag{1}$$

The value predicted for SM is $\phi_s \simeq -2\beta_s = -0.0368 \pm 0.0018$ rad [11]. However, many New Physics models allows large ϕ_s values while satisfying all existing constraints, including the precisely measured value of the oscillation frequency Δm_s [12,13]. In the $B_s^0 \longleftrightarrow \bar{B}_s^0$ mixing, there is also another interesting physical quantity - the decay width difference $\Delta\Gamma_s = \Gamma_L - \Gamma_H$. The value itself is not expected to be affected by the beyond-SM physics as significantly as the ϕ_s [14], but measuring the value provides a constraint on the ratio of $\Delta\Gamma_s/\Delta m_s$ which has the advantage of being free of most theoretical uncertainties [11].

The CP violating parameters can be extracted from decay-time dependence of angular distribution of the $B_s^0 \to J/\psi(\mu^+\mu^-)\phi(K^+K^-)$ decays. This decay of the pseudo-scalar B_s^0 to the vector-vector final-state results in an admixture of CP-odd and even states, the former corresponding to total angular momentum of 1, and the later to the total angular momentum of 0 or 2. The CP states are separated statistically through the decay time dependence of the decay and angular correlations amongst the final-state particles. The angular distribution of the four final state particles ($K^+K^-\mu^+\mu^-$) is given by three angles, θ_T, ψ_T and φ_T defined in the transversity basis [15]: having x-axis defined as the direction of the ϕ-meson in the J/ψ rest frame and using the K^+K^- plane to define the x-y plane ($p_y(K^+) > 0$), the three transversity angles are:

- θ_T is the angle between $p(\mu^+)$ and the x-y plane in the J/ψ meson rest frame,
- φ_T is the angle between the x-axis and the projection of the μ^+ momentum in the x-y plane, all viewed in the J/ψ meson rest frame,
- ψ_T is the angle between $p(K^+)$ and $-p(J/\psi)$ in the ϕ-meson rest frame.

The measurement of the interesting physics quantities ϕ_s and $\Delta\Gamma_s$ is then based on a simultaneous B_s^0 mass-lifetime-angular fit to the data. The mass-lifetime part of the fit is identical to the method used in this thesis to measured the B_d^0 lifetime.

2 The ATLAS Experiment

ATLAS (A Toroidal LHC ApparatuS) [16, 17] is a general-purpose detector for the Large Hadron Collider (LHC) built in the European Organization for Nuclear Research (CERN). The experiment was designed to cover wide spectrum of possible physics signatures, from precision measurements of the Standard Model parameters to the search for New Physics phenomena, and to operate over the full range of the LHC luminosity conditions.

2.1 The Large Hadron Collider

The Large Hadron Collider is a proton-proton synchrotron, with four collision points devoted for the four main experiments: general-purpose ATLAS and CMS, B-physics focused LHCb, and ALICE dedicated for the study of the heavy ion collisions[1]. The accelerator is built in the longest of the CERN tunnels (reusing tunnel of the LEP experiment ended in 2000), situated near Geneva, 27 km long and with maximum depth of 175 metres. The designed nominal energy of the proton beams is 7 TeV each, providing centre-of-mass energy of 14 TeV. Before being injected into the LHC ring, the beams are produced in the existing CERN accelerator facilities: 50 MeV proton linear accelerators (Linac), 1.4 GeV Proton Synchrotron booster, 26 GeV Proton Synchrotron and finally 6.9 km long 450 GeV Super Proton Synchrotron (SPS). Whole the schema shown in figure 1.

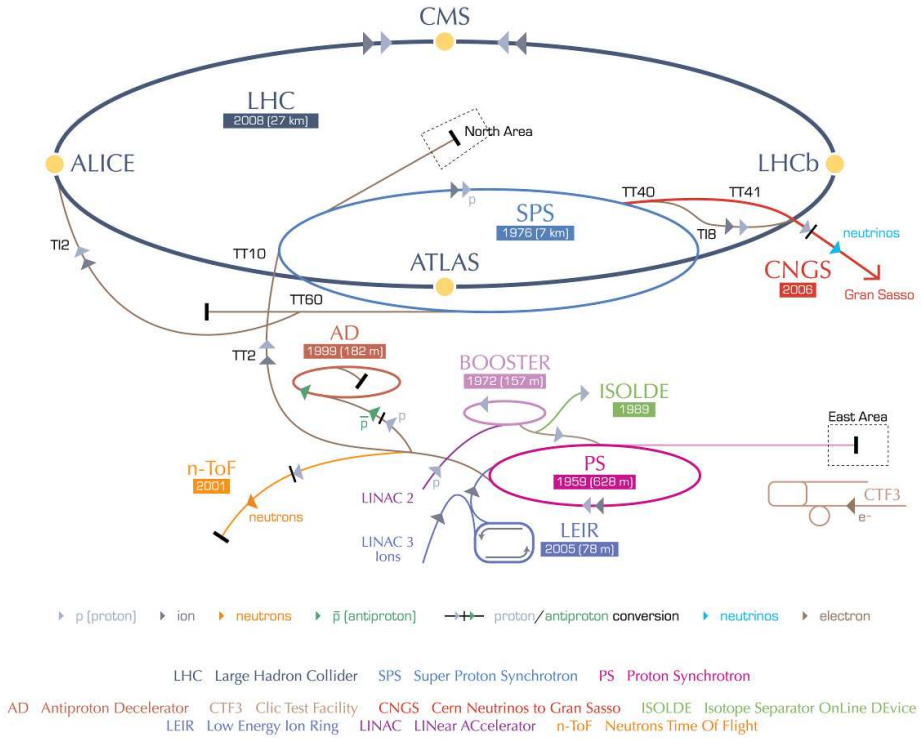

Figure 1: The schema of the CERN accelerator facilities [18].

The proton beams are not continuous fluxes of particles but a system of bunches. At the nominal operation the bunches are $\sim$ 1 m long and colliding in the ex-

[1]This part of the LHC programme is omitted in this section.

periments interaction points with a frequency of 40 MHz. The designed nominal LHC luminosity is 10^{34} cm^{-2}s^{-1}. However, in the initial phases (including the 2010 data taking) the luminosity and also the proton beams energy are kept at lower levels. Because of the density and the amount of protons in each the bunch ($\sim 2.5 \cdot 10^{11}$ protons squeezed to ~ 15 µm in the transverse profile), there occurs more than one proton-proton collision in a bunch crossing. The number of these so called pile-up events is distributed according to Poisson statistics with mean value of ~ 22 expected at the nominal luminosity. The inelastic cross-section for proton-proton collisions at a center of mass energy $\sqrt{s} = 7$ TeV using the ATLAS detector at the Large Hadron Collider was measured [19]: $69.4 \pm 2.4(\text{stat.} + \text{syst.}) \pm 6.9(\text{extrap.})$, out of this the cross section in ATLAS fidutial volume is $60.33 \pm 2.10(\text{stat.} + \text{syst.} + \text{lumi.})$. However, most of these interaction are of low-energy transfer (minimum bias events) producing a number of low-transverse momentum ($\lesssim 0.5$ GeV) hadrons. Therefore each bunch crossing results in hundreds of tracks in the detectors. Signal processes planned to be studied at LHC have significantly smaller cross-sections as show in figure 2. The success of the experiments therefore strongly depend on the detectors trigger systems designed to pickup the interesting events and filter out the rest.

During 2010 data taking period the *pp* collisions were run at centre-of-mass energy of 7 TeV and with instantaneous luminosity reaching up to $\sim 2{\cdot}10^{32}$ cm^{-2}s^{-1}, significantly lower than the nominal design. The delivered integrated luminosity and the achieved peaking instantaneous luminosity are shown in figures 3. The main goal of the ATLAS physics programme at this early was the measurement Standard Model processes (cross-sections etc.) and cross-checks of the detector and analysis methods, as well as tunning of the trigger algorithms (ATLAS trigger system is described in section 3). The B_d^0 lifetime measurement presented in this thesis exactly fits into this programme.

2.2 The ATLAS Detector

The complex ATLAS physics programme include Higgs Boson searches in full possible mass range, search for SUSY, for new heavy gauge bosons, precision measurements of the W-boson and the top quark masses, gauge boson coupling and CP violation and CKM matrix determination. In order to fulfill all these physics goals, the following set of general requirements [17] have to be covered by the detector operation:

- Fast radiation hard-electronics and sensor elements to cope with the experimental conditions at the LHC.
- High detector granularity to handle large particle fluxes and to reduce event overlaps.
- Coverage of large acceptance in pseudorapidity (with almost full azimuthal angle).
- Good charge particle momentum resolution and reconstruction efficiency by the tracking system.
- Vertex detectors placed close to the interaction region for precise secondary vertex reconstruction.

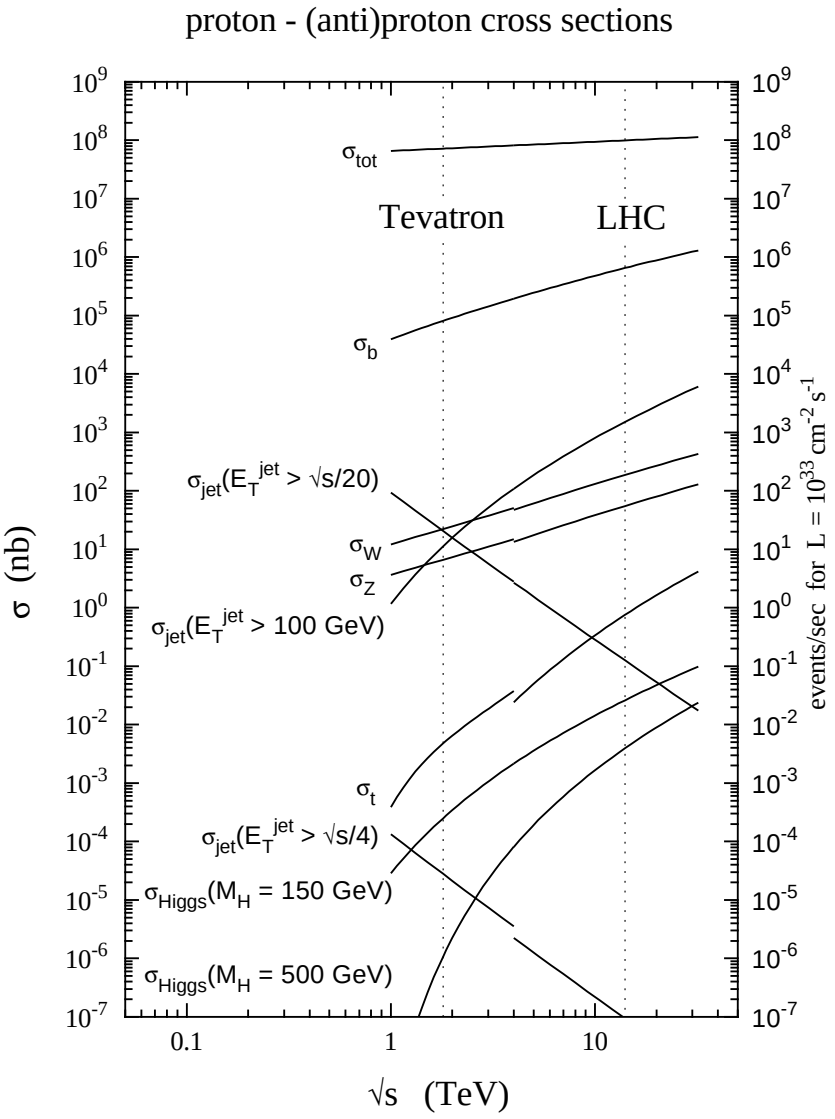

Figure 2: Prediction of the cross-section of the various physics processes in proton-proton collisions as a function of the centre-of-mass energy $\sqrt{s}$. Taken from [20].

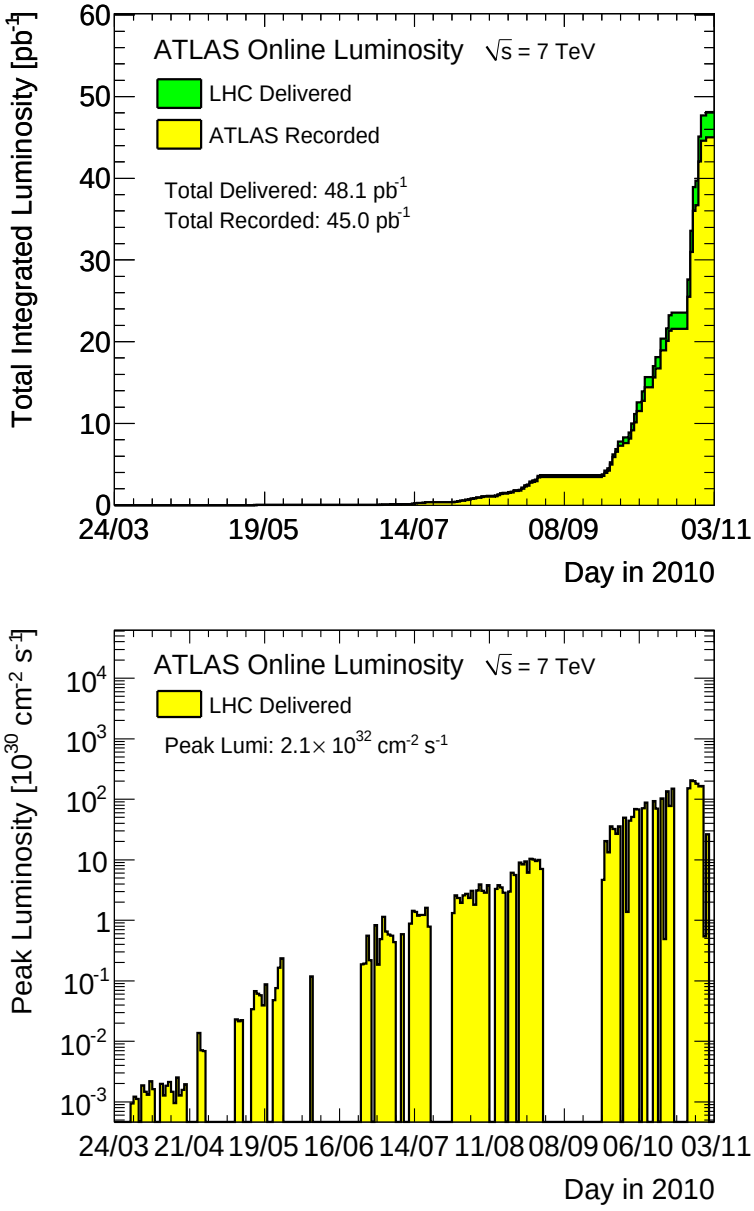

Figure 3: Figures from 2010 data taking period, provided in [21]. The luminosity measurement in 2010 data is described in [22]. Total integrated luminosity delivered by LHC and recorded by ATLAS is shown on the top figure. The inefficiency in ATLAS recording accounts for the turn-on of the high voltage of the tracking and muon detectors and for deadtime or individual problems with a given subdetector that prevent the ATLAS data taking to proceed. The bottom figure presents peak instantaneous luminosity delivered by LHC as monitored by the ATLAS detector.

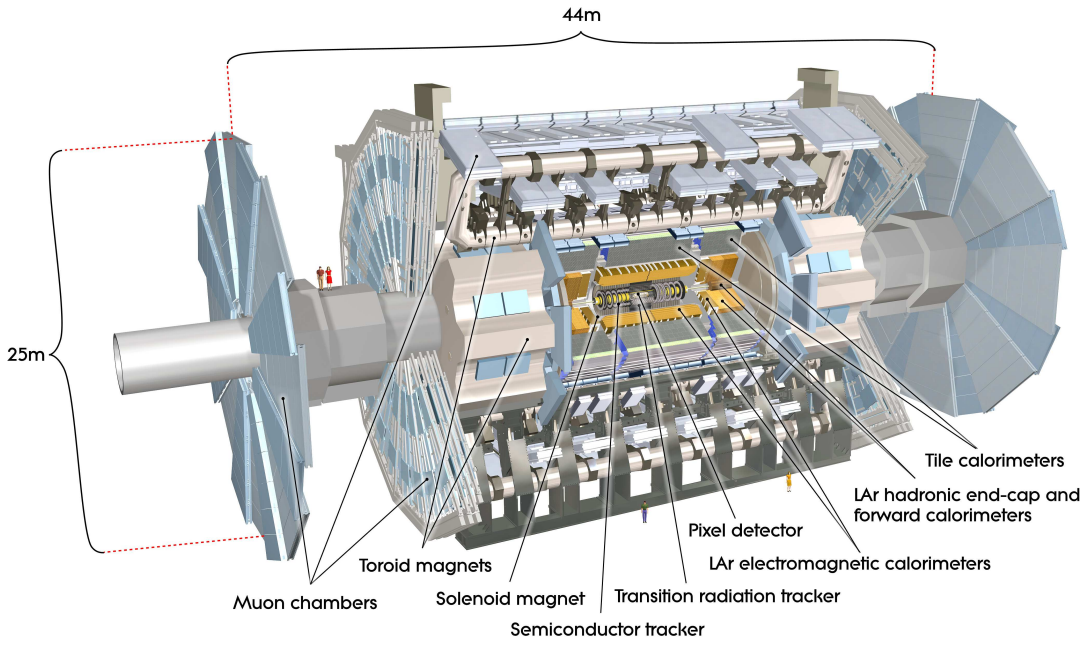

Figure 4: View of the ATLAS detector locating its main subsystems. The detector is 22 m in height, 44 m in length and of overall weight of about 7000 tonnes. Figure provided by [23].

- Very good electromagnetic calorimeters to assure electron and photon identification and measurement, complemented by full-coverage hadronic calorimeters providing accurate jet and missing transverse energy measurements.
- Highly efficient trigger system capable of selecting low transverse-momentum physics objects with sufficient background rejection.

The ATLAS detector layout is shown in figure 4. The detector is forward-backward symmetric with respect to the interaction region. The subsystem closest to the proton-proton (pp) collisions is the Inner Detector (ID), assuring charged tracks reconstruction. This tracking system is consisting of the Pixel detector, the Semiconductor tracker and the Transition Radiation Tracker, all placed in solenoidal magnetic field. The calorimetry system is realized by liquid-argon (LAr) sampling calorimeter and scintillator-tile hadronic calorimeter. The very most outer part of the ATLAS detector consists of the muon spectrometer with air-core toroid magnet system. Further details are provide below in separated sections, extracted from the complete detector description in [17].

2.2.1 Coordinate System and Nomenclature

Since being extensively used in this thesis, the ATLAS coordinate system and basic nomenclature are summarized here. The origin of the coordinate system is in the nominal interaction point, while the beam direction defines the z-axis. The x-y plane is transverse to the beam with positive x-axis defined as pointing from the interaction point to the centre of the LHC ring, and positive y-axis defined as pointing upwards. The side-A of the detector is defined as that with positive z, while side-C as with the negative. The azimuthal angle ϕ is the angle

around z-axis, polar angle θ the angle from the beam axis and the pseudorapidity relates to the polar angle as $\eta = -\ln[\tan(\theta/2)]$. The transverse momentum p_{T}, the transverse energy E_{T} and the missing transverse energy $E_{\mathrm{T}}^{\mathrm{miss}}$ are then defined in the x-y plane. The distance ΔR in the pseudorapidity-azimuthal angle space is defined as $\Delta R = \sqrt{\Delta\eta^2 + \Delta\phi^2}$.

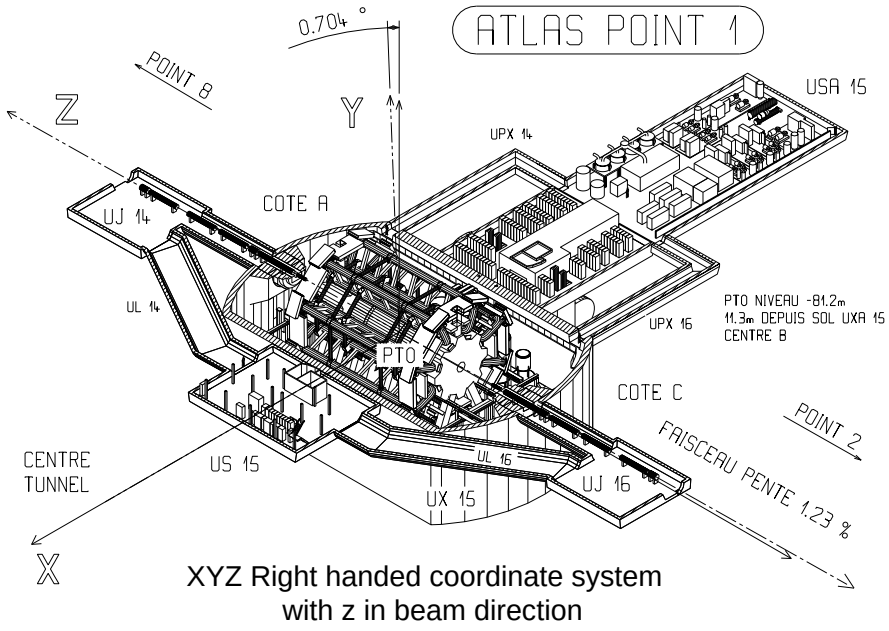

Figure 5: Definition of the ATLAS coordinate system, taken from [24].

2.2.2 Magnet System

The ATLAS magnet system consists of a solenoid and air-core toroids (see figure 6). The 2 T solenoid is positioned in front of the barrel electromagnetic calorimeter, providing tracks bending in the Inner Detector. In order to avoid degrading the electromagnetic calorimeter performance the thickness of the solenoid had to be minimized. The magnetic field for the muon spectrometer is generated by three large air-core toroids. The two end-cap toroids are inserted in the barrel toroid at each end and line up with the central solenoid. The barrel toroid provides 1.5 to 5.5 Tm of bending power in the pseudorapidity range $0 < |\eta| < 1.4$ and the end-cap toroids approximately 1 to 7.5 Tm in the region $1.6 < |\eta| < 2.7$. In the transition region the B-field is combined by magnetic fields of the barrel and of end-cap toroids and thus provides less powerful bending. Each the toroid consists of 8 coils. In order to provide radial overlap and to optimise the bending power at the interface between the two coil systems the end-cap toroid coil system is rotated by 22.50 degrees with respect to the barrel toroid coil system.

2.2.3 Inner Detector

The Inner Detector system, shown in figure 7, provides tracks reconstruction for the ATLAS experiment. It covers pseudorapidity range up to $|\eta| < 2.5$ and is composed of 3 different detectors: semiconductor pixel detector, semiconductor strip detector and transition radiation tracker.

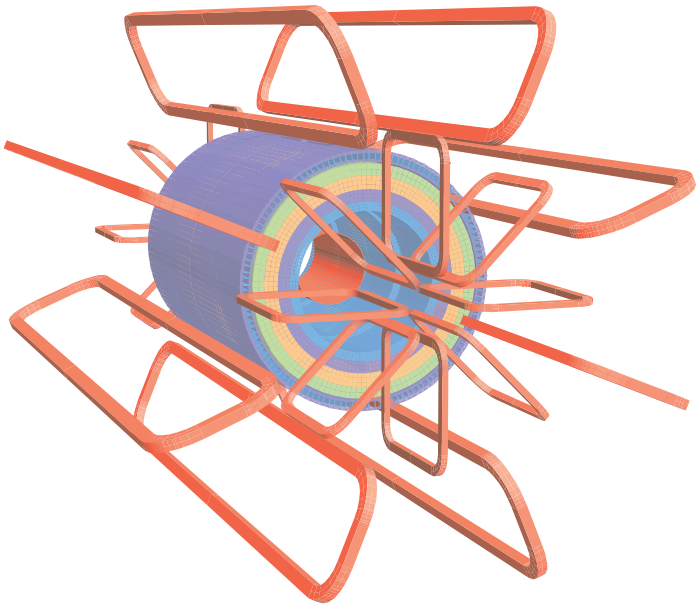

Figure 6: Geometry of magnet windings (red) and tile calorimeter steel (blue, green, orange).

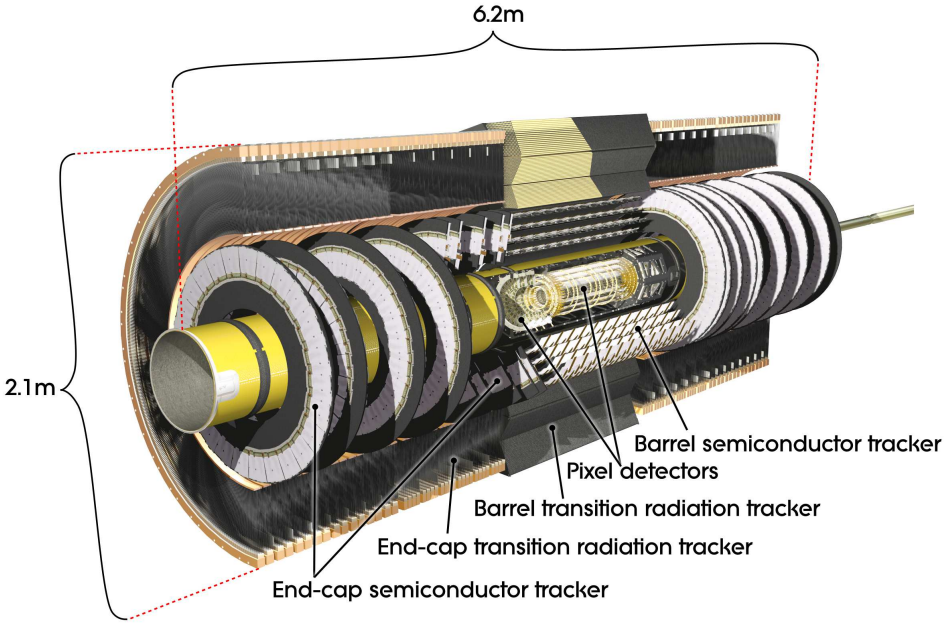

Figure 7: Cut-away view of the ATLAS Inner Detector.

The nearest one to the beam pipe is the Pixel detector. It is designed to provide a very high-granularity and high-precision set of measurements as close to the interaction point as possible. The system consists of 3 layers in the barrel part and 4 disks in the end-cap part, and offers 80 million detector elements, each 50 μm in the $R\phi$ direction and 400 μm in the z. The intrinsic accuracies in the barrel are 10 μm in the R-ϕ plane and 115 μm in z. For the end-cap disks the accuracies are 10 μm (R-ϕ) and 115 μm (R). The maximal radius of the barrel layer is $\sim$ 12 cm, and of the forward disk is $\sim$ 23 cm. However the most important for the secondary vertex reconstruction precision is the layer closest to the beam pipe. This layer is placed only $\sim$ 5 cm from the beam axis.

The Semiconductor Tracker (SCT) is a strip detector consisting of 4 barrel layers and 9 forward wheels. The SCT system is designed to provide 4 precision measurements per track in the intermediate radial range and to contribute to the momentum, impact parameter and vertex position measurement. The four points are assured by eight silicon strip layers grouped into pairs with small angle (40 mrad) stereo strips to measure both coordinates. The strips are $\sim$ 6.4 cm long with typical distance between them of 80 μm (for barrel; in end-cap the strips are running radially, but at similar average distance). The inner most barrel layers is at radius of $\sim$ 30 cm, while the outer most at $\sim$ 51 cm. For the forward wheels the radius range is from $\sim$ 28 cm to $\sim$ 56 cm.

The transition radiation tracker (TRT) provides large number of hits (typically $\sim$ 36) per track using 4 mm diameter straw tubes, with length covering pseudorapidity region up to $|\eta| = 2.0$. The TRT only provides R-ϕ information, reaching an intrinsic accuracy of 130 μm per straw. In the end-cap region, the straws are arranged radially in wheels. The TRT detector is located at radius from $\sim$ 55 cm up to 110 cm. Beside the tracking information, TRT also provides electron identification using the transition radiation in the xenon-based gas mixture of the straw tubes.

The combination of precision trackers at small radii with the TRT at a larger radius gives very robust pattern recognition and high precision in both R-ϕ and z coordinates. Although the TRT has a lower precision per point (compared to the two silicon detectors), the combination of longer measured track length and the relatively large number of points assures significant contribution to the momentum measurement.

2.2.4 Calorimetry

The ATLAS calorimetry system (see figure 8) uses two technologies to assure the electrons and photons energy measurement, the jet reconstruction and the missing transverse energy measurement: liquid argon (LAr) technology, that is intrinsically radiation resistant, and hadronic scintillator tile calorimeter. The full pseudorapidity coverage of the system is $|\eta| < 4.9$.

The electromagnetic (EM) calorimeter is a lead-LAr detector with accordion-shaped kapton electrodes and lead absorber plates over its full coverage. The calorimeter is divided into barrel part ($|\eta| < 1.475$) and two end-cap components ($1.375 < |\eta| < 3.2$). Since the solenoid is placed in front of the system, a presampler detector is used in $|\eta| < 1.8$ region to correct for the energy lost by electrons and photons upstream of the calorimeter.

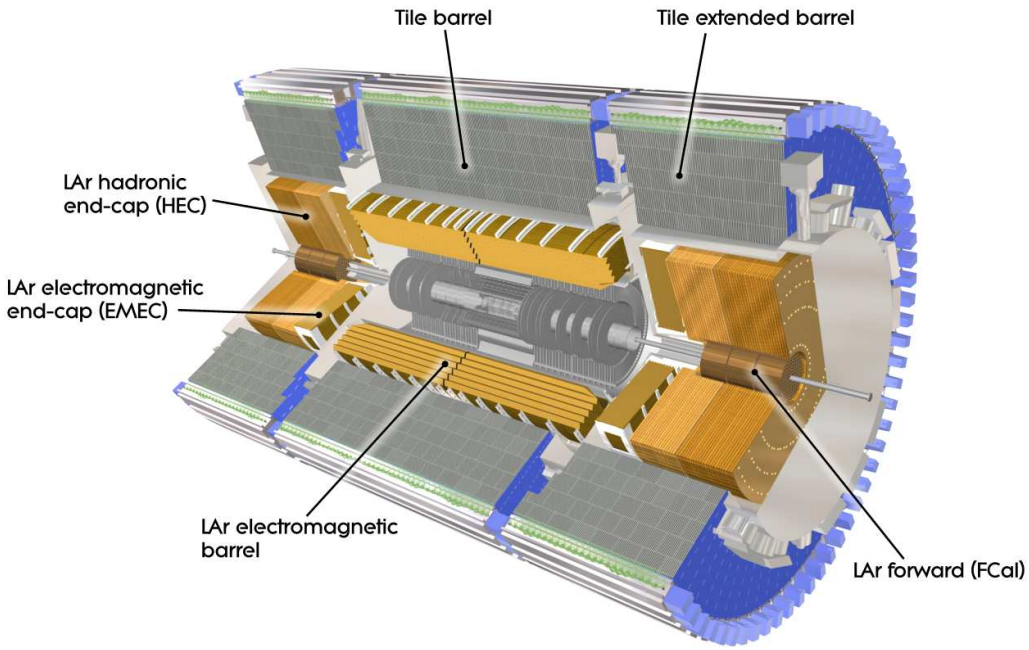

Figure 8: Cut-away view of the ATLAS calorimeter system.

The hadron calorimeter is placed directly outside the EM calorimeter envelope. In the barrel region up to $|\eta| < 1.7$ the tile calorimeter is used, made up of a barrel and two extended barrel sections. The detector is a sampling calorimeter using steel as the absorber and scintillating tiles as the active material. At high η region ($1.5 < |\eta| < 4.9$), the hadronic calorimetry is composed of end-cap and forward detector. These are closer to the beam and thus using the LAr technology to assure radiation hardness.

The calorimeters must provide not only the good coverage of the electromagnetic and hadronic showers, but must also limit punch-through into the muon system. Therefore the calorimeter depth is an important parameter. The total thickness of the EM calorimeter is > 22 radiation lengths (X_0) in the barrel and $> 24 \cdot X_0$ in the end-caps. To provide good resolution for high energy jets, the thickness of the active calorimeter was designed to ~ 9.7 of the interaction length (λ). The total thickness including outer support structures is $\sim 11 \cdot \lambda$, sufficiently reducing the punch-through to the muon detectors and, together with the large η coverage, assuring a good $E_{\mathrm{T}}^{\mathrm{miss}}$ measurement.

2.2.5 Muon Detectors

The ATLAS muon detector system is shown in figure 9. The muon momentum determination is based on deflection of the tracks in the superconducting air-core toroid magnets and measured by separate muon chambers devoted for trigger and high-precision tracking. In the barrel region, the tracks are measured using chambers arranged in three cylindrical layers around the beam axis, while in the transition and end-cap regions, the chambers are installed in planes perpendicular to the beam, and also in three layers.

The precision measurement detectors are realized by Monitored Drift Tubes

(MDT's) in the barrel region with each wire resolution of about 80 μm. In the end-cap Cathode Strip Chambers (CSC's, which are multiwire proportional chambers with cathodes segmented into strips) are used, providing spatial resolution less than $\lesssim 100$ μm. The total pseudorapidity coverage of the precision chambers is $|\eta| < 2.7$.

The trigger system covers the pseudorapidity range $|\eta| < 2.4$. Resistive Plate Chambers (RPC's) are used in the barrel and Thin Gap Chambers (TGC's) in the end-cap regions. The trigger chambers for the muon spectrometer serve a threefold purpose: provide bunch-crossing identification, provide well-defined p_{T} thresholds, and measure the muon coordinate in the direction orthogonal to the one determined by the precision-tracking chambers.

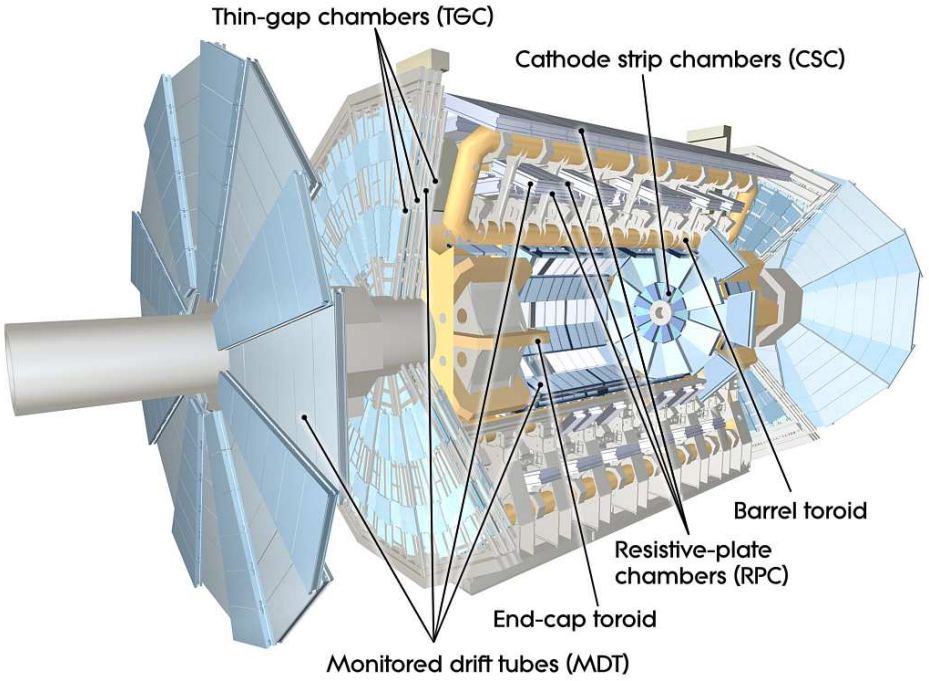

Figure 9: Cut-away view of the ATLAS muon system.

3 ATLAS Trigger

The ATLAS trigger system [17, 25, 26] has to reduce the collision rate of 40 MHz down to $\sim$ 200 Hz rate of the data storage for physics analyses. Therefore it has to provide $\sim 10^5$ rejection while keeping the high efficiency for the events of interest.

A simplified scheme of the trigger system is shown in figure 10. The trigger system has a three level structure: *Level 1* (L1), *Level 2* (L2) and *Event Filter* (EF), each level refining the decision of the previous one. While the first one is hardware based, the other two - together called *High Level Trigger* (HLT) - are filtering events using the ATLAS software framework.

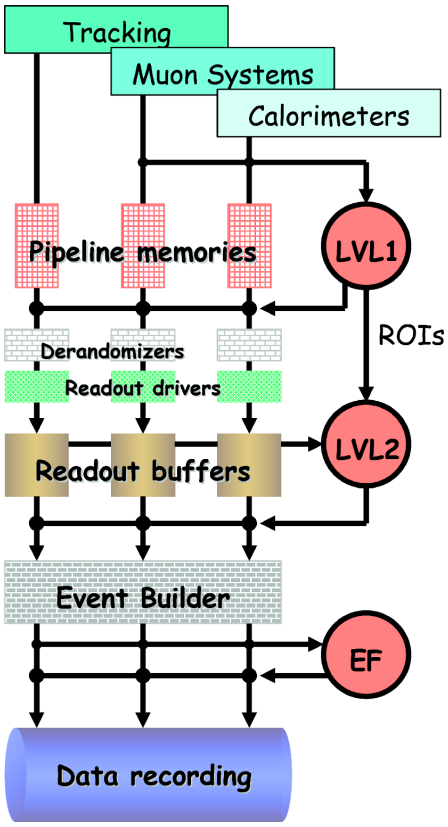

Figure 10: Scheme of the ATLAS trigger system.

The L1 trigger searches for signatures of high transverse-momentum muons, electrons, photons, jets, and τ-leptons decaying into hadrons, as well as large missing and total transverse energy. The corresponding selections are based on information from a subset of the detectors - those that are fast, but less precise. The trigger is implemented in custom programmable electronics, allowing to adopt the selection criteria to the changing luminosity conditions and physics requirements. High transverse-momentum muons are identified using trigger chambers in the barrel and end-cap regions of the spectrometer (TGC's and RPC's). Calorimeter selections are based on reduced-granularity information from all the calorimeters. The L1 decision has to be made in less than 2.5 μs. During the time, the data (from all the detectors) are kept in pipeline memories. Results from the L1 muon and calorimeter triggers are processed by the central trigger processor, which also makes combinations of the decisions, building up

an L1 trigger menu. The number of the items in the L1 menu is around 200 (varying with the physics requirements in different data periods).

In each event, the L1 trigger defines one or more Regions-of-Interest (RoI's), which are geographical coordinates in η and ϕ of those regions within the detector where the L1 selection process has found interesting signatures. The RoI's are accompanied with the information about the type of the observed interesting features and about the criteria they passed - a threshold on the (transverse) momentum or the deposited energy, and/or isolation condition. This information is then used by the subsequent L2 and EF trigger levels. The maximum output acceptance rate of the L1 trigger is ~ 75 kHz.

At L2 further event selection is based on the L1 RoIs. The L2 algorithm constructs an RoI window around the L1 seeds. Size of the window depends on the trigger type object. Data are read from all subsystems at full granularity (including Inner Detector tracking), but only in these RoI windows. This mechanism significantly reduces both the processing times and the required data bandwidth ($\sim 2\,\%$ of the full event information). L2 then performs a refined analysis of the L1 features with the fine-grained detector data and more optimal calibrations to provide results with improved resolution. For each the RoI and for some of their combinations a sequence of L2 algorithms is executed and a new set of selection criteria is used to determine which objects to leave for further analysis. The average L2 processing time is 40 ms and the accepted event rate gets reduced to 2 kHz.

The final EF level also works in the seeded mode, but has access to the full detector data. While L2 selection algorithms are optimized for timing performance, EF uses offline-like analysis tools for further events filtering. The EF algorithms needs several seconds for processing. Gaining from the complex pattern recognition algorithms and calibrations developed for offline processing allows additional events rejection. The output rate is ~ 200 Hz.

The HLT menu consists of around 700 types of different algorithms and their configurations (called L1-L2-EF trigger chains). Because of the limited rate for the data storage, the bandwidth is well balanced for the various ATLAS physics groups. Part of the trigger chains is devoted for calibrations and efficiency measurements. These are consisting of either dedicated supporting trigger algorithms, or by reusing the physics-oriented algorithms but with looser criteria in the selection, or by having chains configured in passthrough mode, when a trigger algorithm is run and its result stored, but its selection decision is ignored and the event is always passed for further processing. In order not to consume too much of the data bandwidth with these supporting trigger chains, their relative contribution is limited by prescaling: only every n-th decision is taken into account, others are ignored as if the particular chains was not running at all. The passthrough mode and prescaling can be applied on any of the three trigger levels. The prescaling is often used also for the main physics triggers as the basic feature for adopting the trigger configuration to the changing luminosity conditions during data-taking.

3.1 B-Physics Triggers

ATLAS can write to permanent storage 200 events per second and the trigger rate dedicated to B-physics is typically 20 Hz. From the values of cross sections from B-physics and total inelastic one (described in section 1.1), it is clear that B-triggers have two main challenges: first select B-physics channels out of inelastic events, and second select B-physics events of interest, since even the B-cross-section is too large to be recorded. The B-physics programme is thus focused on the decay channels that can be clearly distinguished in ATLAS trigger system. The $b\bar{b}$ events are of relatively low-p_{T} scale w.r.t. ATLAS sub-detectors genuine thresholds and compared to other processes studied in ATLAS - B-hadron decays daughter tracks have p_{T} of few GeV; the calorimetry information would thus be dominated by background. Triggering B-hadron decays to hadronic and/or electron final states is therefore possible only at very low luminosities at the start of LHC running. ATLAS B-physics and trigger is thus mostly relying on muonic final states, namely the ones containing $J/\psi \to \mu^+\mu^-$.

The B-trigger system is composed of algorithms searching for the following physics processes or signatures:

- **Single-muon or two-muons** with various p_{T} thresholds. Due to their high rate can only be used at low luminosity or be highly prescaled. They mostly serve as control triggers for calibration and efficiency measurements.
- **Di-muon vertex.** This is the main type of trigger for the ATLAS B-physics. It is described in details in the next section.
- **Multi-muon vertex.** Devoted for $\mu + J/\psi$ (b-quarks correlations studies) and multi-J/ψ events.
- $\boldsymbol{B \to \mu^+\mu^- X}$ **reconstruction.** Trigger used for semileptonic rare B-hadron decays $B \to \mu^+\mu^- X$. Beside the di-muon vertex the trigger algorithm reconstructs also the B-vertex by searching for particles like K^{*0} or ϕ and combining them with the di-muon candidate. This additional requirement provides further rejection to allow to keep the wide non-resonant $\mu^+\mu^-$ mass window of the rare decays.
- $\boldsymbol{J/\psi \to e^+e^-}$ **signature.** Due to high rate it is only usable at low luminosity. These events are intended for cross-checks of the $J/\psi \to \mu^+\mu^-$ analysis.
- $\boldsymbol{D_s \to \phi\pi}$ **plus single-muon signature.** Again usable only at low luminosity. Devoted for $B_s^0 \to D_s(\phi\pi)X$ decays. Purely hadronic signature would not provide enough rejection, which is why a single muon is also required (can come from the opposite-side B-hadron decay, increasing the probability that it is a $b\bar{b}$ event which is picked up).

3.1.1 Di-Muon B-Physics Triggers

A requirement of two muon candidates with certain p_{T} thresholds and originating in a common vertex is the basis of the main B-physics triggers at ATLAS.

There are 4 types of these di-muon B-trigger algorithms. They are tuned for different luminosity levels and in the algorithms by imposing different requirements on the muon identification. Simple schema of the four algorithms is shown in figures 11.

Topological di-muon trigger is the basic algorithm for the nominal luminosities. At L1 it requires two muon signatures. L2 confirms the two muons via precision chambers (*muFast* algorithm [26]), producing corresponding muon spectrometer (MS) track. *IDSCAN* [26] algorithm is then used to reconstruct Inner Detector tracks within the muon L1 RoIs. Further refining of the muons track parameters is achieved by matching and combining the ID and MS tracks (using *muComb* algorithm [26]). However, due to the low-p_{T} nature of the $b\bar{b}$ events, it is the ID parameters that dominates the precision. In next step at L2 the two muons are fitted into a common vertex using a fast vertexing tool based on Kalman filter. An event is allowed for further processing if it passes the selections on the di-muon vertex quality and if the invariant mass of the two muons is within a preselected interval. The EF level copies the procedure that has been performed at L2, but getting use of the tools developed for offline analysis. Because of the L1 and L2 requirements, the topological triggers efficiently pick up events with each muon p_{T} above ~ 4 GeV (muons below this threshold hardly reaches the ATLAS muon detectors due to energy loss in the calorimetry system and do not have enough momentum to pass through all the muon detector layers to form a MS track).

***TrigDiMuon* trigger** is designed for starting LHC luminosities. The L1 signature is a single muon. At L2 the series of steps already described above is used to confirm the L1 measurement and produce combined ID+MS muon track (primary muon). In order to identify the second muon, the following procedure (*TrigDiMuon* algorithm) is applied [26]: The *IDSCAN* tracks reconstruction is run in a extended region around the RoI. The size of the region is $\Delta\eta \times \Delta\phi = 0.75 \times 0.75$. Since the trigger was primarily designed for J/ψ signatures, the size of region was tuned so that there is 92 % probability to include the second J/ψ muon in it (the percentage calculated assuming the p_{T} of the primary muon is greater than 6 GeV and the second one greater than 3 GeV). The *TrigDiMuon* algorithm then combines each found opposite charged ID track with the primary muon. If a pair fulfills certain invariant mass condition (depending on the current trigger chain configuration), the ID track is extrapolated to the muon spectrometer (accounting for the solenoidal and toroidal magnetic field) to confirm whether it is a potential muon candidate or not. This confirmation is realized by a cut on number of muon detector (MDT) hits around the extrapolated ID track (within precision varying with η direction of the tracks). The di-muon candidates are required to be within a certain invariant mass window and eventually are fitted into a common vertex with a quality cut applied. The EF part of the code relies on the offline tools to identify the muon pair within the extended region around the L1 RoI. Similarly as in the topological trigger the opposite charge muon pairs have to sit in a invariant mass window and are required to originate from a common vertex by passing a vertex fit of certain quality. The L2 part of the algorithm has the advantage of being capable to identify low-p_{T} muons (starting from ~ 2.5 GeV) that do not traverse through whole the ATLAS muon system. Because of lower rejection power than the topological

triggers, the *TrigDiMuon* triggers are at higher luminosities configured with higher p_{T} threshold on the primary muon, picking up specific class of di-muon events with highly asymmetric muon parameters (corresponding to $J/\psi \to \mu^+\mu^-$ decays kinematics where one muon tend to follow the original J/ψ momentum).

Muon+track trigger is developed for muon efficiency measurement via tag-and-probe method [27] (gets use of clean J/ψ signatures in ATLAS allowing muon-detectors free muon identification). This muon+track again requires just a single muon at L1 and the muon is confirmed at L2. Di-muon pairs are then combined from opposite charge tracks (reconstructed in the enhance L1 RoI), where one track is required to match the L1 muon by a simple opening angle cut: $\Delta\eta < 0.1$ and $\Delta\Phi < 0.1$. There is also a p_{T} threshold imposed on both the tracks of the di-muon pairs, 4 GeV on the L1 matched muon track and $(2-4)$ GeV on the other track. Similarly as in the previous cases the di-muon pairs have to have invariant mass in a certain window and are tested on originating from a common vertex. The EF procedure copies the L2 algorithm.

Full-scan trigger is a special configuration of either the *TrigDiMuon* or the muon+track trigger allowing larger di-muon opening angles. This is achieved by L2 and EF ID tracks reconstruction in the full Inner Detector volume instead of just in the enlarged L1 RoIs. Besides for calibration purposes, the trigger is useful for collecting $\Upsilon \to \mu^+\mu^-$ decays that in non-negligible fraction decay back-to-back in ATLAS. However, due to larger requirement on the HLT processing time and high rates, the full-scan triggers have to be prescaled or completely off at high luminosities (basically not an issue in 2010 data taking, but later).

3.1.2 Di-Muon B-Physics Triggers Configurations

Each the described di-muon algorithm exists in several configurations. The basic configuration option is the p_{T} threshold of the muon track(s) connected with the L1 decision. These thresholds are pre-programmed in the L1 hardware. For the B-physics triggers the only used L1 muon p_{T} thresholds during 2010 data taking were 4 GeV and 6 GeV (and their combination in case of topological triggers).

The second most used configuration is the selected di-muon invariant mass window. The following mass windows were used:

- $(2.5-4.3)$ GeV: devoted for J/ψ events,
- $(8.0-12.0)$ GeV: devoted for Υ events,
- $(4.0-8.5)$ GeV: rare $B^0_{s,d} \to \mu^+\mu^-$ decay window,
- $(1.5-14.0)$ GeV: mass window covering the whole B-physics region, including non-resonant semileptonic rare B-decays $B \to \mu^+\mu^- X$.

The intervals are chosen accounting for the mass resolution at L2 trigger level. Although the last region covers all the others, the reason for keeping also the separated mass windows is that the full-region trigger will earlier reach the point where its rate is too high and the trigger needs to get prescaled, while the ones with the separated mass windows covering the most important regions can still

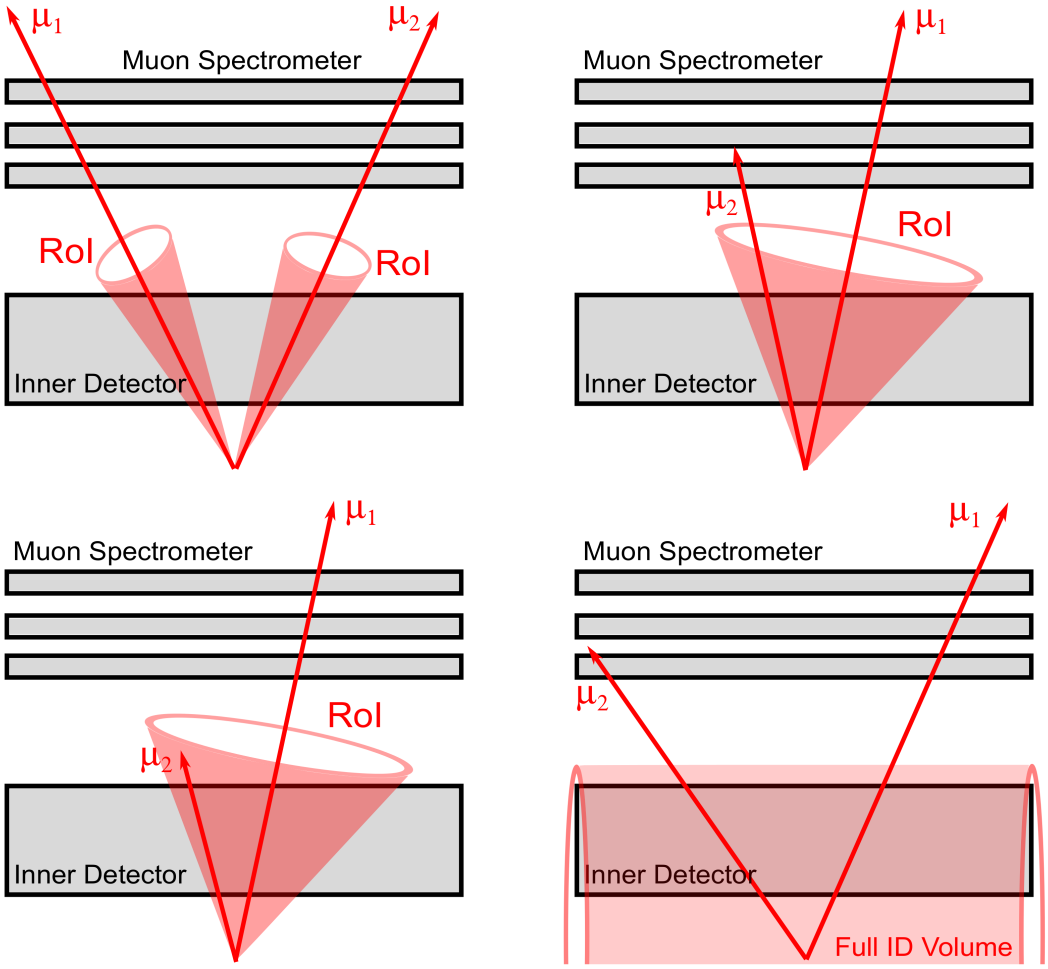

Figure 11: Schema of the B-physics di-muon trigger algorithms: topological (top left), *TrigDiMuon* (top right), muon+track (bottom left) and full-scan *TrigDiMuon* variant (bottom right). The muonic tracks reach in the detectors represents the minimal requirement on the particular muon candidate (e.g. the second muon in the muon+track trigger can also traverse through whole the muon spectrometer).

be fully running. The small overlaps between the first three mass windows allows cross-checks and determining the relative normalization of the data yields collected by the three triggers.

There are also number of other specific configurations using alternative muon identification algorithms at HLT, using alternative tracking code, or applying looser or no vertexing requirements as well as muons opposite charge condition. Some of these are more in more details described at the end of appendix A.3. This appendix also shows the naming convention of the various triggers as used in the analysis.

4 Monte Carlo Simulations

An essential part of the data analysis is the preparation of the analysis strategy using Monte Carlo (MC) physics and detector simulations. Whole the simulation machinery is a complex process which can be decomposed into several steps. At first the studied physics processes, including the interested signal and expected backgrounds, are generated at purely particle level - simulating the pp collision and all subsequent processes as hadronization and particle decays up to the level of real particles passing through the volume of the detector. At the next step, the detector response to the passing particles is modeled, resulting in a set of digital signals as would be seen in real collision. This allows to apply standard real data reconstruction and analysis algorithms, but in addition information about the particle-level origin of the reconstructed objects is provided.

Due to the time and disk-space consumption of the simulations, they are in the ATLAS experiment organized in so called simulation campaigns. The campaigns are specific in the tunning of the MC particle generators (e.g. tunned to the latest results from the LHC and also other experiments) and in the version of the ATLAS reconstruction software (including e.g. updated detector geometry). The simulations used in this thesis were generated during MC10 simulation campaign [28,29], using the same versions of the reconstruction tools as for the Data 2010 processing and with MC particle generators tunning based on the ATLAS measurements in 2009 and early 2010 data taking.

The main steps of the MC simulation chain are described in the next subsections.

4.1 Event Generators

The B-physics processes at ATLAS as simulated using Pythia6 [30] event generator. But because of the large amount of background processes in the pp collisions, using the generator as is would result in unrealistic CPU requirements. In Pythia6, there are three mechanisms leading to a b-quark production. They are classified as flavour creation ($gg \to b\bar{b}$, $qq \to b\bar{b}$), flavour excitation ($gb \to gb$) and gluon splitting ($g \to b\bar{b}$) as illustrated in figure 12. If all the processes containing the mechanisms above are switched on, the fraction of $b\bar{b}$ quarks pair in the pp collisions is only of $\sim 1\,\%$. Moreover the studied signal processes are usually low-branching ratio (BR) exclusive decays. And finally, it is envisaged to pass to the detector simulation only events with the signal B-hadron decay within the ATLAS detector acceptance (in means of pseudorapidity and minimal transverse momenta of the final state daughter particles). To speed up the generation, the obvious method would be to boost the probability of the $b\bar{b}$ production. Although there is such an option in Pythia6, it was found out it impacts the resulting cross-section and p_{T} spectra so seriously that it cannot be reasonably used [31] for proper MC studies.

Therefore the repeated hadronization approach was implemented in ATLAS Pythia wrapper called *PythiaB* [31]. It combines the fact that the most CPU time consuming is the parton-level simulation, with the usually very high filtering factor for the desired signal final state. The repeated hadronization algorithm clones the generated parton-level event record n-times (n is driven by

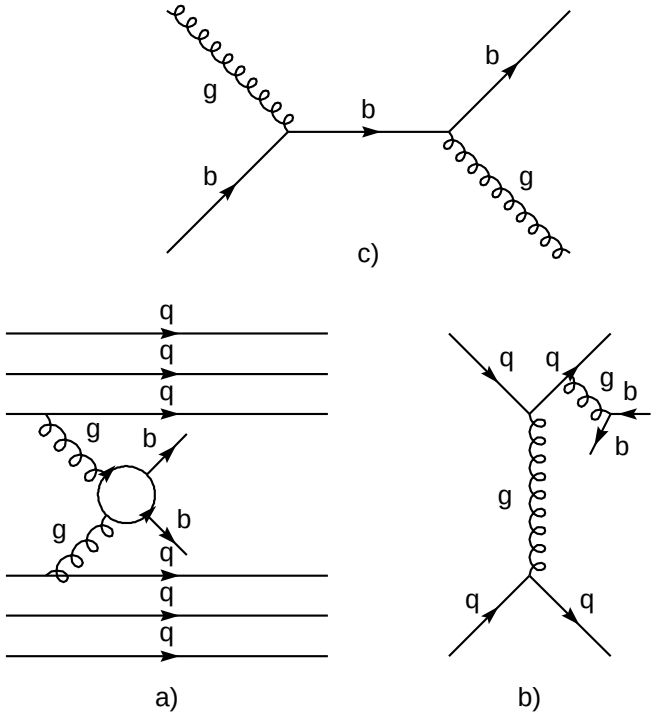

Figure 12: The b-quark production mechanisms in Pythia6: a) flavour creation (gluon-gluon fusion), b) gluon splitting, c) flavour excitation. Figure from [32].

user) and so lets it to be n-times hadronized as if these were completely independent events. To avoid biasing the MC sample, the user selection of n should be of such value so that in average the number of events passing the final-state filtering is close to unity. The *PythiaB* algorithm in addition introduces a simple mechanism for forcing a concrete exclusive B-decay final state, but leaving all other B-hadrons in the event to decay freely. Both these mechanisms greatly improves the efficiency of the requested events generation. The event filtering based on the daughter tracks p_{T} and η is also included in the algorithm. To improve the efficiency also here, it is possible to cut the p_{T} of the hard scattering process in Pythia and eventually preselect events with certain p_{T} and η of the b- or $\bar{b}$-quark.

The ATLAS B-physics group has also implemented an interface to *EvtGen* [33], which is a decay tool widely used in the B-physics dedicated experiments. This tool takes the complex amplitudes of the particle decays and ensembles the total decay (not matter how complex) amplitude before calculating the decay probability. This approach not only simplifies the task of introducing new complex decay models, but most importantly retains the cross-terms in the decay sequences, which are lost in the conventional probability-based generators. The *EvtGen* is just a decayer, not capable of generating the primary interaction. Therefore it needs to be run after Pythia(B) event generation and hadronization.

The MC signal and background samples used in this thesis (table 1) were produced by the *PythiaB* generator only.

4.2 Detector Response Simulation

At the first step of the detector response simulation, the particles from the MC generator(s) are passed through the detector and the energy deposits in the various subdetectors are determined using Geant4 package [34, 35, 36]. The Geant4 simulates all possible interactions of the generated particles with the detector material and thus results not only in the energy deposits, but also in the creation of secondary particles as delta-electrons, full electromagnetic showers and particles from nuclear interactions. Of course the simulation takes into account the B-field generated by the ATLAS magnet systems.

More specific part is then the simulation of the detector electronics in response to the energy deposits in the sensitive parts of the detector. This so called digitization [37] is developed separately for each sub-detector system, going to different levels of the precision of the simulation of the real physics processes in the material and electronics. The digitization algorithms were thoroughly tested (and tuned) in beam tests during the ATLAS subdetectors construction. The product of the digitization process is a collection of so called *digits* - the very basic signal quantities that can be converted to raw real-data like output.

The MC generators usually simulate just a single pp collision. However, as was already mentioned, there are expected ~ 22 pile-up events per each bunch crossing. In order to include this effect into the simulation of the signal processes and to reduce needed CPU power, there are large datasets of minimum bias events pre-simulated and digitized. These large datasets are then combined with the physics samples at the level of the *digits* and in the relative ratio corresponding to the simulated luminosity conditions.

4.3 Reconstruction and Analysis of Simulated Events

The reconstruction and analysis algorithms are basically working the same with the real and simulated data. However, the MC simulation allows to determine which generator particle contributed to which signal in the detector, and thus to associate them with the reconstructed Analysis Objects Data (see section 5). This allows to identify the reconstructed signal B-hadron decays and eventually to study the composition of the background events in the analysis. To make the simulation realistic, the MC events are also required to pass through similar calibration and alignment procedures as the real data.

5 Computing at the ATLAS Experiment

The analysis tools used for the study presented in this thesis are implemented within ATLAS software framework Athena [37]. These tools and analysis principles are in details described in my proceedings [38] from the CHEP 2007 conference [39] and thus the content of this chapter is largely reusing my original text.

The analysis runs on reconstructed data specifically devoted for physics analysis - Analysis Object Data (AOD), the final product of the ATLAS reconstruction chain [37]. The chain starts with RAW data (the output of the final stage of the ATLAS High Level Trigger) that are reconstructed producing Event Summary Data (ESD), intended to make access to RAW data unnecessary for most physics applications. The AOD are then derived from ESD, representing reduced event information suitable for analysis, such as reconstructed particles and b-tagging information. Along side with AOD also Tag Data (TAG) are extracted collecting event-level metadata to support an efficient identification and selection of the events of interest to a given analysis. All the data from the ATLAS detector are distributed using a hierarchical four-tier structure of facilities ([37] p. 8) connected by a Grid infrastructure. Both AOD and ESD are held on Tier-1 facilities, while AOD are copied to Tier-2 sites that are accessible for physicists to perform the analyses.

The Tier-2 sites also provide all the required simulation capacity for the experiment. The Monte Carlo simulations consisting of the event generation, the Geant4 simulations of the particles' passage through the ATLAS detector and finally the detector response simulation (as described in the previous section 4) uses the output *digit* to produce ESD and the rest of the chain is similar as with real data.

To avoid large amounts of data being copied over to local computers, the analysis software is sent to the data on the Tier-2 sites. The jobs are distributed via a Grid middleware to which several interfaces exist, most used Ganga [40] and Panda [41].

5.1 ATLAS Software Framework

Athena [37], the ATLAS software framework, primarily uses the object-oriented C++. The Athena applications are built up from a sequence of dynamically loadable components driven by Python configuration scripts. The framework provides common data-processing support, with major components including list of tools (e.g. vertexing tools), services (e.g. logging facility, histogram and ntuple services), data representation converters, common interfaces for per-event processing algorithms etc., all driven by an application manager. The B-physics analyses [42] are coded in pure C++. The main processing classes are derived from an Athena algorithm extended by robust handling of ROOT-ntuple output [43].

5.2 B-Physics Analysis Software

At the LHC the B-physics programme focuses on the study of exclusive decay channels, therefore the analysis is characterized by many different topologies

and constraints. In order to avoid duplicated efforts, common tools, data structures and calculations were collected and unified over all the B-physics channels. The main task in the B-physics analysis is to identify a B-hadron decay chain typically consisting of a cascade of several vertices, like the topologies depicted in the following sketches:

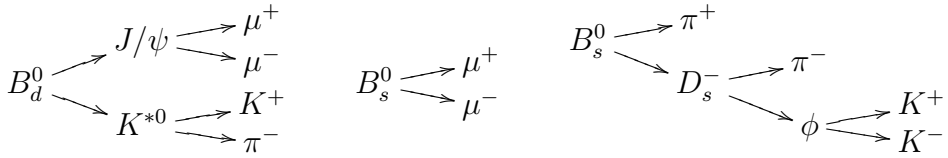

This requires the usage of an offline vertex finder, a management of the combinatorics of tracks to form the candidates of the elements of the decay chain and an extraction of various properties of the fitted particle-like objects. In order to check the efficiencies, performance and sources of background, the MC truth and its associations to the reconstructed objects are used and there were tools developed to ease the usage of these relations, like an extraction of the correct signal tracks of the whole decay topology.

Since the B-physics analysis suite is a part of the Athena software framework, the Athena services are used to access the objects stored in the AOD files. Presently, the B-physics analyses rely on reconstructed Inner Detector tracks, combined muon and electron objects, trigger decision information, reconstructed primary vertices and particle jets.

The analysis extracts the B-decay candidates and produces ROOT ntuples, that can be transferred to the users' private locations and the final tuning is performed using a collection of ROOT scripts [44].

5.2.1 Typical Analysis Procedure

The analyses of the various decays have a common structure, that is here illustrated by means of the reconstruction of the $B_d^0 \to J/\psi(\mu^+\mu^-)K^{*0}(K^+\pi^-)$ channel. The analysis steps are:

1. Get the collections of the analysis objects (from the AOD files) in a given event.

2. Select tracks matching the kinematic cuts for the muon candidates and consult the muon combined objects to retain tracks belonging to the identified muons only. Combine such muon candidates into opposite charged pairs (J/ψ pre-candidates) and possibly cut out the pairs not satisfying some additional conditions like e.g. the muon tracks invariant mass window. By default the track parameters are defined in a point closest to the ATLAS geometrical origin as described in the section 2.2.1. This implies that the further is this point from the real di-muon vertex the more is the invariant mass biased (at this stage of the analysis). This is corrected later by the vertexing procedure.

3. Perform the vertexing of all the preselected muon pairs and apply appropriate quality, position, mass window and other cuts on the J/ψ candidates. The vertexing procedure provides the new muon tracks parameters

in the point of the fitted vertex. The J/ψ candidates are therefore constructed from these *refitted* muon tracks.

4. Select the K^{*0} candidates using similar procedure (combine and use for vertexing the tracks being identified neither as muons nor as electrons).

5. Combine the J/ψ and K^{*0} candidates to create a track quadruplet, fit a common vertex of the whole B_d^0 decay and again reject low-quality, out of the mass window and other unlikely B_d^0 candidates. The vertexing algorithm used in the B-physics analysis is *VKalVrt* [45], based on Kalman filter method. It works with the detailed map of the ATLAS Inner Detector magnetic field and is capable of complex mass, pointing (e.g. to the primary vertex) and conversion vertex type constraints. B-physics analysis packages uses a dedicated interface to the vertexer to allow using physics-objects-like at the input and output and to automatically calculate closely related quantities like the total momentum, invariant mass, proper decay time, etc. The vertexer provides at the output also full covariance matrix of the refitted tracks and vertex parameters (using covariance matrices of the original track parameters and primary/pile-up vertices emerging from the ATLAS track-reconstruction machinery). The matrix is used to calculate per-candidate (B_d^0-hadron) errors on the quantities mentioned above.

6. Finally calculate additional variables (e.g. B_d^0 isolation, flavor tagging etc.) to be either used for further rejection or to be just stored alongside with the B_d^0 candidates in the output ntuple for a consequent ROOT analysis.

5.2.2 Analysis Output

The analysis algorithms use the Athena histogram and ntuple services to produce control histograms and an output ntuple collecting all the selected candidates of the analyzed decay chain in each event. Applying loose cuts during the analysis on the AOD allows a later tuning of the selection cuts on the ntuple level. Thus, to check results with only a slight change of the selection cuts, one does neither need to have the offline software installed nor does one need to rerun the analysis on the Grid. The AOD analysis is intended to extract the required B-hadron candidates per event. However, further statistical analysis on the datasets is performed on the output ntuples, naturally making use of existing statistical and mathematical tools available in ROOT.

6 Observation of $B_d^0 \to J/\psi K^{*0}$ at ATLAS

B_d^0 mesons produced from $b\bar{b}$ pairs in pp collisions in the LHC are reconstructed in ATLAS detector via their exclusive decays $B_d^0 \to J/\psi K^{*0}$, with J/ψ decaying to $\mu^+\mu^-$ and K^{*0} to charged K and π. The chosen J/ψ final state enables these events to be triggered by the ATLAS (di-)muonic triggers and together with the charged K^{*0} daughter tracks allows full B_d^0 meson reconstruction using the ATLAS tracker.

The observation of the exclusive B-decays at ATLAS is the first step in the B-physics analyses and serves for testing of the ATLAS detector performance, especially the tracking and the muon subsystems. The study in this chapter focuses on the $B_d^0 \to J/\psi K^{*0}$ selection cuts and on extraction of the B_d^0 invariant mass, its resolution and the number of signal events. The position of the extracted B_d^0 mass compared to the world average value tests the p_{T} scale of the ATLAS Inner Detector. The analysis was performed using $L_{\mathrm{int}} = 40$ pb^{-1} of ATLAS pp collisions data at centre-of-mass energy of $\sqrt{s} = 7$ TeV. The provided uncertainties of the results are only statistical.

6.1 Data Sample

The used data are required to be collected in luminosity blocks [46, 47] where LHC beams were declared stable. Since the muon and tracking systems are of particular importance for the analysis, only data where these subsystems were operating correctly were accepted, comprising the results of data quality procedures during data taking and later offline reconstruction (technical details in appendix A.1). The analyzed events were accepted by a group of muon-search based triggers (data are stored in so called *muon stream* [26]). The data sample corresponds to $L_{\mathrm{int}} = 40$ pb^{-1} measured with an uncertainty of 3.4 % [22]. Because cross-section measurement is not the subject of this study, no concrete trigger selection was imposed in order to maximize the signal yield. However, efficiency of the B-physics triggers in selecting the events containing $B_d^0 \to J/\psi K^{*0}$ decays is evaluated in section 6.4.

6.2 Analysis Description

The analysis includes both the charge conjugated states B_d^0 and $\bar{B}_d^0$, although in the text only the B_d^0 variant is described. Eventual parts concerning separately B_d^0 and $\bar{B}_d^0$ are mentioned explicitly.

The analysis uses the ATLAS B-physics analysis software tools as described in the section 5.2. Events passing the data quality criteria as noted in the previous section have to contain at least one reconstructed primary vertex and two oppositely charged track pairs. One of the oppositely charged track pairs must be identified as di-muon. However, the information from the Muon Detectors is used only for the muon identification, while the muon-track parameters are taken purely from the Inner Detector measurement alone (the precision of the track parameters is in low-p_{T} region dominated by the ID measurement). Each track is required to have a hit in the Pixel Detector and at least four hits in the Semiconductor Tracker and $p_{\mathrm{T}} > 0.5$ GeV. A kinematic cut $p_{\mathrm{T}} > 0.5$ GeV and $|\eta| < 2.5$

Channel	Generator cuts	Generated Events	Cross-section
$B_d^0 \to J/\psi(\mu^+\mu^-)K^{*0}(K^+\pi^-)$	$p_{\mathrm{T}}(\mu_{1,2}) > 2.5$ GeV	10^6	1.6 nb
$b\bar{b} \to J/\psi(\mu^+\mu^-)X$	$p_{\mathrm{T}}(\mu_{1,2}) > 2.5$ GeV	10^4	425 nb
$pp \to J/\psi(\mu^+\mu^-)X$	$p_{\mathrm{T}}(\mu_{1,2}) > 2.5$ GeV	10^6	56 nb

Table 1: Monte Carlo samples used for the studies of $B_d^0 \to J/\psi K^{*0}$ selection.

copying the Inner Detector acceptance is applied on all the tracks. The muon candidates are not anyhow matched to the muon objects at trigger level.

The B_d^0 candidates are reconstructed using the Inner Detector tracks of the final state particles μ^+, μ^-, K and π, with intermediate steps building the J/ψ and K^{*0} candidates. The composite-particle candidates are created by finding a common vertex of the constituent tracks and selected by applying a vertex quality and an invariant mass window cuts. Optionally additional p_{T} and/or proper decay time cuts are used to further suppress background. The effect of the selection cuts is studied on MC signal and background samples generated by Pythia(B) (with statistics as summarized in table 1):

- Signal $B_d^0 \to J/\psi(\mu^+\mu^-)K^{*0}(K^+\pi^-)$ decay (forcing only the B_d^0 mesons to decay into that mode, assuming similar production and cut efficiencies for $\bar{B}_d^0$). The muons p_{T} are required to be above 2.5 GeV which roughly follows the detector acceptance for muon identification. Similarly, taking into account the ATLAS track reconstruction limits, only the events where K and π p_{T} is above 0.5 GeV are retained.

- Background events coming from B-hadron decays, but allowing only those decay modes containing J/ψ in the decay tree (and forcing the J/ψ to decay to two muons). Each event must contain at least two muons with p_{T} above 2.5 GeV (not necessarily the muons from the J/ψ decay). This sample was also used to pick up several dedicated B-decay channels that had the potential to mimic the $B_d^0 \to J/\psi K^{*0}$ topology and could create structures (reflections) in the reconstructed B_d^0-candidates invariant mass spectrum (see section 6.3.3).

- Background events with J/ψ produced directly in the pp collision, again using the muonic decay mode and 2.5 GeV p_{T} cuts.

The generated events were passed through the standard ATLAS detector simulation and reconstruction chain as described in chapter 4. Grid dataset names corresponding to the samples are collected in appendix A.2.

6.2.1 Muons Reconstruction

In order to successfully build the B_d^0 candidates, the muon candidates have to have associated Inner Detector tracks. There are two types of muon reconstruction algorithms in the ATLAS detector fulfilling this condition:

- **Combined muons reconstruction:** The muon objects are created by combining fitted tracks from Muon Spectrometer with tracks in the Inner

Detector, pairing them by tight matching criteria [17]. However, as noted above, only the ID part is used in the next analyses. Due to low-p_{T} of the muons an improvement by using the combined tracks is expected to be small (but the effect is going to be studied with MC and in analyses with future data).

- **Muons from ID track tagging:** The algorithm treats the cases, where there are not enough hits in the Muon Spectrometer to fit a standalone MS track. Thus is namely covering muon identification of low-p_{T} muons, roughly in $(1-6)$ GeV p_{T} range. Muons of p_{T} below 3 GeV comes from higher pseudorapidity region. A tagged muon is built from an Inner Detector track extrapolated to the MS and matched with the MS hits (that are not associated with any MS track). The tagged muon naturally adopts the parameters only from the ID measurement. Eventual loose and tight muon identification than uses different cuts on the number of MS hits and their distance from the extrapolated ID track [17].

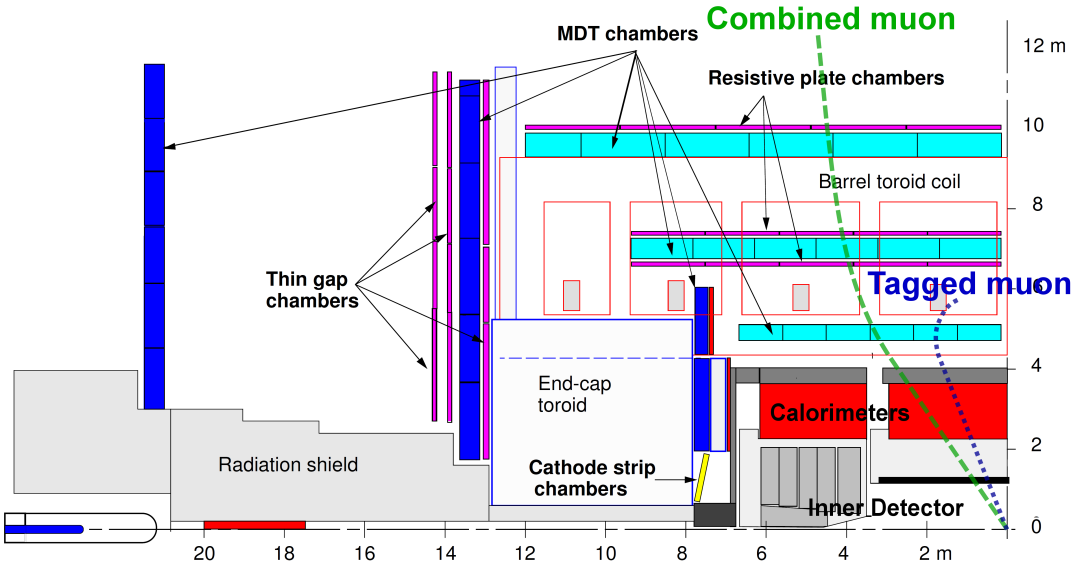

Figure 13: Illustration of the combined muons reconstruction (greed dashed path) and muons from ID track tagging (blue dotted path). Figure taken from [26].

The reconstruction algorithms are illustrated in figure 13. In neither of the cases there are explicit muon p_{T} cuts applied and thus the p_{T} spectrum is given by the implicit acceptance of the algorithms above (practically driven by the Inner and Muon Detectors coverage, magnetic fields and the amount of material between ID and Muon detectors). The p_{T} and η spectrum for the combined and tagged muons in a sample of di-muons with loose selection cuts is shown in figure 14. A fall and distortion of the distributions can be seen at p_{T} below 4 GeV, which is caused by the detector acceptance and the *muon stream* trigger configuration, namely varying prescale factors of trigger chains of different p_{T} thresholds.

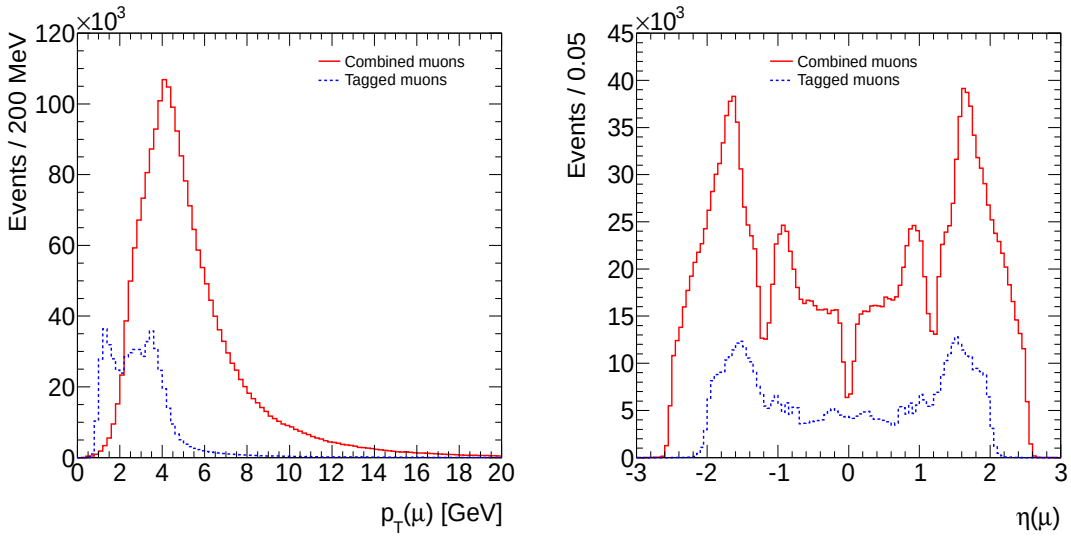

Figure 14: The p_{T} and η spectrum of the muons separately for combined and tagged types in the data. The data muon sample is created from loose di-muon candidates selection requiring successfully fitted common $\mu^+\mu^-$ vertex and di-muon invariant mass 2.7 GeV $< m_{\mu^+\mu^-} <$ 4.0 GeV.

6.2.2 J/ψ Selection

Opposite charge muon tracks are refitted using vertex fitting tool and only those pairs where vertex-fit χ^2/n.d.o.f. < 10 was kept for further analysis, representing J/ψ candidates. The loose vertex quality cut is just to exclude the worst $\mu^+\mu^-$ combinations, rejecting 15 % of background and 0.7 % of signal J/ψ (see figure 15 left). The cut is practically superseded by later quality cut on the overall B_d^0 four-tracks vertex as is demonstrated on figure 15 (right).

The invariant mass of the J/ψ candidates is calculated using the refitted tracks (ID tracks parameters in the fitted J/ψ vertex) of the muon-candidates. In order to account for varying tracks measurement precision and subsequently the mass resolution as a function of the pseudorapidity of the muon tracks, the J/ψ candidates were divided into three samples and different mass window is opened for each of them:

- **Both muons in barrel region (BB)**, where barrel region is defined by requiring the muon track $|\eta| < 1.05$. Only J/ψ with invariant mass inside window of $m_{\mu^+\mu^-} \in (3094 \pm 135)$ MeV are considered in later B_d^0 candidates selection.

- **One muon in the barrel and second in endcap region (EB)** (endcap defined complementary to the barrel). Associated J/ψ invariant mass window is $m_{\mu^+\mu^-} \in (3093 \pm 180)$ MeV.

- **Both muons in endcap region (EE)**, J/ψ invariant mass window opened to $m_{\mu^+\mu^-} \in (3092 \pm 240)$ MeV.

The selection of the mass J/ψ windows is based on results of a fit to the $\mu^+\mu^-$ invariant mass distribution as shown in figures 16, using technique described

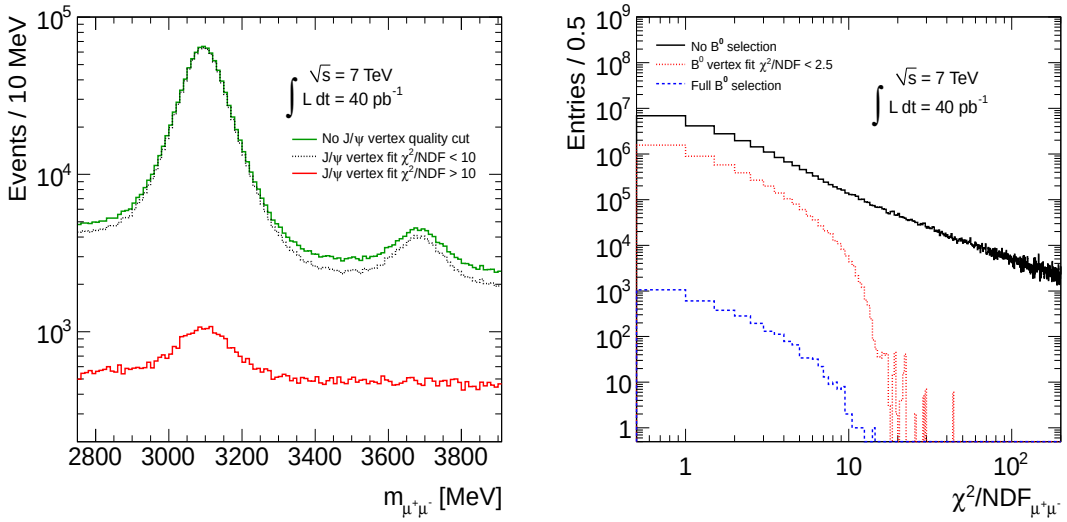

Figure 15: The effect of χ^2/n.d.o.f. < 10 cut on the di-muon mass spectrum (left) extracted from the data. Right: di-muon vertex χ^2/n.d.o.f. distribution for all successfully fitted di-muon vertices in the data sample and the same distributions only for J/ψ candidates used in a B_d^0 candidate passing four-track vertex quality cut χ^2/n.d.o.f. < 2.5 and finally for J/ψ candidates after the full B_d^0 selection cuts. Only negligible fraction of J/ψ candidates does not have χ^2/n.d.o.f. < 10 when required to be successfully used for a B_d^0 construction with associated good-quality four-track vertex.

for the B_d^0 candidates invariant mass fit in section 6.3.1, but with linear background model. The mass windows are symmetric around the fitted mean value and with width retaining 99.8 % of the extracted signal events. The fitted mean values are systematically shifted from the world average J/ψ mass $M_{\rm PDG}(J/\psi) = 3096.916 \pm 0.011$ MeV [48] due to trigger $p_{\rm T}$ cuts and agrees with the results of a detailed J/ψ analysis at ATLAS detector [49].

6.2.3 $B_d^0 \to J/\psi K^{*0}$ Selection

A $B_d^0 \to J/\psi K^{*0}$ decay is reconstructed by fitting the two muon tracks of a J/ψ candidate with other oppositely charged ID tracks into a common vertex. None of these additional two tracks is allowed to be identified as muon. Because the J/ψ natural width is very small, in the fit the muon tracks are constrained to the J/ψ world average [48] mass $M_{\rm PDG}(J/\psi) = 3096.916 \pm 0.011$ MeV [2]. This constraint improves the B_d^0 mass resolution and partly recovers the effect of the systematic J/ψ mass shift (see previous section) in the B_d^0 mass calculation. A B_d^0 and K^{*0} candidates are constructed from the refitted tracks, using appropriate muon, kaon and pion mass hypothesis on the tracks. There is currently no attempt for K/π separation and thus both K/π and π/K combinations are considered and tested through the subsequent cuts flow.

Only those track quadruplets where the vertex-fit χ^2/n.d.o.f. < 2.5 are considered for further analysis. Using MC events, it is demonstrated in the figure 17 (right) that the 4-tracks vertex χ^2/n.d.o.f. distributions is clearly different for sig-

[2] Using just the central value, not accounting for the error.

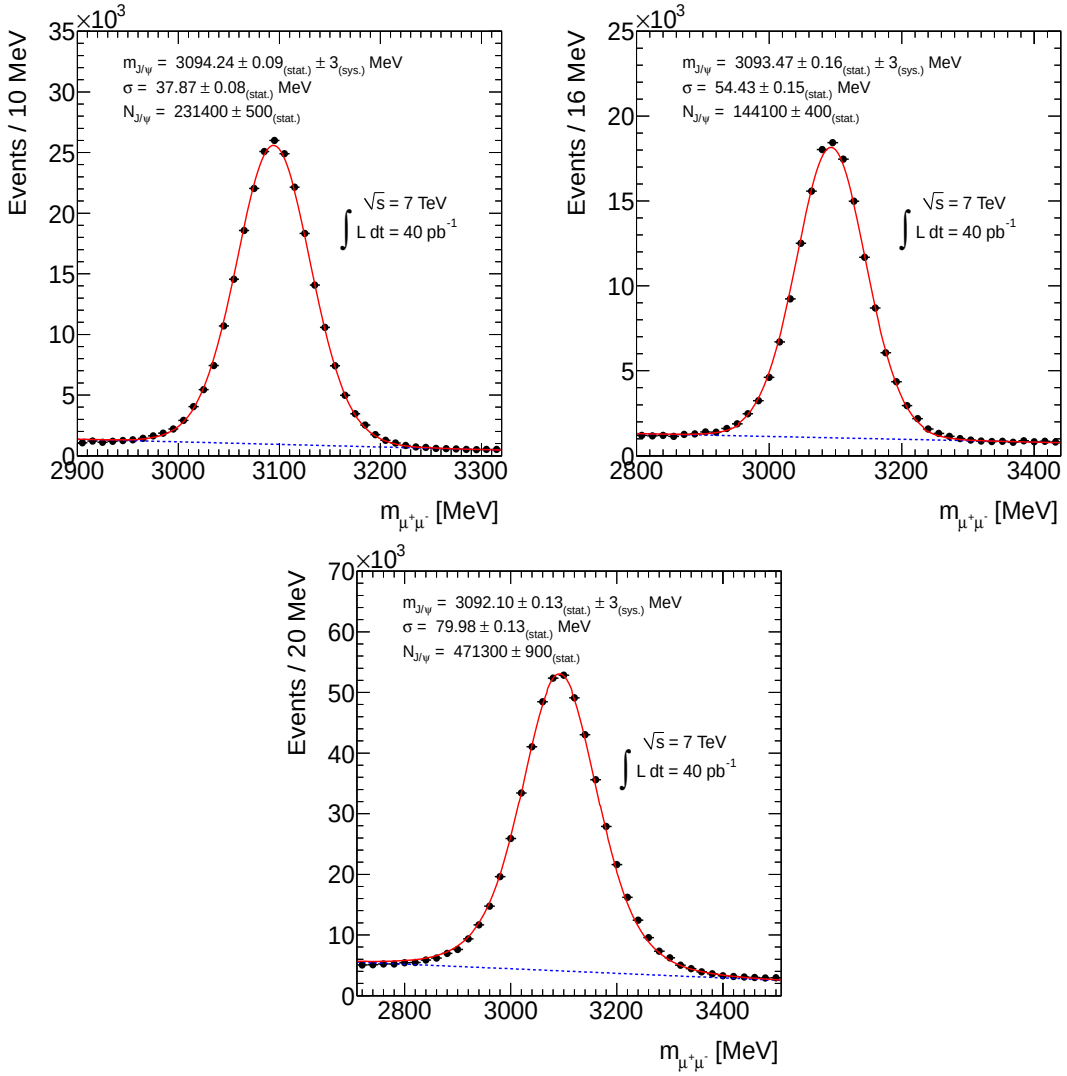

Figure 16: Di-muon invariant mass distributions for BB (top left), EB (top right) and EE (bottom) data samples accounting for different η of the muon tracks. The points are data. The solid red curves represent projections of the results of unbinned maximum likelihood fit to the data, while the blue dashed lines shows the background component of that fit. The signal model of the fit is a poly-Gaussian function (see equation 10). Background is modeled with a linear function.

nal and background events, thus allowing to reduce the background level in the data. The χ^2/n.d.o.f. cut removes 54 % MC background events ($b\bar{b} \to J/\psi X$), while loosing only 5 % of the signal. In addition, poorly measured events which would not significantly contribute to the fit results, but could potentially cause problems, are removed by a cut on the measured B_d^0 proper decay time uncertainty $\delta_{\tau_i} < 0.3$ ps and the B_d^0 invariant mass uncertainty $\delta_{m_i} < 160$ MeV. The uncertainties are calculated for each B_d^0 candidate from the covariance matrix of the 4-tracks vertex fit and the errors of the track parameters. This additional cut removes 7.5 % of the candidates. The distribution of the δ_{τ_i} and δ_{m_i} uncertainties are shown in figures 30.

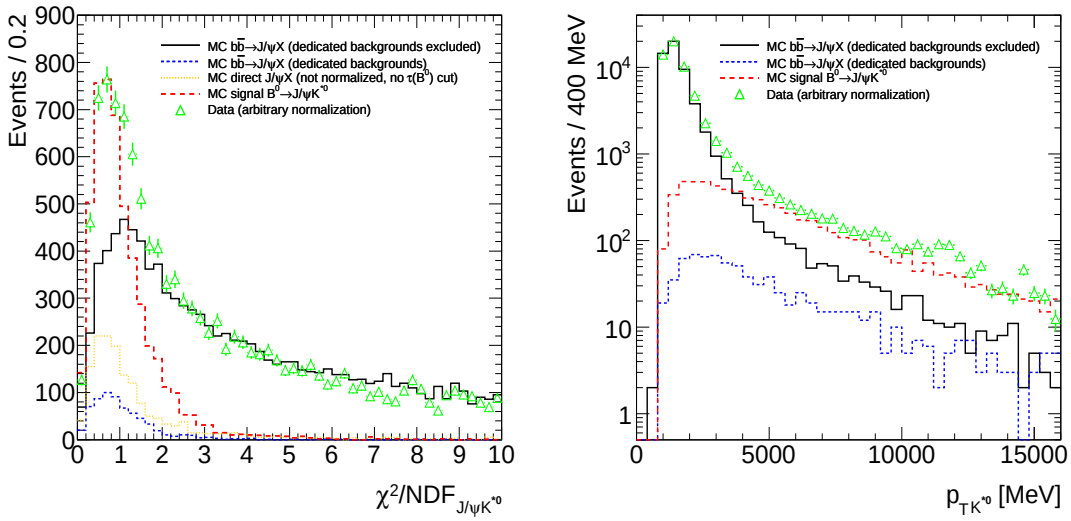

Figure 17: B-vertex χ^2/n.d.o.f. distribution (left) and K^{*0} p_{T} spectrum (right) for the MC signal decay and selected background B_d^0 candidates. Full selection described up to section 6.2.3 is applied, except the cut on the variables that is plotted. The dedicated backgrounds involves $B_d^0 \to J/\psi K\pi$, $B^{\pm} \to J\psi K\pi\pi$, $B_s^0 \to J/\psi\phi$ and $B_s^0 \to J/\psi K^+K^-$ (see also section 6.3.3). The MC $b\bar{b} \to J/\psi X$ and signal curves are normalized according to their Pythia x-sections. The green points are data.

The K^{*0} candidates are requested to have the invariant mass inside a window of $m_{K^{*0}} \in (896 \pm 50)$ MeV. This rejects 25 % of the real K^{*0}, but allows to get rid of the contribution of $\phi \to K^+K^-$ from the $B_s^0 \to J/\psi\phi$ decay, as is shown on figure 25 (right). Because of harder p_{T} spectrum of the K^{*0} from the B-decays a cut $p_{\mathrm{T}}(K^{*0}) > 2.5$ GeV is applied, keeping 77 % of the MC signal events and only 10 % of the $b\bar{b} \to J/\psi X$ background. The p_{T} spectrum for MC signal and background events is shown on the figure 17 (left). However, none of the two cuts above is able to reduce relative contribution from partially reconstructed B-decays, when both the J/ψ and the K^{*0} (real or fake) are coming from the same mother B-hadron. The effect of these background events on the extracted signal B_d^0 candidates is studied in section 6.3.3.

The B_d^0 and $\bar{B}_d^0$ mass spectrum after the all selections above is shown in figure 19 (left).

6.2.4 Selection Based on B-Proper Decay Time

In order to minimize the background contribution from direct J/ψ production, a cut on minimal B_d^0 proper decay time is used. The proper decay time τ is defined as follows:

$$\tau = \frac{L}{\beta\gamma c} \tag{2}$$

where L is distance between primary vertex and the fitted B-vertex, $\beta\gamma$ is the Lorentz factor of the B-hadron and c is the speed of light. Using variables from the B_d^0 reconstruction, the B_d^0 proper lifetime is calculated from the projection to the transverse plane:

$$\tau_{B_d^0} = \frac{L_{\rm xy} M_{\rm PDG}(B_d^0)}{c \cdot p_{\rm T}(B_d^0)} \tag{3}$$

where $p_{\rm T}(B_d^0)$ is the reconstructed transverse momentum of the B_d^0 candidate, $M_{\rm PDG}(B_d^0) = 5279.5 \pm 0.5$ MeV is the world average mass [48] of B_d^0 [3] and $L_{\rm xy}$ is the transverse distance between the primary and B_d^0 vertex (corrected by cosine of the B_d^0 momentum pointing angle to the primary vertex):

$$L_{\rm xy} = |\Delta r_{\rm xy}| \cdot \cos\theta_{\rm xy} \tag{4}$$

as illustrated on the figure 18 (left).

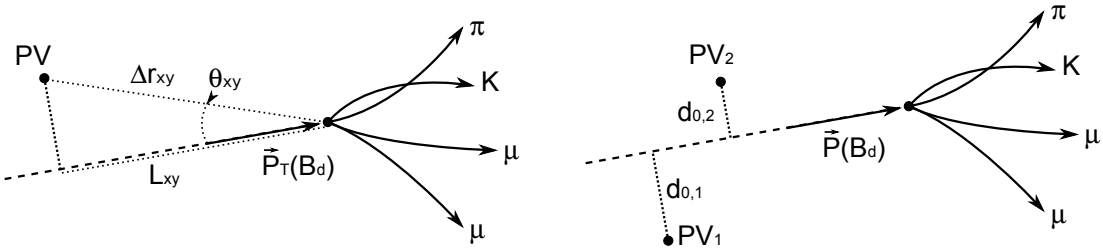

Figure 18: B_d^0 transverse decay length $L_{\rm xy}$ (left) and B_d^0 momentum impact parameter d_0 (right) definitions.

An important step in extracting the $\tau_{B_d^0}$ is the selection of the primary vertex, since more than one primary vertex is present in 75 % of the events with the selected B_d^0 candidates. The distribution of number of primary vertices in the data is shown on figure 20. In the case there are more primary vertices, the one with highest $\sum p_{\rm T}^2$ of the constituent tracks constructing the vertex is chosen. It was checked that this selection also agrees in 99 % with an alternative method when picking up the primary vertex with minimal B_d^0 momentum impact parameter d_0 calculated as the shortest space distance between the direction vector of the reconstructed B_d^0 momentum and the primary vertex, as shown on figure 18 (right). To prevent possible bias in the $L_{\rm xy}$, for each B_d^0 candidate all the primary vertices are refitted after removing the signal tracks from the list of tracks forming the particular primary vertex and the quantities like $L_{\rm xy}$ or d_0 are calculated with respect to the refitted primary vertex position. The selected cut on the B_d^0 proper decay time is: $\tau_{B_d^0} > 0.35$ ps. The background suppression by this additional cut is shown on the B_d^0 and $\bar{B}_d^0$ mass spectrum in figure 19 (right).

[3] Using just the central value, not accounting for the error.

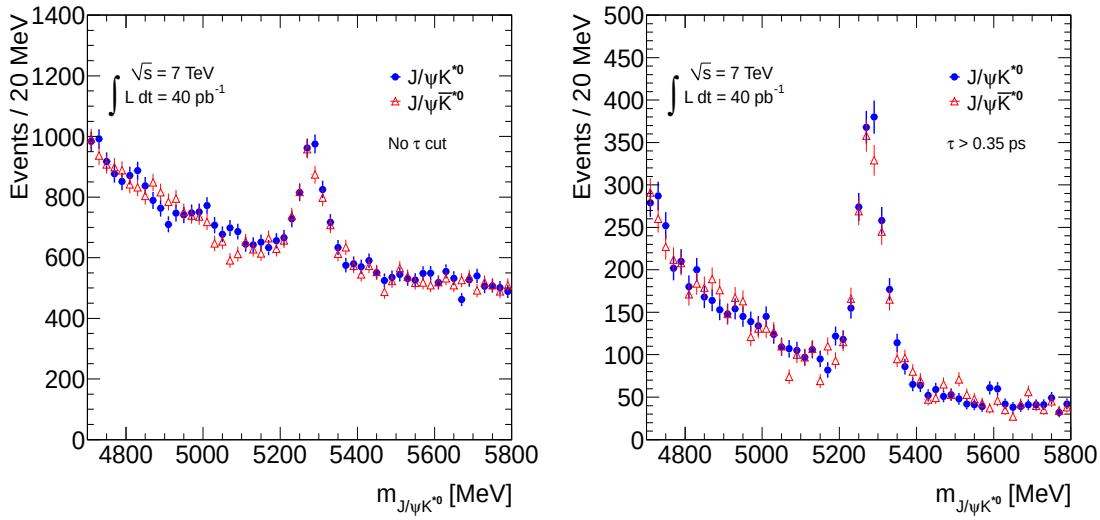

Figure 19: The B_d^0 and $\bar{B}_d^0$ invariant mass spectrum after selection without the proper decay time cut (left) and with the cut (right).

The effect of the cut on different types of the background events can be seen from the proper decay time distribution in the sidebands. In oder to disentangle the various background contributions, an unbinned maximum likelihood fit is performed to the data in B_d^0 invariant mass regions $(5050-5130)$ MeV and $(5430-5550)$ MeV. The $\tau_{B_d^0}$ of the fake B_d^0 candidates constructed from prompt J/ψ and some other two hadronic tracks in the primary vertex is modeled by a Gaussian resolution model. The probability density function (PDF) is defined as:

$$\mathcal{T}_{\text{prompt}}(\tau_i, \delta_{\tau_i}) \equiv R(\tau_i, \delta_{\tau_i}) = \frac{1}{\sqrt{2\pi} S_\tau \delta_{\tau_i}} \exp\left(\frac{-\tau_i^2}{2(S_\tau \cdot \delta_{\tau_i})^2}\right) \tag{5}$$

where τ_i and δ_{τ_i} are per-candidate proper decay times and its uncertainty (input data). The S_τ is a scale factor accounting for possible difference between the measured δ_{τ_i} distribution and the overall τ_i resolution. For the B_d^0 candidates formed from indirect J/ψ the PDF is constructed from two exponentials convoluted with the resolution function:

$$\mathcal{T}_{\text{indirect}}(\tau_i, \delta_{\tau_i}) = \left[\frac{b}{\tau_{\text{eff1}}} \exp\left(\frac{-\tau'}{\tau_{\text{eff1}}}\right) + \frac{1-b}{\tau_{\text{eff2}}} \exp\left(\frac{-\tau'}{\tau_{\text{eff2}}}\right)\right] \otimes R(\tau' - \tau_i, \delta_{\tau_i}) \tag{6}$$

This accounts for two types of the fake B_d^0 candidates: a fast decaying component where J/ψ from a B-hadron decay is combined with two tracks from the primary vertex, and slow decaying component corresponding to partially reconstructed B-decays in the left mass sideband. The proper decay time distributions in the left and right sidebands separately are plotted in figure 21 (right), showing, as expected, relatively larger slow-decaying component in the left sideband. The τ_{eff1} and τ_{eff2} are fitted parameters as well as the relative fraction b of those two exponential PDFs. An additional double-exponential term symmetric around zero is introduced to describe small negative tails in the data, respectively small fraction of bad measurements:

$$\mathcal{T}_{\text{tails}} = \left[\frac{1}{2 \cdot \tau_{\text{eff3}}} \exp\left(\frac{-|\tau'|}{\tau_{\text{eff3}}}\right)\right] \otimes R(\tau' - \tau_i, \delta_{\tau_i}) \tag{7}$$

The fitted likelihood function is created from the PDFs above, introducing relative fractions b_1 and b_2 (fitted parameters):

$$\mathcal{L} = \prod_{i=1}^{N_{\text{side}}} \left[b_2 \cdot [b_1 \cdot \mathcal{T}_{\text{prompt}}(\tau_i, \delta_{\tau_i}) + (1-b_1) \cdot \mathcal{T}_{\text{tails}}(\tau_i, \delta_{\tau_i})] + (1-b_2) \cdot \mathcal{T}_{\text{indirect}}(\tau_i, \delta_{\tau_i}) \right] \quad (8)$$

where N_{side} is the total number of the B_d^0 candidates in the selected sideband regions.

The fit result is plotted in the figure 21 (left). Suppression of the two main background components by several proper decay time cuts is presented in table 2, together with the most important fitted parameters. Because the prompt peak resolution is $\sigma_\tau = 0.139 \pm 0.002$ ps, the cut $\tau_{B_d^0} > 0.35$ ps removes practically all this type of background. Due to poly-Gaussian shape of the resolution function, the σ_τ is defined as the half-width of $R(\tau' - \tau_i, \delta_{\tau_i})$ for which an integral symmetrical around zero retains 68.3 % of the number of fitted B_d^0 candidates constructed from prompt J/ψ. The selected proper decay time cut also removes significant part (47 %) of the non-prompt background by reducing the fast decaying component. The signal reduction in the table 2 is a simple calculation using exponential function with the world average measured B_d^0 lifetime $\tau_{\text{PDG}}(B_d^0) = 1.525 \pm 0.009$ ps.

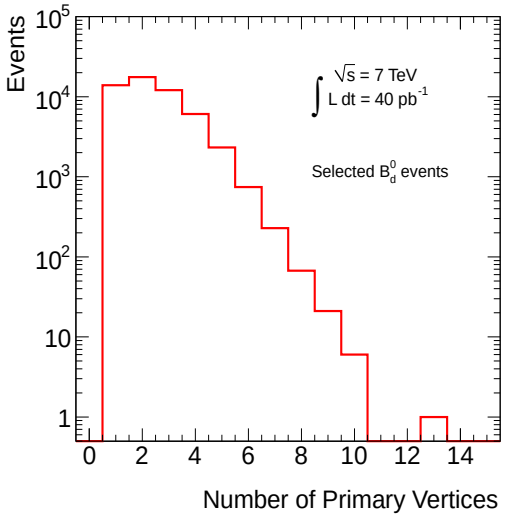

Figure 20: Distribution of the number of primary vertices in the events containing the B_d^0 candidates selected in section 6.2.3.

6.2.5 Ambiguous Candidates Selection

With the selections above, there is a possibility of multiple B_d^0 candidates being found in one event. In particular, the candidates can share some of the tracks and thus should not be both included in the analysis. Due to very low BR of the total $B_d^0 \to J/\psi(\mu^+\mu^-)K^{*0}(K^+\pi^-)$ decay $(5 \cdot 10^{-5})$, a probability of having two signal decays in one event is negligible. Therefore only one B_d^0 candidate is kept within an event. Its selection depends on what/if daughter tracks are shared among the B_d^0 candidates:

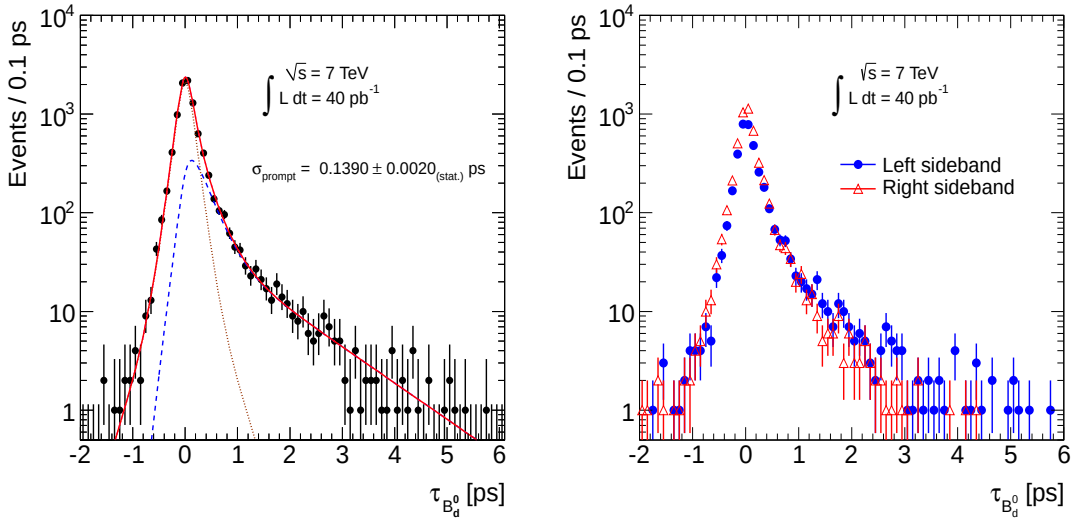

Figure 21: Left: B_d^0 proper decay time distribution in the sidebands. The black points are data and the red solid curve is the projection of the unbinned maximum likelihood fit. The dashed blue curve corresponds to the projection of the indirect-J/ψ induced component of the fit and the dotted brown curve to the prompt-J/ψ induced model together with the symmetric exponential describing small tails in the data (bad measurements). Right: B_d^0 proper decay time distribution from data separately for each left and right sideband.

Minimal $\tau_{B_d^0}$	**Prompt** J/ψ $\mathcal{T}_{\text{prompt}}$ $S_\tau = 1.03 \pm 0.02$ $\sigma_\tau = 0.139 \pm 0.002$ ps	**Indirect** J/ψ $\mathcal{T}_{\text{indirect}}$ $\tau_{\text{eff1}} = 0.26 \pm 0.03$ ps $\tau_{\text{eff2}} = 1.18 \pm 0.10$ ps	**Signal** (no smearing) $\tau_{\text{PDG}}(B_d^0)$ 1.525 ± 0.009 ps
0.25 ps	5.4 %	54 %	85 %
0.30 ps	3.3 %	48 %	82 %
0.35 ps	2.0 %	43 %	79 %
0.40 ps	1.2 %	38 %	77 %
0.45 ps	0.7 %	34 %	74 %
0.50 ps	0.4 %	31 %	72 %

Table 2: Acceptance of background B_d^0 candidates by a proper decay time cut.

Ambiguity type (tracks sharing)	**Fraction of B_d^0 candidates, no $\tau_{B_d^0}$ cut**	**Fraction of B_d^0 candidates, with $\tau_{B_d^0}$ cut**
All 4 tracks shared (swapped K/π)	18 %	22 %
Both K and π tracks are shared, not J/ψ	1.2 %	0 %
J/ψ and one of K or π tracks are shared	15 %	7 %
Only J/ψ is shared	7 %	2.2 %
One μ track or one of K or π are shared	0.06 %	0.03 %
Two B_d^0 candidates not sharing any tracks	0 %	0 %

Table 3: Data after full selection (with and without $\tau_{B_d^0}$ cut). Fractions of B_d^0 candidates in events with more B_d^0, divided into groups according to what parts of the track quadruplets is shared among the candidates.

- B_d^0 and $\bar{B}_d^0$ candidates are created from the same 4 tracks, sharing the J/ψ and having just swapped the K/π mass hypothesis on the two ID tracks: the cases when this type of ambiguity occurs are characterized by a symmetrical K^{*0} decay topology having similar K and π track momentum and therefore it is not possible to distinguish the correct combination on event-by-event basis. A B_d^0 candidate reconstructed from the signal decay tracks, but with wrong K/π mass assignment, forms a peak 3.5× wider and shifted by +10 MeV from the true MC signal (see figure 22 right). The K^{*0} mass spectrum for the wrong combination is rather flat (figure 22 left). The latter fact allows for purely statistical based selection of correct K/π track mass assignment by taking the candidate where K^{*0} ($\bar{K}^{*0}$) mass is closer to the world average mean value. Since the K^{*0} mass peak width is dominated by the natural Breit-Wigner shape, there is no correlation between the B_d^0 and K^{*0} masses of the true signal decays and thus the selection itself does not bias the B_d^0 mass in any other way than by the fraction of wrongly assigned K/π masses. Testing the method on MC signal events, it picks up the correct combination in 63 % cases and introduces 5 % increase in the observed B_d^0 mass resolution.

- Any other multiple B_d^0 candidates are treated by selecting the best fitted quadruplet vertex, keeping the one with the lowest vertex-fit χ^2/n.d.o.f.. A small signal contribution is seen in the plotted B_d^0 mass spectrum of the candidates (figure 23), where J/ψ and eventually one of the K or π tracks is shared. That would suggest that these cases correspond to $B \to J/\psi X$ decays with multiple hadronic tracks.

The fraction of events with ambiguous B_d^0 candidates is summarized in table 3 and the corresponding mass distributions shown on figure 23. It is obvious that the fraction of multiple B_d^0 candidates grows with the number of shared tracks. As expected, there are no cases of having completely different B_d^0 candidates in one event.

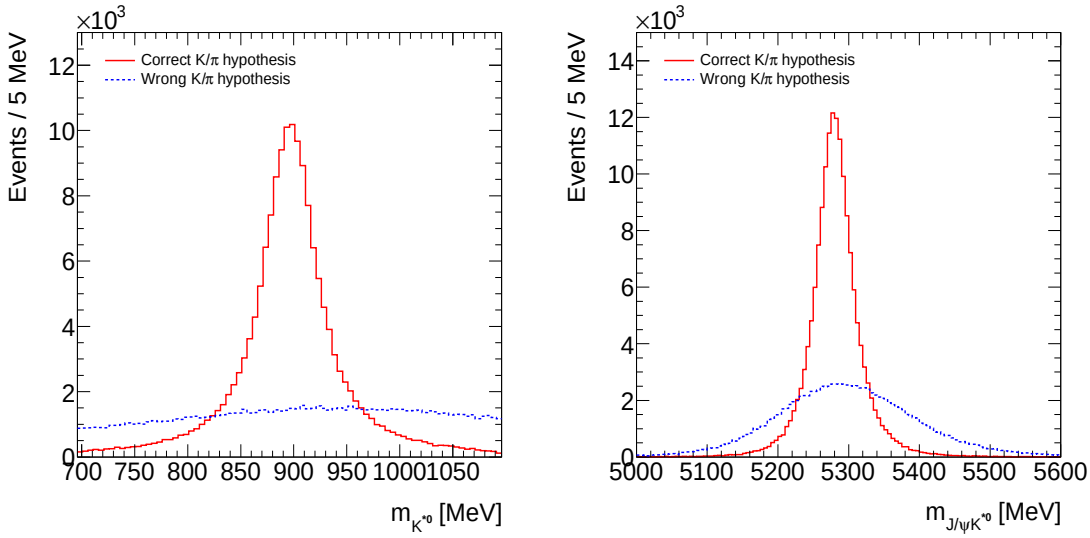

Figure 22: MC signal events. Reconstructed K^{*0} (left) and B_d^0 (right) mass spectrum for correctly assigned K/π masses to the tracks and for the swapped combination.

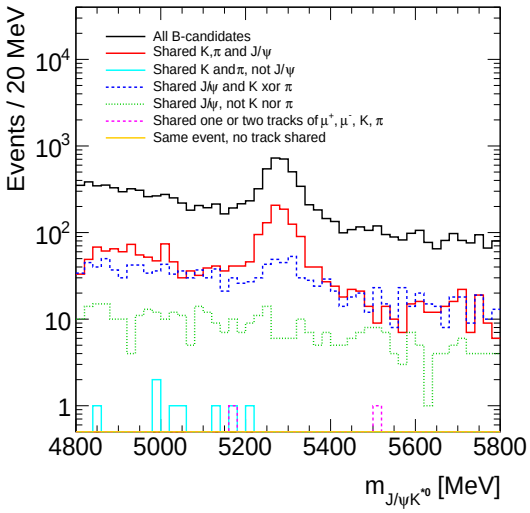

Figure 23: The mass spectrum of all B_d^0 candidates after full selection including proper decay time cut (black solid line) and of only those sitting in the same event with another candidate, eventually sharing same parts of the tracks quadruplet as explained in the legend.

6.3 B_d^0 Invariant Mass Distribution Fit

6.3.1 Method of the Fit

To extract the B_d^0 mass and the number of signal events, an unbinned maximum likelihood fit to the invariant mass data is used. The likelihood function is defined by:

$$\mathcal{L} = \prod_{i=1}^{N} \left[f_{\text{sig}} \cdot \mathcal{M}_{\text{sig}}(m_i, \delta_{m_i}) + (1 - f_{\text{sig}}) \cdot \mathcal{M}_{\text{bkg}}(m_i) \right] \tag{9}$$

where m_i and δ_{m_i} are B_d^0 candidate invariant mass and its uncertainty calculated using the covariance matrix of the tracks quadruplet vertex fit. N is the number of input B_d^0 candidates. The fitted parameter f_{sig} represents fraction of signal events. The probability density functions $\mathcal{M}_{\text{sig}}$ and $\mathcal{M}_{\text{bkg}}$ are used to model the signal and background shape of the B_d^0 mass distributions. For the signal a poly-Gaussian function is used (similar as when modeling the proper time distribution of B_d^0 candidates constructed from prompt J/ψ):

$$\mathcal{M}_{\text{sig}}(m_i, \delta_{m_i}) = \frac{1}{\sqrt{2\pi} S_m \delta_{m_i}} \exp\left(\frac{-(m_i - m_B)^2}{2(S_m \cdot \delta_{m_i})^2} \right) \tag{10}$$

This allows to account for varying mass resolution in different parts of the detector using the track parameters' errors provided by ATLAS reconstruction algorithms. Possible inaccuracy in the calculation of these errors is analogously to equation 5 corrected by a fitted scale factor S_m. The extracted B_d^0 mass is represented by the fitted parameter m_B. In the likelihood constructed above, it is assumed that the δ_{m_i} distribution is the same for signal and background events. The validity of this simplification is presented in figure 30 (right), showing that the mean and RMS of the distributions for background events in the sidebands and for extracted signal are similar.

The background is modelled by a combination of constant and exponential function approximating flat mass spectrum in the right sideband and growing background with lower mass values:

$$\mathcal{M}_{\text{bkg}}(m_i) = \frac{1 + d_{\text{exp}} \cdot e^{\frac{-(m_i - m_C)}{m_{\text{sl}}}}}{\int_{m_{\text{min}}}^{m_{\text{max}}} \left(1 + d_{\text{exp}} \cdot e^{\frac{-(m_i - m_C)}{m_{\text{sl}}}} \right)} \tag{11}$$

where $m_C = (m_{\text{max}} + m_{\text{min}})/2$ and the fitted parameters m_{sl} and d_{exp} correspond to exponential slope and the relative fraction of the linear and exponential terms. On account of partially reconstructed B-mesons and kinematic reflections, no attempt is made to model the background far from the signal peak. The following mass window was selected for the fit: $m_{J/\psi K^{*0}} \in (5050 - 5550)$ MeV (defining m_{min} and m_{max} values), where the selected background model is an adequate description within the available statistics of input data.

The fit has five free parameters f_{sig}, m_B, S_m, d_{exp} and m_{sl}. These values are used to extract the expected number of B_d^0 signal decays N_{sig}, the mass resolution σ_m and the expected number of background events N_{bkg} in mass interval of $m_B \pm 3 \cdot \sigma_m$. Due to nontrivial signal peak shape, the mass resolution is (similarly to section 6.2.4) defined as half-width of the signal peak concentrating 68.3 %

of $N_{\rm sig}$ symmetrically around m_B. The uncertainty of σ_m and $N_{\rm bkg}$ is calculated using a covariance matrix returned by the fit and the returned errors of the fitted parameters.

6.3.2 Fit results

The results of the fit for data without and with proper decay time cut are shown on figure 24. The extracted B_d^0 mass from the fit is 5278.6 ± 1.3 MeV for the selection without the $\tau_{B_d^0}$ cut and 5279.6 ± 0.9 MeV when keeping only candidates with $\tau_{B_d^0} > 0.35$ ps. All given errors are statistical only. These results are consistent with the world average measured value of $M_{\rm PDG}(B_d^0) = 5279.5 \pm 0.5$ MeV. The number of background candidates 10280 ± 110 in the mass range of $m_B \pm 3 \cdot \sigma_m$ is reduced to 1330 ± 60 after the proper decay time cut, while the number of fitted signal events changes from 2680 ± 150 to 2340 ± 80. At the same time, it is clear that the proper decay time cut allows to improve the statistical error on the extracted B_d^0 mass although the number of signal events is smaller. The results including the extracted mass resolution are summarized in table 4.

The main analysis and results were published as a part of ATLAS conference note [50] and accompanied by supporting material for the ATLAS community in internal ATLAS note [51].

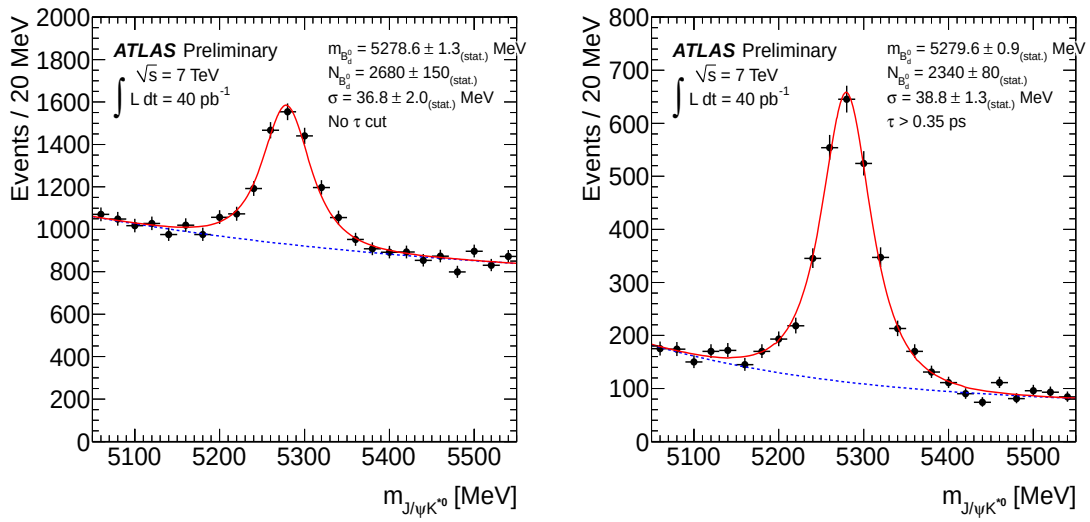

Figure 24: The invariant mass spectrum of the B_d^0 and $\bar{B}_d^0$ candidates after selection without $\tau_{B_d^0}$ cut (left) and with $\tau_{B_d^0}$ cut (right) and in range defined for the used unbinned maximum likelihood fit. The black points are data. The solid red curve is the projection of the fit to the data, while the dashed blue curve represents just the background component of the fitted function.

6.3.3 Specific Backgrounds

As was mentioned in section 6.2.3, there are some types of background candidates whose rejection by K^{*0} $p_{\rm T}$ and $J/\psi K^{*0}$ vertex χ^2/n.d.o.f. is similar to the signal events. These fake B_d^0 candidates can have potentially non-flat invariant mass structure. In order to study the impact on the extracted B_d^0 mass and number

Selection	m_B [MeV]	σ_m [MeV]	N_{sig}	N_{bkg}
no $\tau_{B_d^0}$ cut	5278.6 ± 1.3 MeV	36.8 ± 2.0 MeV	2680 ± 150	10280 ± 110
with $\tau_{B_d^0}$ cut	5279.6 ± 0.9 MeV	38.8 ± 1.3 MeV	2340 ± 80	1330 ± 60

Table 4: Summary of the fit results to mass distribution of B_d^0 candidates. The number of background events is given in the $3 \cdot \sigma_m$ range around the fitted B_d^0 mass m_B.

of signal events, MC study is performed focusing on dedicated list of B-meson decays that can potentially affect the invariant mass spectrum shape:

- $B_s^0 \to J/\psi\phi$
- $B_d^0 \to J/\psi K\pi$
- $B^{\pm} \to J\psi K\pi\pi$
- $B_s^0 \to J/\psi K^+K^-$

The B_d^0 and K^{*0} candidates arising from these (partially) reconstructed B-decays are required to pass all the selection cuts introduced in the previous sections. The invariant mass spectrum of those fake B_d^0 and K^{*0} candidates is plotted in figures 25. When plotting the K^{*0} mass, the cut on the K^{*0} mass window is omitted. As can be seen in the left figure 25, only the $B_s^0 \to J/\psi\phi$ forms a structure in the reconstructed K^{*0} mass spectrum, accumulating events in the left sideband and ending at kinematic threshold around 845 MeV. This was the motivation for the selected K^{*0} mass window in section 6.2.3. All the other dedicated backgrounds are flat across the whole K^{*0} mass interval, disallowing any possibility to reduce these backgrounds at K^{*0} selection level. However the structure of the B_d^0 mass distribution of the dedicated background is more complicated. The $B^{\pm} \to J\psi K\pi\pi$ and $B_s^0 \to J/\psi K^+K^-$ decays create a structure in the left side from the B_d^0 nominal mass due to missing π/K track and wrong π mass hypothesis respectively. The most dangerous background naturally comes from the $B_d^0 \to J/\psi K\pi$ decay. Counting the backgrounds and true signal events in $3 \cdot \sigma_m$ region, the dedicated backgrounds contribute by 18 % to the total number of events. Including the backgrounds does not have a significant impact on the extracted B_d^0 mass from the unbinned maximum likelihood fit (only the mass resolution very slightly rises when comparing to a fit to pure MC signal events).

The K^{*0} mass spectrum from the data is plotted and fitted in figure 26. Only those candidates from the $B_d^0 \to J/\psi K^{*0}$ decays after full selection except the K^{*0} mass window cut are examined. In order to clean up the sample, the B_d^0 in which the K^{*0} is contained must have the invariant mass in the signal peak by requiring $m_{J/\psi K^{*0}} \in (5279.5 \pm 120)$ MeV. In addition, to avoid complicated modeling of the background shape, the contribution from $B_s^0 \to J/\psi\phi$ is rejected by requiring $m_\phi \notin (1019.5 \pm 13)$ MeV and $m_{B_s^0} \notin (5366.3 \pm 100)$ MeV, where the ϕ and B_s^0 are constructed from the same tracks as the K^{*0} and B_d^0 respectively, just modifying the π track mass hypothesis. (The ϕ and B_s^0 mass windows are based on B_s^0 analysis in [50]). The used unbinned maximum likelihood fit is constructed in similar way as in equation 9, but with different signal and background PDFs. The signal one is constructed as a convolution of Breit-Wigner

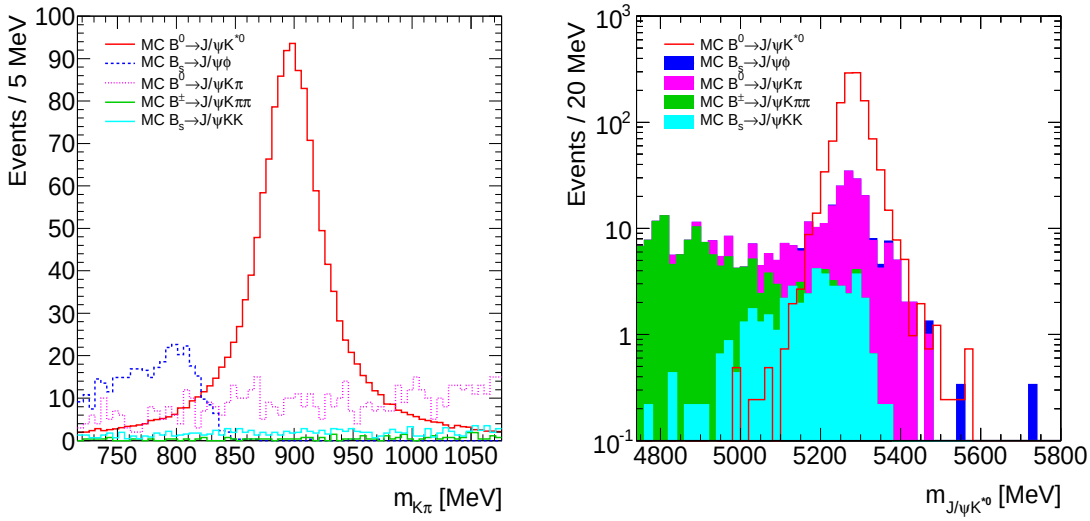

Figure 25: K^{*0} (left) and B_d^0 (right) mass distributions for the MC signal decay and dedicated backgrounds from the $b\bar{b} \to J/\psi X$ MC sample. On the right figure the contributions from the various background decay types are accumulated on top of each other. The relative branching ratios are corrected to the recent world average measurements [48] (because of obsolete data in the Pythia generator).

distribution and Gaussian function:

$$\mathcal{M}^K_{\rm sig}(m_{Ki}) = \frac{N^{\rm sig}_{\rm norm}}{(m' - m_{K^{*0}})^2 + \left(\frac{\Gamma_{K^{*0}}}{2}\right)^2} \otimes \frac{1}{\sqrt{2\pi}\sigma_K} \exp\left(\frac{-(m' - m_{Ki} - m_{K^{*0}})^2}{2\sigma_K^2}\right) \tag{12}$$

where m_{Ki} are the input masses of the K^{*0} candidates, $m_{K^{*0}}$ is the extracted K^{*0} mass, σ_K is a fitted parameter representing detector resolution and $\Gamma_{K^{*0}}$ is a constant value corresponding to K^{*0} world average Breit-Wigner width $\Gamma_{\rm PDG}(K^{*0}) = 50.3 \pm 0.6$ MeV [52]. The constant $N^{\rm sig}_{\rm norm}$ is just the proper normalization of the PDF to unity in the fitted K^{*0} mass interval $m_{K^{*0}} \in (660 - 1140)$ MeV. The background shape $\mathcal{M}^K_{\rm bkg}(m_{Ki})$ is modeled by second order polynomial:

$$\mathcal{M}^K_{\rm bkg}(m_{Ki}) = N^{\rm bkg}_{\rm norm} \cdot (1 + a_1 \cdot m_{Ki} + a_2 \cdot m^2_{Ki}) \tag{13}$$

where a_1 and a_2 are fitted parameters and $N^{\rm bkg}_{\rm norm}$ again a constant normalization factor. The fitted K^{*0} mass 896.2 ± 0.8 MeV is within the statistical uncertainty consistent with the world average value $M_{\rm PDG}(K^{*0}) = 895.94 \pm 0.22$ MeV [48]. The number of extracted signal K^{*0} candidates in the region $m_{K^{*0}} \in (896 \pm 50)$ MeV (the mass window used for the full B_d^0 selection) is 3710 ± 90. Comparing to the 2340 ± 80 extracted B_d^0 candidates (table 4), it is clear that beside the K^{*0} from the $B_d^0 \to J/\psi K^{*0}$ decay, there are also real K^{*0} candidates forming part of the background below the signal B_d^0 peak.

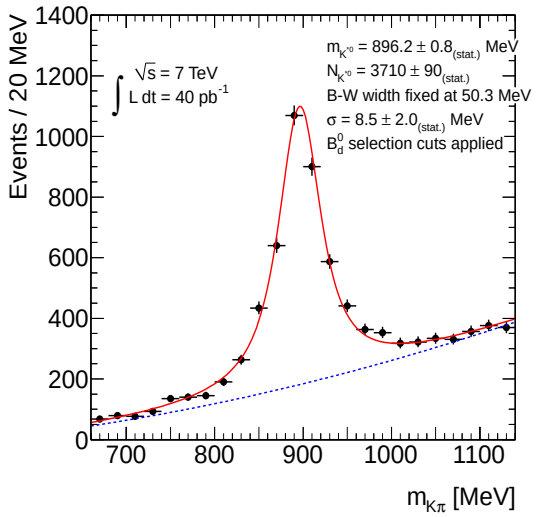

Figure 26: K^{*0} mass spectrum from the $B_d^0 \to J/\psi K^{*0}$ decays with reconstructed B_d^0 invariant mass inside $m_{J/\psi K^{*0}} \in (5279.5 \pm 120)$ MeV interval and rejected candidates forming good $B_s^0 \to J/\psi\phi$ decay. The black points are data. The solid red curve is the projection of the unbinned maximum likelihood fit to the data, while the dashed blue curve represents just the background component of the fitted function.

6.4 B-Triggers Performance

Although the analysis above was maximizing the signal yield by not applying any explicit trigger selection, studying the performance of dedicated B-physics trigger of selecting the signal events is important in predicting the signal yields for the incoming data. In addition, the later precision measurements like B_s^0/B_d^0 decay angular analysis will require well defined efficiency and acceptances and thus a well defined trigger configuration will have to be chosen.

The composition of the triggers activated during 2010 data taking was rapidly changing as the instantaneous luminosity was rising (see figure 3), including early periods where no HLT trigger was applied up to the last runs where some of the basic B-physics triggers were already prescaled. Therefore the fractions of events in this section do not represent an efficiency measurement, but only an overview of what triggers picked up the B_d^0 candidates after the full selection (except the B_d^0 proper decay time cut). In order to test the B-physics triggers and due to relatively low instantaneous luminosity in the 2010 LHC run, all the B-triggers described in section 3.1 were active, including number of supporting and calibration configurations for each of the trigger types. The fractions of offline-selected B_d^0 candidates picked up by selected B-physics triggers are summarized in table 5. However, since all these triggers are targeting on J/ψ signature, there is very high overlap between them. The triggers in their primary configuration devoted to $(B \to)J/\psi$ analyses, which includes just the *TrigDiMuon* and the topological trigger, picked up 64 % of the events with the B_d^0 candidates. Including in addition also the muon+track trigger and a *TrigDiMuon* trigger configured to do track search in the full Inner Detector volume (Full-scan trigger - see section 3.1), the fraction of triggered events grows to 76 %. The remaining 24 % of B_d^0 events were collected by either single-muon triggers not specifically

Trigger type		Accepted B_d^0 events	Average prescale
Basic J/ψ triggers:			
`EF_mu4_Jpsimumu`	(*TrigDiMuon*)	61 %	1.12
`EF_2mu4_Jpsimumu`	(topological)	22 %	1.00
`EF_mu4_Trk_Jpsi`	(muon+track)	25 %	1.11
Higher muon p_{T} threshold:			
`EF_mu6_Jpsimumu`	(*TrigDiMuon*)	33 %	1.12
`EF_mu4mu6_Jpsimumu`	(topological)	16 %	1.00
`EF_mu6_Trk_Jpsi`	(muon+track)	20 %	1.11

Table 5: Fractions of offline-selected B_d^0 candidates triggered by the main B-physics triggers in several configurations (for more details see section 3.1). The *TrigDiMuon* and the muon+track triggers were prescaled in the very end of the 2010 data taking due to too high rate of the single muon signatures at trigger level 1.

searching for a J/ψ signature, or by a set of supporting and calibration B-physics triggers with loose cuts (not requiring $\mu^+\mu^-$ vertex, soft muon-identification conditions, lower muon p_{T} cuts, alternative tracking or muon reconstruction algorithms, etc.). In offline analysis, these events are mostly characterized by a very low p_{T} ($\lesssim$ 3 GeV) of one of the muons. Full list of concrete trigger signatures for all the B_d^0 events is dumped in appendix A.3. The evolution of the signal B_d^0 events acceptance with LHC data periods in 2010 is shown in figure 27.

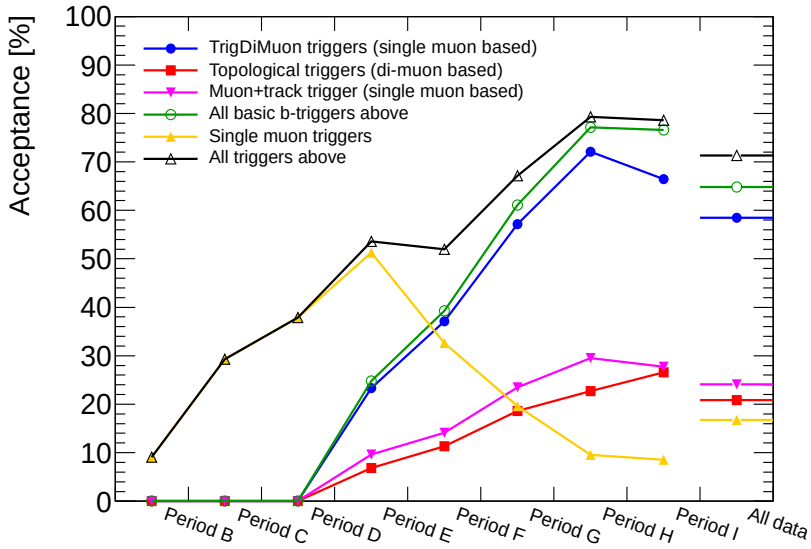

Figure 27: Acceptance of the B_d^0 events by the basic set of (di)muon triggers over the 2010 data periods (and in the last bin for the full data). Up to *period E*, the instantaneous luminosity was low enough to keep unprescaled the lowest-p_{T} single muon triggers. The B-physics J/ψ triggers (*TrigDiMuon*, topological and muon+track) become important since the *period F* and in the last periods the L1 single-muon based B-physics triggers had to be already prescaled (although still collecting majority of the B_d^0 events). The remaining fraction of B_d^0 events (not triggered by any of the triggers above) were collected by various supporting and calibration triggers.

7 B_d^0 Lifetime Measurement

Measurement of the B_d^0 lifetime in the reference decay channel $B_d^0 \to J/\psi K^{*0}$ servers for validation of the fitting procedure for $B_s^0 \to J/\psi\phi$ CPV studies coming with the larger collected data. The measurement also probes the ATLAS performance in secondary vertexes reconstruction.

The used data are identical to the one in the previously discussed $B_d^0 \to J/\psi(\mu^+\mu^-)K^{*0}(K^+\pi^-)$ observation study. Also the selection of the B_d^0 candidates follows the cuts presented in the previous chapter, except that no proper decay time cut is applied. Leaving in the B_d^0 candidates that are constructed from J/ψ and K^{*0} produced in the primary interaction, it allows to precisely describe the detector time resolution, since it is the only factor defining proper decay time distribution of this type of background.

7.1 Method of the Fit

The lifetime is measured using simultaneous unbinned maximum likelihood fit to the B_d^0 candidates proper decay time and invariant mass data. The sources contributing to the background were already described in section 6.2.4 and thus the background proper decay time part of the likelihood function is reusing the probability density functions and their relative fractions from equation 8:

$$\begin{aligned} \mathcal{T}_{\text{bkg}}(\tau_i, \delta_{\tau_i}) &= b_2 \cdot [b_1 \cdot \mathcal{T}_{\text{prompt}}(\tau_i, \delta_{\tau_i}) + (1 - b_1) \cdot \mathcal{T}_{\text{tails}}(\tau_i, \delta_{\tau_i})] \\ &+ (1 - b_2) \cdot \mathcal{T}_{\text{indirect}}(\tau_i, \delta_{\tau_i}) \end{aligned} \tag{14}$$

The PDF of the signal decay time is defined as a an exponential decay smeared by the resolution function 5:

$$\mathcal{T}_{\text{sig}}(\tau_i, \delta_{\tau_i}) = \left[\frac{1}{\tau_B} \exp\left(\frac{-\tau'}{\tau_B}\right)\right] \otimes R(\tau' - \tau_i, \delta_{\tau_i}) \tag{15}$$

with τ_B being the fitted B_d^0 lifetime. The B_d^0 mass data are for the signal events described by the probability density function 10. In order not to over-parametrize the fit (accounting for the limited amount of data), the background mass description was simplified to a linear function, while limiting the B_d^0 mass range to $m_{J/\psi K^{*0}} \in (5159 - 5399)$ MeV:

$$\mathcal{M}_{\text{bkg}_\text{l}}(m_i) = \frac{1}{m_{\max} - m_{\min}}[1 + d \cdot (m_i - m_C)] \tag{16}$$

where d is a fitted parameter, while the boundary $m_{\max}$, $m_{\min}$ and center m_C masses are constants corresponding to the range defined above.

The likelihood of the simultaneous mass-lifetime fit is constructed as:

$$\mathcal{L} = \prod_{i=1}^{N} \left[f_{\text{sig}} \cdot \mathcal{M}_{\text{sig}}(m_i, \delta_{m_i}) \cdot \mathcal{T}_{\text{sig}}(\tau_i, \delta_{\tau_i}) + (1 - f_{\text{sig}}) \cdot \mathcal{M}_{\text{bkg}_\text{l}}(m_i) \cdot \mathcal{T}_{\text{bkg}}(\tau_i, \delta_{\tau_i}) \right] \tag{17}$$

As well as in the previous likelihood fits, it is assumed that the distribution of per-candidate δ_{τ_i} and δ_{m_i} uncertainties is similar for all signal and all the background types. The distributions are plotted on figures 30. Within the current statistics,

they are compatible. The largest possible bias can come from the 23 % difference between means of the signal and background δ_{τ_i} histograms. A systematic error is assigned to this simplification as described in section 7.3.3.

To summarize, input of the likelihood fit constructed above are the B_d^0 candidates mass and proper decay times and their uncertainties, and the following parameters are fitted:

- the fraction of signal events f_{sig} in the mass region of the fit,
- the fitted B_d^0 mass m_B and lifetime τ_B,
- the scale factors S_m and S_τ reflecting the difference between measured and fitted mass and proper decay time resolutions,
- the slope d of the mass distribution of the background B_d^0 candidates,
- the effective lifetimes τ_{eff1}, τ_{eff2} and τ_{eff3} describing the exponential background proper decay time distributions and their relative fractions b, b_1 and b_2.

The values and the covariance matrix of the fit-parameters are then used to calculated the number of signal and background events within the mass interval $m_B \pm 3 \cdot \sigma_m$ with mass-resolution σ_m defined as in section 6.3.1 as the signal-peak half-width collecting 68.3 % of the signal events.

7.2 Fit Results

The results of the simultaneous mass and lifetime fit performed on the selected B_d^0 candidates (see section 6.2, not applying proper decay time cut) are presented in figures 28. The B_d^0 mass returned by the fit is $m_B = 5279.0 \pm 0.8$ MeV with extracted resolution of $\sigma_m = 34.3 \pm 0.9$ MeV. The number of signal and background candidates in the $3 \cdot \sigma_m$ mass region is $N_{\text{sig}} = 2750 \pm 90$ and $N_{\text{bck}} = 9680 \pm 310$. The measured B_d^0 lifetime is $\tau_B = 1.51 \pm 0.04$ ps. All the errors are statistical only. The systematic uncertainties are evaluated in the next sections. Values of all the fitter parameters are summarized in table 6.

Main parameters		**Background parameters**		**Background fractions**	
m_B	5279.0 ± 0.8 MeV	τ_{eff1}	0.22 ± 0.03 ps	b	0.64 ± 0.06
S_m	1.28 ± 0.08	τ_{eff2}	1.12 ± 0.14 ps	b_1	0.83 ± 0.07
τ_B	1.51 ± 0.04 ps	τ_{eff3}	0.12 ± 0.02 ps	b_2	0.65 ± 0.02
S_τ	0.96 ± 0.02	d	-0.7 ± 0.2		
f_{sig}	0.20 ± 0.01				

Table 6: Table of the resulting values of the parameters of the simultaneous B_d^0 mass and lifetime fit.

Figure 29 shows the correlations of the parameters. For the measured B_d^0 mass and lifetime, there are no significant correlations with the other parameter. The largest one is between τ_B and the long-lived background component

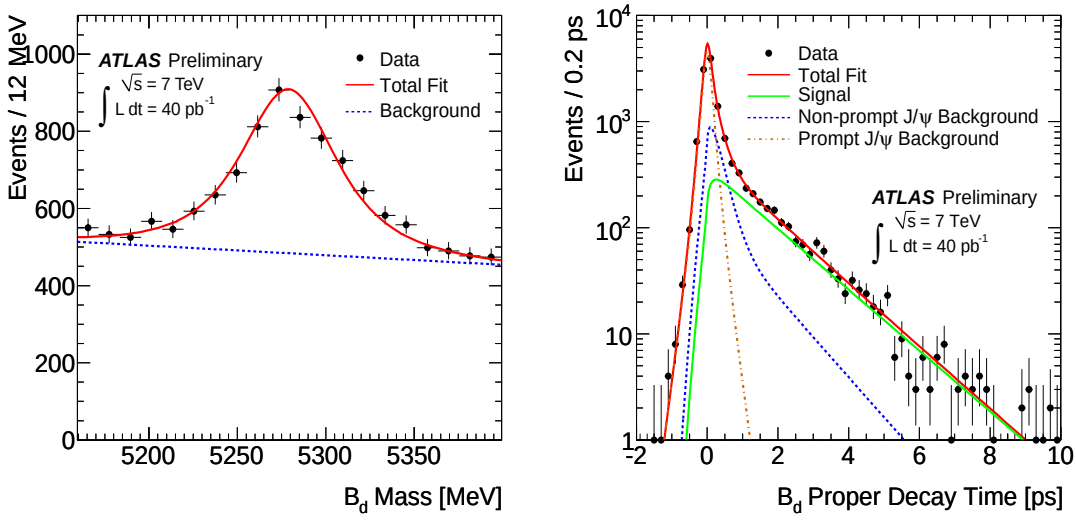

Figure 28: The invariant mass spectrum (left) and the proper decay time distribution (right) of the B^0_d and $\bar{B}^0_d$ candidates after selection without $\tau_{B^0_d}$ cut. The black points are data and the red solid curve is the projection of the unbinned maximum likelihood fit. On the mass plot, the dashed blue curve represents just the background component of the fitted function. On the proper decay time plot, the dashed blue curve corresponds to the projection of the indirect-J/ψ induced component of the fit and the dotted brown curve to the prompt-J/ψ induced model together with the symmetric exponential describing small tails in the data. Signal component of the proper decay time is drawn by the solid green curve.

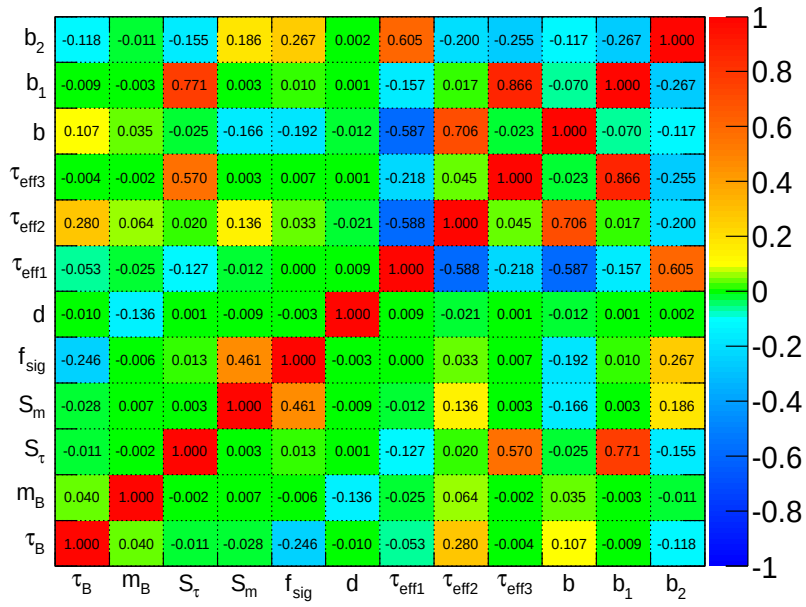

Figure 29: Correlations between the parameters of the simultaneous B^0_d mass and lifetime fit.

τ_{eff2}. However, this is where the mass part of the fit helps by driving the signal fraction. Large correlation can be seen between the proper decay time scale factor S_τ and the parameters of the $\mathcal{T}_{\text{tails}}$ symmetric exponential approximating badly measured data. The correlations are there because these tails could be considered as part of the detector resolution and in that case should be used for smearing of the signal exponential function. That was not done in the final version of the fit, but a systematic uncertainty arising from this was evaluated as one of the alternative models in section 7.3.1 - omitting $\mathcal{T}_{\text{tails}}$ to allow the tails to be reflected in large fitted scale factor. The background lifetime parameters are strongly correlated because they do not correspond to concrete physics parameters, but only serve for effective description of the fake B_d^0 candidates proper decay time distribution.

7.3 Systematic Uncertainties

Because the purpose of this measurement is mainly to validate the procedure for later CPV measurements, and accounting for the large statistical errors of the fit, only the most important systematics are studies instead of providing an exhaustive list of all the possible effects. The systematics uncertainties are described and evaluated in the following sections.

7.3.1 Signal and Background Model in the Likelihood Fit

Systematics arising from imperfect modeling of the signal and background PDFs in the likelihood fit are determined by rerunning the fit using different, but still reasonable, parametrization. The model variations tested were:

- Choose double-Gaussian for the signal mass fit as an alternative to the per-event mass errors poly-Gaussian function to account for the varying resolution in different parts of the detector.
- Similarly choose double-Gaussian for the proper decay time resolution PDF.
- Use more complicated description of the background B_d^0 mass distribution: 2^{nd} order polynomial or an exponential PDF as in the equation 11.
- Consider possible different scaling factors for the signal and background candidates.
- Exclude the $\mathcal{T}_{\text{tails}}$ component (see equation 7) from the fit. This PDF was describing negative tails in the data. However, there is a possibility that the negative tails are effectively part of the real resolution. In that case they should have be used for the smearing of the signal and background exponential PDFs. Excluding the $\mathcal{T}_{\text{tails}}$ forces the S_τ scale-factor to try to fit the tails and thus include them in the resolution function. The scale factor extracted from this fit exercise indeed grown from (0.96 ± 0.02) to (1.11 ± 0.01).
- Allow to vary the center of the poly-Gaussian PDF describing the prompt-J/ψ induced background (PDF 5) in order to account for eventual systematic shift in the proper decay times (however, the fitted value of the center was found to consistent with zero within the statistical precision).

Due to the constraints from the available statistics, each of the model variations were tested separately as they introduce more free parameters to the fit. Fitted lifetime τ_B is extracted from each the fit and compared to the value obtained in the default fit model. The maximum deviation - 0.01 ps - is then taken as the systematic uncertainty due to this source.

7.3.2 Fitting Procedure

To assure the fitting procedure does not introduce a bias in the fit results, several thousand pseudo-experiments was performed. Repeatedly generating the mass and lifetime distribution according to the data and performing the fit, the fit results were found to be compatible within the statistical uncertainties. Since no discrepancy was observed, this systematic error is considered to be negligibly small.

7.3.3 Time Uncertainty Model

The fit assumes the same distributions of the signal and background per-candidate mass and proper decay time errors. These distributions are plotted on figures 30, separating the signal from the background by a simple sidebands-subtraction method. With higher statistics, it would be possible to model the per-candidates errors as well, but this would require to introduce a number of additional free parameters which is not feasible with the current number of events. To estimate the eventual systematics, different proper decay time uncertainty models are assumed for the signal and background candidates, following the method published in [53]. The average change in the fitted parameters is then stated as the systematics due to this simplification of the fit. For the τ_B the systematics yields 0.03 ps.

7.3.4 Choice of Mass Window

A possible systematics can come from the choice of the B_d^0 mass window. To exclude possible effect of the B_d^0 candidates at the edge of the used mass interval, fits were performed with several different B_d^0 mass windows and the largest observed change in the fitted parameters is assigned as the systematic uncertainty of the default choice. There were performed 14 fits varying the mass window from $(5169 - 5389)$ MeV up to $(5079 - 5479)$ MeV. Variations of the main fitted parameters are presented in figures 31. The largest change in the B_d^0 lifetime with respect to the default fit is 0.01 ps. The small systematics also proves the robustness of the used fit-model since the mass window strongly influences the relative number of signal and background events. (Similarly stability of the fit results with B_d^0 proper decay time window is shown in the appendix B.1).

7.3.5 Choice of Primary Vertex

Due to the pile-up conditions in 2010 data taking, the events contain more then one primary vertex (1.9 PV per event in average). The distribution is plotted in figure 20. To determine the B_d^0 candidate lifetime, it is important to select the correct one. Failure to do so can introduce a bias in the measured lifetime.

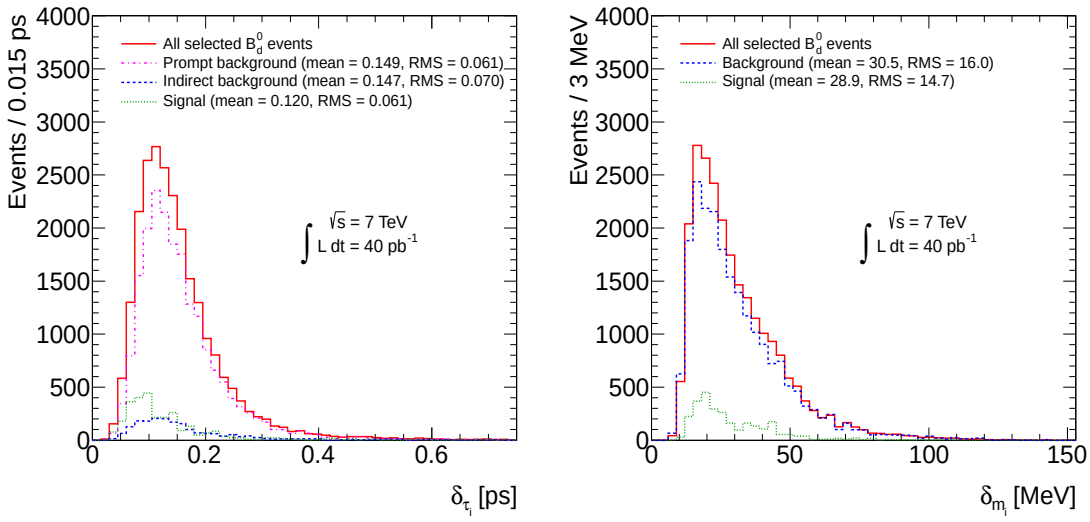

Figure 30: Distribution of the per-candidate proper decay time uncertainties δ_{τ_i} (left) and B_d^0-mass uncertainties δ_{m_i} (right) of the selected B_d^0 candidates from data (not applying the cuts on these observables). The distributions are decomposed to signal and background contributions using simple sidebands subtraction method: It is assumed that the δ_{τ_i} and δ_{m_i} of the background candidates under the B_d^0-mass signal peak are the same as in the left and right sidebands (as defined in the section 6.2.4). Background distribution of the uncertainties is thus obtained from the sidebands, but scaled to the total number of background events as obtained from the B_d^0 mass fit. Signal distribution is then constructed by subtracting the background histogram from the distributions for all events. The prompt-J/ψ and indirect-J/ψ induced backgrounds in the proper decay time uncertainty plot are classified using $\tau_{B_d^0} > 0.5$ ps cut.

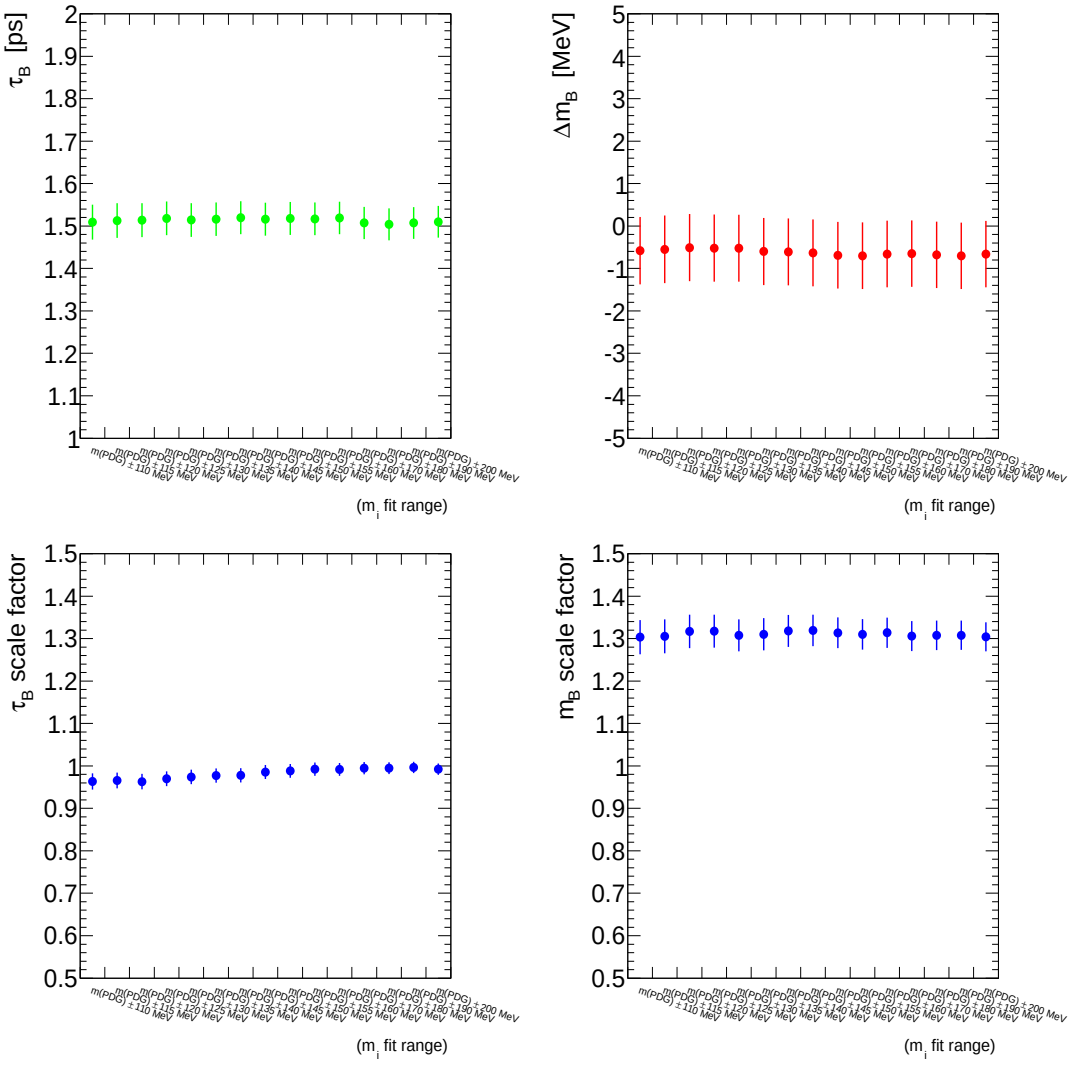

Figure 31: Variations of the fit results with the choice of the B_d^0 mass window. The fitted B_d^0 lifetime is shown on the top left figure, the invariant mass (relative to the world average value $M_{\rm PDG}(B_d^0) = 5279.5 \pm 0.5$ MeV) on the top right. The bottom figures shows the stability of the mass (right) and proper decay time (left) error scale factors.

As was already described in section 6.2.4, two methods of selecting the correct PV were compared:

- The default selection using PV with the highest $\sum p_{\mathrm{T}}^2$ of the constituent tracks.
- Alternative selection picking up PV with the smallest B_d^0 momentum impact parameter d_0 (see figure 18 right). Since the relative distance of the primary vertices in the transverse plane is comparable to the resolution, the selection is mostly driven by the separation alongside the beam-axis.

Since it was found out that the two selections overlap in 99 % of the events, the systematics coming from the PV selection is negligible.

7.3.6 Alignment of the Inner Detector

Imperfect knowledge of the Inner Detector alignment can arise in a systematic uncertainty on the lifetime measurement. The default used dataset was reconstructed using alignment set of constants determined from the data taken at 7 TeV centre-of-mass energy. In order to estimate the systematic variation, the analysis is repeated using the same data but reconstructed with earlier set of alignment constants based on data taken at 900 GeV. This latter alignment is based on lower statistics and smaller average track momentum, leading to a higher uncertainty due to multiple scattering. The B_d^0 lifetime extracted from that earlier-aligned dataset is (1.54 ± 0.04) ps, which is by 0.03 ps greater than the default result. This difference is thus taken as the systematic uncertainty due to the alignment procedure.

The above method of determination of the systematics is rather conservative and based on following observations: The alignment procedure is more focused on momentum scale than on the vertex-related quantities. A residual misalignment in vertexing is typically showing up in a distribution of the tracks transverse impact parameter $d_{0\mathrm{xy}}$. It was found out that the deviations of these distributions in the 7 TeV-data based alignment are approximately of the same size as is the difference in these deviations between the two alignment sets. E.g. a polar angle dependence of the mean tracks $d_{0\mathrm{xy}}$ is shown in figures 32 and 33, taken from [54] and [55]. The deviations are of the order of ~ 10 μm. Similar size variations were also observed during data taking as a consequence of changed detector conditions. In another similar lifetime measurement at ATLAS [8] there were performed more detailed studies using MC simulations with various types of distorted geometries. There the resulting systematics on decay time measurement is of the same amount.

7.3.7 Proper Decay Time Acceptance

Simulated events were used to check whether the selection cuts are potentially introducing a non-trivial shaping of the decay time distribution. However, as is proven on figure 34, the efficiency of reconstructing and selecting the MC signal decay $B_d^0 \to J/\psi(\mu^+\mu^-)K^{*0}(K^+\pi^-)$ with the default set of cuts, is not exhibiting any dependence or excessive behaviour (accounting for the statistical fluctuations). This is also partly confirmed on data by the stability of the fit results in various proper decay time ranges as is described in the appendix B.1.

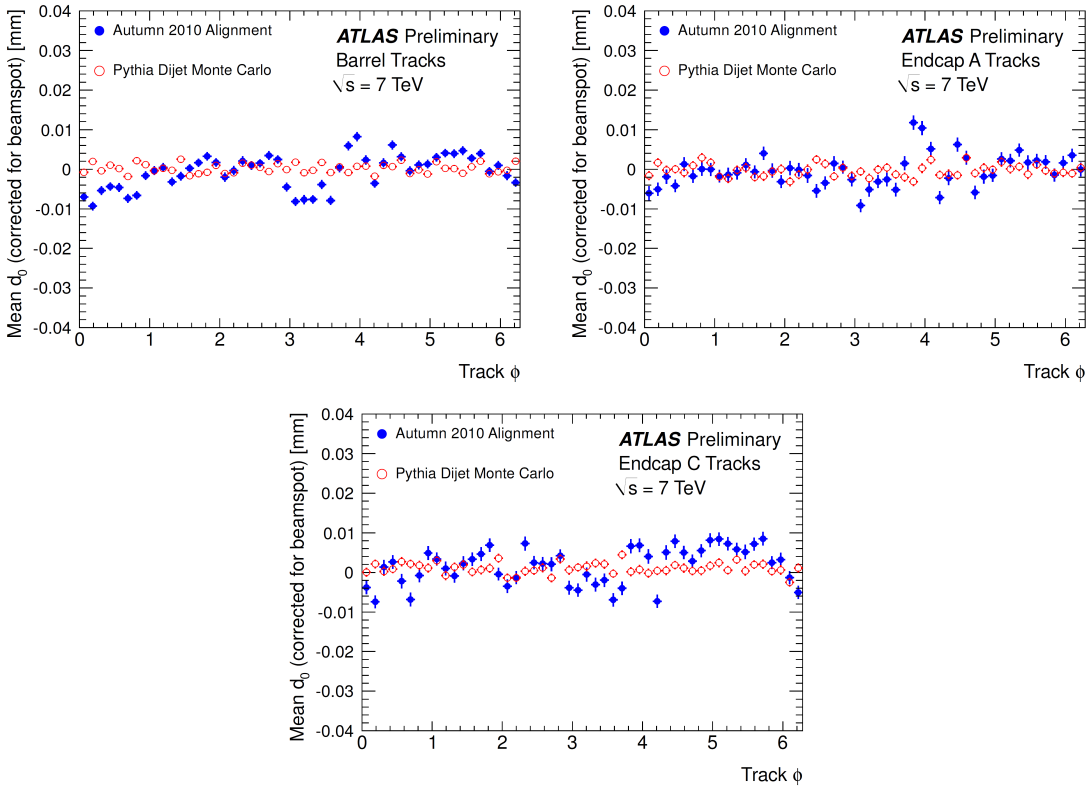

Figure 32: Mean of the transverse impact parameter distribution as a function of the tracks direction in the polar angle ϕ. Blue points are illustrating the scale of the residual misalignment in the default 7 TeV-data based alignment. Figures taken from [54].

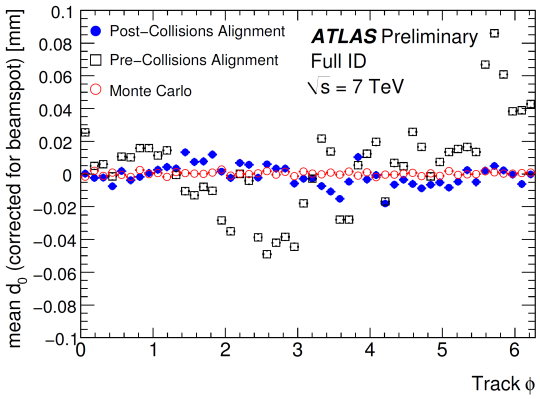

Figure 33: Mean of the transverse impact parameter distribution as a function of the tracks direction in the polar angle ϕ. Blue points are illustrating the scale of the residual misalignment in the old 900 GeV-data based alignment. Figure taken from [55].

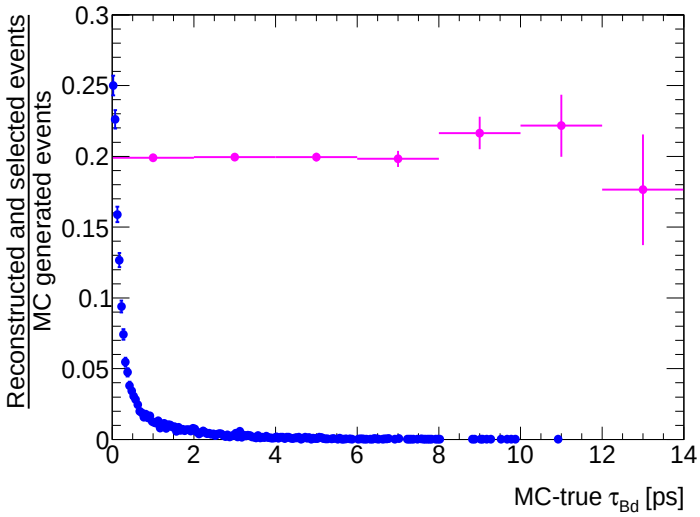

Figure 34: MC simulation of the $B_d^0 \to J/\psi(\mu^+\mu^-)K^{*0}(K^+\pi^-)$ decay. The magenta points show the efficiency of the reconstruction cuts as a function of the true B_d^0-candidate proper decay time. The blue points representing the true B_d^0-candidates proper decay time distribution (arbitrary normalized) are just for illustration of how many events falls to each bin of the efficiency graph.

7.3.8 Summary of the Systematic Uncertainties

The systematic uncertainties in the B_d^0 lifetime measurement are summarized in table 7 (only the non-zero ones are included). Since there is not correlation between the discussed types of systematics, they are quadratically added up and this total systematics uncertainty is presented in the table too. The final

Source of systematics	**Systematic uncertainty**
Modeling signal and background	0.01 ps
Time uncertainty model	0.03 ps
Mass window	0.01 ps
Alignment	0.03 ps
Total systematics	**0.04 ps**

Table 7: Table of the systematics uncertainties of the B_d^0 lifetime measurement.

value of the B_d^0 lifetime measured in the ATLAS detector in the decay channel $B_d^0 \to J/\psi(\mu^+\mu^-)K^{*0}(K^+\pi^-)$ is thus (compared to present world average value [48]):

$$\textbf{ATLAS measurement:} \quad \tau_{Bd} = 1.51 \pm 0.04\ \text{(stat.)} \pm 0.04\ \text{(syst.)}\ \text{ps}$$
$$\textbf{World average (PDG):} \quad \tau_{Bd} = 1.525 \pm 0.009\ \text{ps}$$

This analysis and results were published in ATLAS conference note [7] accompanied by supporting material for the ATLAS community in an internal ATLAS note [56].

8 Summary of the Results

The B_d^0 mesons are observed by ATLAS experiment in the decay mode $B_d^0 \to J/\psi(\mu^+\mu^-)K^{*0}(K^+\pi^-)$. Analyzing 40 pb^{-1} of pp collision data at 7 TeV the number of observed signal events is 2340±80 after full selection cuts, when using an unbinned maximum likelihood fit to the B_d^0 candidate masses to separate the signal from the background. To measure the B_d^0 meson mass and lifetime, the same dataset and selection is used except a cut on the proper decay time of the B_d^0 candidates, and a simultaneous unbinned maximum likelihood fit to the B_d^0 candidate masses and proper decay times is performed. The number of extracted signal events under this selection and fit is 2750 ± 90. Systematic uncertainties arising from fit-modeling, fitter-procedure, per-candidate uncertainty model, choice of B_d^0 mass window, choice of primary vertex, alignment procedure and proper decay time acceptance were evaluated. The largest two contributions come from the Inner Detector alignment, for which a rather conservative estimate was used, and from the proper decay time uncertainty model, which is being improved with more statistics. The total size of the systematic error is comparable to the statistical errors fit. The main results of the analysis are summarized in table 8 and plotted in figures 35 (top).

The same technique is used to measure mass and lifetime of the B_s^0 meson in decay channel $B_s^0 \to J/\psi(\mu^+\mu^-)\phi(K^+K^-)$ [7, 50]. The selection of the B_s^0 candidates follows the cuts used for the B_d^0; the ϕ meson is constructed from two opposite charge tracks with p_{T} above 1 GeV and requiring their invariant mass to be within a range of 1009 MeV $< m_{KK} <$ 1031 MeV. Using the 40 pb^{-1} of pp collision data at 7 TeV the number of observed signal events is 358 ± 22 and 463 ± 26 for the full set of cuts and for the selection without proper decay time cut respectively.

In the case of the B_s^0 meson, there are two eigenstates with distinct decay widths Γ_L (short lived) and Γ_H (long lived). Both the components have been determined at the Tevatron from the $B_s^0 \to J/\psi\phi$ decay using time-dependent angular analysis, that allows the simultaneous extraction of the CP-even and CP-odd amplitudes characterised by the two decay widths [57, 58]. The two decay widths are usually parametrized in terms of their difference $\Delta\Gamma_s = \Gamma_L - \Gamma_H$ and the average $\Gamma_s = (\Gamma_L + \Gamma_H)/2$. The current world average values [59] of these decay widths are: $1/\Gamma_s = 1.472^{+0.024}_{-0.026}$ ps and $\Delta\Gamma_s/\Gamma_s = +0.092^{+0.051}_{-0.054}$, or equivalently $1/\Gamma_L = 1.408^{+0.033}_{-0.030}$ ps and $1/\Gamma_H = 1.543^{+0.058}_{-0.060}$ ps. Because of the limited statistics in the collected 2010 ATLAS data, only single-exponential is used to model the signal B_s^0 proper decay time distribution. Ignoring the difference $\Delta\Gamma_s$ is known to provide inherently biased lifetime (by the order of $\Delta\Gamma_s$), due to the unequal contribution of the short and long lived eigenstates in the final state of $B_s^0 \to J/\psi\phi$. However, the bias is smaller than the measurement error with the 2010 ATLAS data.

The results of the B_s^0 mass and single-lifetime measurement are again summarized in table 8 and plotted in figures 35 (bottom). The measured lifetime value agrees within the precision with the world average Γ_s. From the Tevatron measurements, the dominating component in the $B_s^0 \to J/\psi\phi$ final state is the short lived B_L. And indeed the single-exponential lifetime value returned by the ATLAS fit is closer to the shorter lifetime $1/\Gamma_L = 1.408^{+0.033}_{-0.030}$ ps.

	ATLAS measurement	World average value
B_d^0 lifetime	1.51 ± 0.04 (stat.) ± 0.04 (syst.) ps	1.525 ± 0.009 ps
B_s^0 lifetime	1.41 ± 0.08 (stat.) ± 0.05 (syst.) ps	1.472 ± 0.026 ps
B_d^0 mass	5279.0 ± 0.8 (stat.) MeV	5279.5 ± 0.5 MeV
B_s^0 mass	5363.7 ± 1.2 (stat.) MeV	5366.3 ± 0.6 MeV

Table 8: Results of the ATLAS B_d^0 and B_s^0 mass and lifetime measurement.

To summarize: the extracted B_d^0 and B_s^0 lifetime and mass are compatible with the world average values within the precision of the current measurement. The results demonstrate that a simultaneous mass and proper decay time unbinned maximum likelihood fit using per-candidate errors is able to separate the B_d^0 and B_s^0 signal events from background and to fit a single exponential to those signal events. Agreement with the world average also confirms the primary and secondary vertex reconstruction, which provides the measurement of the transverse decay length, is working well within the ATLAS detector.

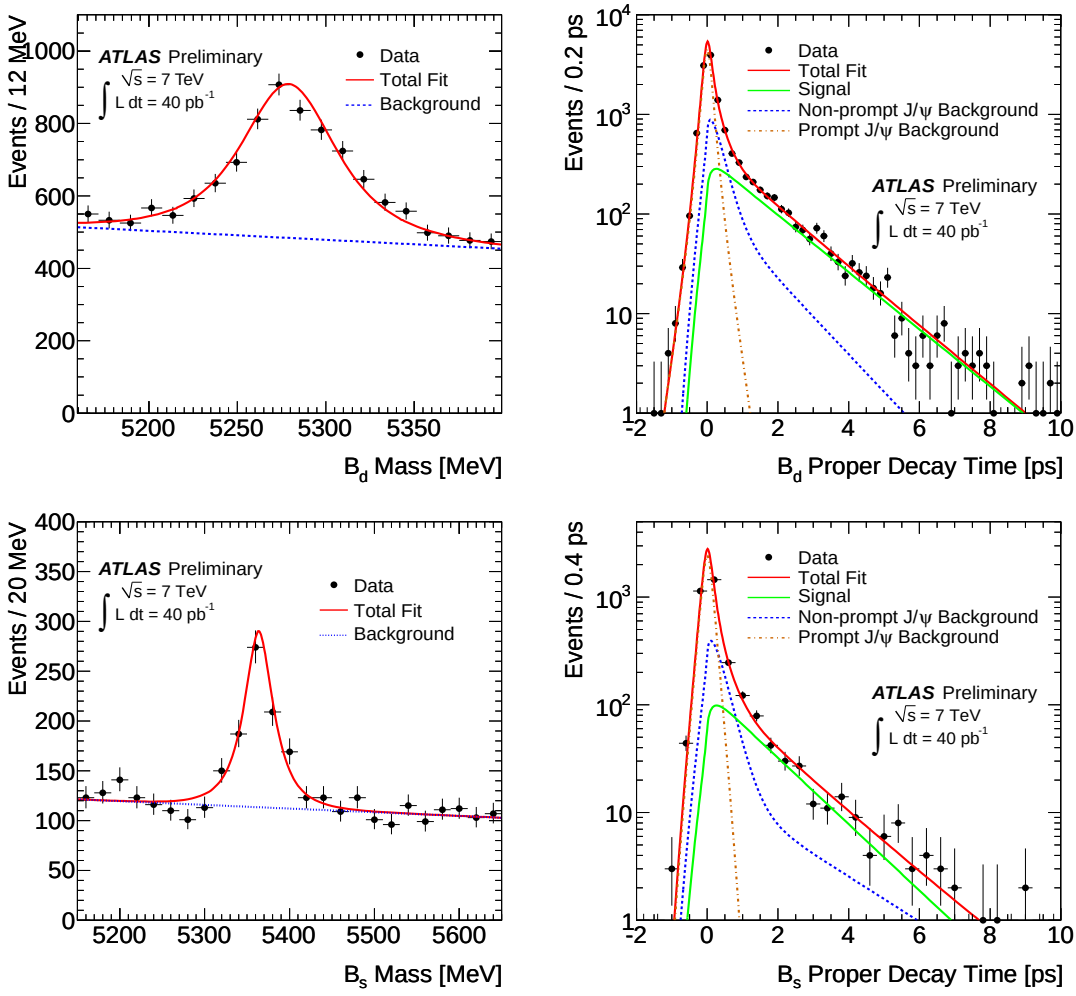

Figure 35: Projections of the simultaneous mass-lifetime unbinned maximum likelihood fits of the B_d^0 (top) and B_s^0 (bottom) data.

References

[1] ATLAS Collaboration, *Measurement of D^* meson production cross sections in pp collisions at $\sqrt{s}$ = 7 TeV with the ATLAS detector*, Tech. Rep. ATLAS-CONF-2011-017, CERN, Geneva, Mar, 2011.

[2] ATLAS Collaboration, G. Aad et al., *Measurement of the differential cross-sections of inclusive, prompt and non-prompt J/ψ production in proton-proton collisions at $\sqrt{s}$ = 7 TeV*, Nucl.Phys. **B850** (2011) 387–444, arXiv:1104.3038 [hep-ex].

[3] ATLAS Collaboration, G. Aad et al., *Measurement of the differential cross-sections of inclusive, prompt and non-prompt J/psi production in proton-proton collisions at sqrt(s) = 7 TeV*, Nucl.Phys. **B850** (2011) 387–444, arXiv:1104.3038 [hep-ex].

[4] ATLAS Collaboration, G. Aad et al., *Observation of a new χ_b state in radiative transitions to $\Upsilon(1S)$ and $\Upsilon(2S)$ at ATLAS*, Phys. Rev. Lett. **108** (2012) 152001, arXiv:1112.5154 [hep-ex].

[5] LHCb Collaboration, R. Aaij et al., *Measurement of $\sigma(pp \to b\bar{b}X)$ at $\sqrt{s} = 7$ TeV in the forward region*, Phys.Lett. **B694** (2010) 209–216, arXiv:1009.2731 [hep-ex].

[6] ATLAS Collaboration, G. Aad et al., *Search for the decay $B_s^0 \to \mu^+\mu^-$ with the ATLAS detector*, arXiv:1204.0735 [hep-ex].

[7] ATLAS Collaboration, *Measurement of the B_d^0 and B_s^0 lifetimes in the decay modes $B_d^0 \to J/\psi K^{0*}$ and $B_s^0 \to J/\psi\phi$ in ATLAS*, Tech. Rep. ATLAS-CONF-2011-092, CERN, Geneva, Jul, 2011.

[8] ATLAS Collaboration, *Measurement of the average B Lifetime in inclusive $B \to JpsiX \to \mu^+\mu^-X$ decays with the ATLAS Detector*, Tech. Rep. ATLAS-CONF-2011-145, CERN, Geneva, Oct, 2011.

[9] A. Ali, T. Mannel, and T. Morozumi, *Forward backward asymmetry of dilepton angular distribution in the decay $b \to sl^+l^-$*, Phys.Lett. **B273** (1991) 505–512.

[10] ATLAS Collaboration, *Time dependent angular analysis of $B_s^0 \to J/\psi\phi$ decay and extraction of $\Delta\Gamma_s$ and the CP violating weak phase ϕ_s in ATLAS*, Preliminary draft (ATLAS members access only), Jun, 2012.

[11] UTfit Collaboration, M. Bona et al., *Constraints on new physics from the quark mixing unitarity triangle*, Phys.Rev.Lett. **97** (2006) 151803, arXiv:hep-ph/0605213 [hep-ph].

[12] CDF Collaboration, A. Abulencia et al., *Observation of B0(s) - anti-B0(s) Oscillations*, Phys.Rev.Lett. **97** (2006) 242003, arXiv:hep-ex/0609040 [hep-ex].

[13] LHCb Collaboration, R. Aaij et al., *Measurement of the B_s^0 - $\bar{B}_s^0$ oscillation frequency Δm_s in $B_s^0 \to D_s^-(3)\pi$ decays*, Phys.Lett. **B709** (2012) 177–184, arXiv:1112.4311 [hep-ex].

[14] A. Lenz and U. Nierste, *Theoretical update of $B_s - \bar{B}_s$ mixing*, JHEP **0706** (2007) 072, arXiv:hep-ph/0612167 [hep-ph].

[15] A. S. Dighe, I. Dunietz, and R. Fleischer, *Extracting CKM phases and $B_s - \bar{B}_s$ mixing parameters from angular distributions of nonleptonic B decays*, Eur.Phys.J. **C6** (1999) 647–662, arXiv:hep-ph/9804253 [hep-ph].

[16] ATLAS Collaboration, W. Armstrong et al., *ATLAS: Technical proposal for a general-purpose pp experiment at the Large Hadron Collider at CERN*, .

[17] ATLAS Collaboration, G. Aad et al., *The ATLAS Experiment at the CERN Large Hadron Collider*, JINST **3** (2008) S08003.

[18] C. Lefevre, *The CERN accelerator complex. Complexe des accelerateurs du CERN*, http://cdsweb.cern.ch/record/1260465, Dec, 2008.

[19] ATLAS Collaboration, G. Aad et al., *Measurement of the Inelastic Proton-Proton Cross-Section at $\sqrt{s} = 7$ TeV with the ATLAS Detector*, Nature Commun. **2** (2011) 463, arXiv:1104.0326 [hep-ex].

[20] S. Catani, M. Dittmar, D. Soper, W. J. Stirling, S. Tapprogge, et al., *QCD*, arXiv:hep-ph/0005025 [hep-ph].

[21] ATLAS Collaboration ATLAS public luminosity results, https://twiki.cern.ch/twiki/bin/view/AtlasPublic/LuminosityPublicResults.

[22] *Updated Luminosity Determination in pp Collisions at root(s)=7 TeV using the ATLAS Detector*, Tech. Rep. ATLAS-CONF-2011-011, CERN, Geneva, Mar, 2011.

[23] ATLAS Collaboration ATLAS public standalone plots, http://www.atlas.ch/photos/index.html.

[24] U. Egede, *The search for a Standard Model Higgs at the LHC and electron identification using transition radiation in the ATLAS tracker*, .

[25] *ATLAS: Detector and physics performance technical design report. Volume 1*, .

[26] ATLAS Collaboration, G. Aad et al., *Expected Performance of the ATLAS Experiment - Detector, Trigger and Physics*, arXiv:0901.0512 [hep-ex].

[27] ATLAS Collaboration, *A measurement of the ATLAS muon reconstruction and trigger efficiency using J/ψ decays*, Tech. Rep. ATLAS-CONF-2011-021, CERN, Geneva, Mar, 2011.

[28] ATLAS Collaboration, *Charged particle multiplicities in pp interactions at $\sqrt{s} = 7$ TeV measured with the ATLAS detector at the LHC*, Tech. Rep. ATLAS-CONF-2010-024, CERN, Geneva, Jul, 2010.

[29] ATLAS Collaboration, *Charged particle multiplicities in p p interactions at $\sqrt{s}$ = 0.9 and 7 TeV in a diffractive limited phase-space measured with the ATLAS detector at the LHC and new PYTHIA6 tune*, Tech. Rep. ATLAS-CONF-2010-031, CERN, Geneva, Jul, 2010.

[30] T. Sjostrand, S. Mrenna, and P. Z. Skands, *PYTHIA 6.4 Physics and Manual*, JHEP **0605** (2006) 026, arXiv:hep-ph/0603175 [hep-ph].

[31] M. Smizanska, *PythiaB an interface to Pythia6 dedicated to simulation of beauty events*, Tech. Rep. ATL-COM-PHYS-2003-038, CERN, Geneva, 2003. (ATLAS members access only).

[32] M. Sevelda, *CP-violation and polarization effects in B-hadron decays. oai:cds.cern.ch:453513*. PhD thesis, Prague Univ., Geneva, 2000.

[33] M. Smizanska and J. Catmore, *EvtGen in ATLAS; rev. version*, Tech. Rep. ATL-COM-PHYS-2004-041, CERN, Geneva, 2004. (ATLAS members access only).

[34] GEANT4 Collaboration, S. Agostinelli et al., *GEANT4: A Simulation toolkit*, Nucl.Instrum.Meth. **A506** (2003) 250–303.

[35] J. Allison, K. Amako, J. Apostolakis, H. Araujo, P. Dubois, et al., *Geant4 developments and applications*, IEEE Trans.Nucl.Sci. **53** (2006) 270.

[36] ATLAS Collaboration, G. Aad et al., *The ATLAS Simulation Infrastructure*, Eur.Phys.J. **C70** (2010) 823–874, arXiv:1005.4568 [physics.ins-det].

[37] ATLAS Collaboration, *Atlas Computing: technical design report*. CERN, Geneva, 2005.

[38] ATLAS Collaboration, C. Anastopoulos et al., *Physics analysis tools for beauty physics in ATLAS*, J.Phys.Conf.Ser. **119** (2008) 032003.

[39] CHEP 2007, http://www.chep2007.com/.

[40] J. M. et al., *Ganga: A tool for computational-task management and easy access to Grid resources*, Computer Physics Communications **180** (2009) no. 11, 2303 – 2316. http://www.sciencedirect.com/science/article/pii/S0010465509001970.

[41] ATLAS Collaboration, T. Maeno, *PanDA: Distributed production and distributed analysis system for ATLAS*, J.Phys.Conf.Ser. **119** (2008) 062036.

[42] https://twiki.cern.ch/twiki/bin/viewauth/AtlasProtected/BPhysWorkingGroupAnalysisAndVertexing (ATLAS members access only).

[43] https://twiki.cern.ch/twiki/bin/view/Atlas/AthenaAwareNTuple (ATLAS members access only).

[44] R. Brun and F. Rademakers, *ROOT: An object oriented data analysis framework*, Nucl.Instrum.Meth. **A389** (1997) 81–86.

[45] V. Kostyukhin, *VKalVrt - package for vertex reconstruction in ATLAS*, Tech. Rep. ATL-PHYS-2003-031, CERN, Geneva, Aug, 2003.

[46] S. Ask, D. Malon, T. Pauly, and M. Shapiro, *Report from the Luminosity Task Force*, Tech. Rep. ATL-GEN-PUB-2006-002, CERN, Geneva, Jul, 2006.

[47] F. Winklmeier, *Real-time configuration changes of the ATLAS High Level Trigger*, Tech. Rep. ATL-DAQ-PROC-2010-009, CERN, Geneva, Jun, 2010.

[48] Particle Data Group Collaboration, K. Nakamura et al., *Review of particle physics*, J.Phys.G **G37** (2010) 075021.

[49] ATLAS Collaboration ATLAS B-physics public standalone plots `https://twiki.cern.ch/twiki/bin/view/AtlasPublic/BPhysPublicResults`.

[50] ATLAS Collaboration, *Observation of the B_d^0 and B_s^0 mesons in the decays $B_d^0 \to J/\psi K^{0*}$ and $B_s^0 \to J/\psi\phi$ in ATLAS*, Tech. Rep. ATLAS-CONF-2011-050, CERN, Geneva, Apr, 2011.

[51] C. Heller, L. Oakes, P. Reznicek, J. Schieck, C. Maiani, J. Catmore, A. Barton, R. Jones, M. Smizanska, and A. Dewhurst, *Observation of the B_d^0 and B_s^0 mesons in the decays $B_d^0 \to J/\psi K^{0*}$ and $B_s^0 \to J/\psi\phi$ in ATLAS: Internal version*, Tech. Rep. ATL-COM-PHYS-2011-202, CERN, Geneva, Feb, 2011. (ATLAS members access only).

[52] Particle Data Group Collaboration, C. Amsler et al., *Review of Particle Physics*, Phys.Lett. **B667** (2008) 1–1340.

[53] CDF Collaboration, T. Aaltonen et al., *Measurement of b hadron lifetimes in exclusive decays containing a J/ψ in $p\bar{p}$ collisions at $\sqrt{s} = 1.96TeV$*, Phys.Rev.Lett. **106** (2011) 121804, `arXiv:1012.3138 [hep-ex]`.

[54] ATLAS Collaboration, *Alignment of the ATLAS Inner Detector Tracking System with 2010 LHC proton-proton collisions at sqrts = 7 TeV*, Tech. Rep. ATLAS-CONF-2011-012, CERN, Geneva, Mar, 2011.

[55] ATLAS Collaboration, *Alignment Performance of the ATLAS Inner Detector Tracking System in 7 TeV proton-proton collisions at the LHC*, Tech. Rep. ATLAS-CONF-2010-067, CERN, Geneva, Jul, 2010.

[56] A. Barton, J. Catmore, A. Dewhurst, C. Heller, R. Jones, C. Maiani, L. Oakes, P. Reznicek, J. Schieck, and M. Smizanska, *Measurement of the B_d^0 and B_s^0 lifetimes in the decay modes $B_d^0 \to J/\psi K^{0*}$ and $B_s^0 \to J/\psi\phi$ in ATLAS*, Tech. Rep. ATL-COM-PHYS-2011-506, CERN, Geneva, May, 2011. (ATLAS members access only).

[57] D0 Collaboration, V. Abazov et al., *Measurement of B_s^0 mixing parameters from the flavor-tagged decay $B_s^0 \to J/\psi\phi$*, Phys.Rev.Lett. **101** (2008) 241801, arXiv:0802.2255 [hep-ex].

[58] CDF Collaboration, T. Aaltonen et al., *An updated measurement of the CP violating phase β_s in $B_s^0 \to J/\psi\phi$ decays using 5.2 fb^{-1} of integrated luminosity*, (2010) . CDF-PUBLIC-10206.

[59] O. Schneider et al., *$B^0 - \bar{B}^0$ Mixing*, J. Phys. G **37** (2010) 075021.

[60] K. Koeneke, *Distributing and storing required data efficiently by means of specifically tailored data formats in the ATLAS collaboration*, Tech. Rep. ATL-SOFT-PROC-2011-036, CERN, Geneva, Jan, 2011.

[61] C. E. et al., *LHC computing Grid: Technical Design Report. Version 1.06 (20 Jun 2005)*. Technical Design Report LCG. CERN, Geneva, 2005.

[62] ATLAS Collaboration, *New ATLAS event generator tunes to 2010 data*, Tech. Rep. ATL-PHYS-PUB-2011-008, CERN, Geneva, Apr, 2011.

[63] A. Coccaro, F. Parodi, and W. Gordon, *Tracking and b-tagging in the ATLAS trigger system. oai:cds.cern.ch:1248681.* PhD thesis, Genoa, Universita' di Genova, Genoa, 2010. Presented on 26 Mar 2010.

[64] S. Tarem, Z. Tarem , N. Panikashvili, O. Belkind, *MuGirl - Muon identification in ATLAS from the inside out*, Nuclear Science Symposium Conference Record, 2007 IEEE **1** (2007) 617–621.

List of Tables

A Appendices of the B_d^0 Observation Study

A.1 Good Run Lists

In order to assure that the offline analysis is run on good quality data, the ATLAS collaboration has developed a system called Good Run List (GRL). The ATLAS data are organized in several levels [47]:

- **Period** - lasting several days, includes several **runs** and typically corresponds to data taking between two technical stops of LHC.
- **Run** - period of data taking with stable detector conditions, usually coinciding to an LHC fill and typically lasts several hours. Each run has an unique number assigned by the data acquisition system.
- **Luminosity Block** - has a length of around 2 minutes and defines an interval of approximately constant luminosity and stable detector conditions. The ATLAS detector configuration (including trigger) is recorded on per-lumiblock basis.

The luminosity blocks are from the data quality point of view the smallest quantities of data. The GRL system thus provides a list of runs and corresponding list of luminosity blocks satisfying selected data quality conditions and detector status. There are number of GRLs for various ATLAS physics-analysis groups, which require good status of different parts of the detector and different functional triggers. For B-physics analyses involving di-muon final state, the muon GRLs are used, which require the ID and magnet systems to have green flags (no problem found) and the muon system to have yellow flag (possible minor issues not affecting the performance) or better. Stable beams have to be declared for all the data. The GRL selections are summarized in table 9, where for each of the 2010 data **periods** a detector and software condition database (COOL) tag is listed together with the muon data quality configuration, allowing to reproduce the list of analyzed **runs** and **luminosity blocks** via a GRL generator page: `https://atlasdqm.cern.ch/grl/`.

2010 Data Period	**COOL tag**	**Configuration**
B	`DetStatus-v03-repro05-01`	`muon yellowPlus 7TeV LBSUM`
C	`DetStatus-v03-repro05-01`	`muon yellowPlus 7TeV LBSUM`
D	`DetStatus-v03-repro05-01`	`muon yellowPlus 7TeV LBSUM`
E	`DetStatus-v03-repro05-01`	`muon yellowPlus 7TeV LBSUM`
F	`DetStatus-v03-repro05-01`	`muon yellowPlus 7TeV LBSUM`
G	`DetStatus-v03-repro05-01`	`muon yellowPlus 7TeV LBSUM`
H	`DetStatus-v03-repro05-01`	`muon yellowPlus 7TeV LBSUM`
I	`DetStatus-v03-repro05-01`	`muon yellowPlus 7TeV LBSUM`

Table 9: Good Run List of the data used for the analysis in section 6. The analysis uses data from a second reconstruction processing where detector alignment was performed on the same 7 TeV (CMS energy) data, while the first processing was done with older alignment based on early 2010 900 GeV data.

A.2 Used Datasets

The output of the ATLAS reconstruction is saved in AOD files - Analysis Objects Data format primarily used for physics analysis [60]. All the available data are reconstructed, the quality selection Good Run List mechanism described in appendix A.1 is applied afterwards during the offline analysis. The AOD files are stored on the world-wide computing grid [61] in datasets grouping the events from each of the data-taking periods. In order to simplify the analyzes between various physics groups, the data are organized several groups called *streams* [26]. The data are directed to the various *streams* depending on which triggers accepted the particular event. For the B_d^0 observation study, the following real-data datasets corresponding to the *muon stream* were used (unique LHC grid names):

data10_7TeV.periodB.physics_MuonswBeam.PhysCont.AOD.repro05_v02/
data10_7TeV.periodC.physics_MuonswBeam.PhysCont.AOD.repro05_v02/
data10_7TeV.periodD.physics_MuonswBeam.PhysCont.AOD.repro05_v02/
data10_7TeV.periodE.physics_Muons.PhysCont.AOD.repro05_v02/
data10_7TeV.periodE.physics_Muons.PhysCont.AOD.repro05_v02a/
data10_7TeV.periodF.physics_Muons.PhysCont.AOD.repro05_v02/
data10_7TeV.periodG.physics_Muons.PhysCont.AOD.repro05_v02/
data10_7TeV.periodH.physics_Muons.PhysCont.AOD.repro05_v02/
data10_7TeV.periodI.physics_Muons.PhysCont.AOD.repro05_v02/

The Monte Carlo datasets used for the cuts selection and study of contributions of fake B_d^0 candidates are listed here (see also table 1):

mc10_7TeV.108524.PythiaB_Bd_Jpsi_mu2p5mu2p5_K0star.merge.AOD.e598_s933_s946_r1830_r1700/
mc10_7TeV.108523.PythiaB_bb_Jpsimu2p5mu2p5X.merge.AOD.e598_s933_s946_r1830_r1700/
mc10_7TeV.108494.Pythia_directJpsimu2p5mu2p5.merge.AOD.e574_s933_s946_r1662_r1700/

The MC events generated by Pythia were filtered to accept only those that contain two muons with at least 2.5 GeV transverse momentum. This was done to avoid CPU-expensive reconstruction of events that would be mostly rejected by the offline analysis due to low muon-reconstruction efficiency of such low-p_{T} muons. The signal $B_d^0 \to J/\psi(\mu^+\mu^-)K^{*0}(K^+\pi^-)$ decay was simulated by Pythia and thus not taking into account the helicity structure generating non-flat angular distribution. Details about Pythia parameters tunning for the MC10 and MC11 simulation campaigns can be found in [28, 29, 62].

A.3 Full List of Triggers Accepting the Selected B_d^0 Candidates

The full list of triggers collecting events with offline-selected B_d^0 candidates (see section 6) is shown in this appendix. The trigger decisions are divided into several groups in order to distinguish events picked up by B-physics triggers dedicated for the search of the $B_d^0 \to J/\psi K^{*0}$ decays from more general muon triggers (for details about the algorithms of the main B-physics triggers (topological, *TrigDiMuon* and muon+track trigger) see section 3.1):

Fraction of B_d^0 events collected by the primary B-physics triggers devoted for search for J/ψ signature:	64 %
`EF_mu4_Jpsimumu`, `EF_2mu4_Jpsimumu`	

By adding the muon+track trigger, the Full-Scan (tracking in full ID volume) variants of the *TrigDiMuon* trigger and the same topological and *TrigDiMuon* triggers with wide $\mu^+\mu^-$ invariant mass window, the fraction of triggered B_d^0 events is enhanced by:	12 %
`EF_mu4_Trk_Jpsi`, `EF_mu4_DiMu_FS`, `EF_mu4_Jpsimumu_FS`, `EF_mu4_DiMu`, `EF_2mu4_DiMu`	

In the very first data periods the luminosity was relatively low allowing for lowest-p_{T} single muon triggers to be unprescaled. Therefore these are also giving significant fraction of B_d^0 events by recovering candidates with one of the two muons seen only offline but not on trigger level. The fraction added by these triggers add w.r.t. the previous trigger list is:	4 %
`L1_MU0` (only up to run 158392), `EF_mu4`, `EF_mu6`	

Out of the remaining 20 % B_d^0 events, great part was triggered by various B-physics supporting and calibration triggers:	9 %
(trigger names sorted from the highest contribution) `EF_MU4_DiMu_FS`, `EF_mu4_DiMu_MG_FS`, `EF_mu4_DiMu_noOS`, `EF_mu4_DiMu_SiTrk`, `EF_mu4_Jpsimumu_SiTrk_FS`, `EF_MU4_DiMu`, `EF_mu4_Trk_Upsi_FS`, `EF_mu6_DiMu`, `EF_mu4_Upsimumu_FS`, `EF_mu4_DiMu_FS_noOS`, `EF_MU4_DiMu_MG_FS`, `EF_mu4_BmumuX`, `EF_2mu4_DiMu_noVtx_noOS`, `EF_mu4_Trk_Upsi_loose_FS`, `EF_MU4_DiMu_FS_noRoI`, `EF_2mu4_DiMu_SiTrk`, `EF_mu4_DiMu_SiTrk_FS`, `EF_mu4_Trk_Jpsi_loose`, `EF_MU4_DiMu_FS_noOS_passL2`, `EF_2mu4_DiMu_noVtx`, `EF_MU4_Trk_Upsi_loose_FS_passL2`, `EF_mu4mu6_DiMu`, `EF_MU6_Trk_Jpsi_loose_FS`	

Another set of events comes from triggers in pass-trough mode (at Event Filter level), effectively making decision at trigger level L2. These are mostly B-physics L2 triggers in the pass-through mode. The triggered fraction is:	2 %
(trigger names sorted from the highest contribution) EF_mu4_Jpsimumu, EF_mu4_DiMu_MG_FS, EF_mu4_Trk_Jpsi, EF_MU4_DiMu_FS, EF_mu4_DiMu_SiTrk, EF_mu4_BmumuX, EF_mu4_Upsimumu_FS, EF_mu4_DiMu_FS_noOS, EF_mu4_Trk_Upsi_loose_FS, EF_2mu4_DiMu, EF_mu4mu6_Jpsimumu, EF_2mu4_DiMu_noVtx_noOS, EF_mu4_Trk_Jpsi_loose, EF_mu4_DiMu_SiTrk_FS, EF_MU4_DiMu, EF_mu4_DiMu_FS, EF_mu4_DiMu, EF_mu4_Trk_Upsi_FS, EF_MU4_DiMu_FS_noOS, EF_MU4_DiMu_FS_noRoI, EF_mu4_DiMu_noOS, EF_MU4_DiMu_SiTrk_FS, EF_mu6_DiMu, EF_mu4_Jpsie5e3_FS, EF_mu20_slow	

Except few events, the remaining B_d^0 events were collected by single muon triggers not specifically aiming on J/ψ signature:	9 %
(trigger names sorted from the highest contribution) EF_mu13_tight, EF_2mu6_MG, EF_mu4_MSonly, EF_mu10i_loose, EF_mu0_outOfTime2, EF_mu4_Jpsie5e3, EF_mu0_rpcOnly, EF_mu10_MG, EF_mu4_MV, EF_mu0_missingRoi, EF_2mu4, EF_2mu0_NoAlg, EF_2mu6_NoAlg, EF_e10_loose_mu6, EF_mu10_MSonly_tight, EF_mu4_MSonly_outOfTime, EF_mu4_muCombTag, EF_2mu10_NoAlg, EF_mu6_Jpsie5e3_FS, EF_mu15_NoAlg, EF_mu13_MG, EF_mu0_outOfTime1, EF_mu4_MG, EF_L1ItemStreamer_L1_MU0_EM3, EF_2mu6, EF_mu6_muCombTag, EF_mu4_tile, EF_mu4_Jpsie5e3_SiTrk_FS, EF_mu20_passHLT, EF_mu6_IDTrkNoCut, EF_mu40_MSonly, EF_L1ItemStreamer_L1_MU0, EF_mu4_IDTrkNoCut, EF_mu10_IDTrkNoCut, EF_mu4_L1J5_matched, EF_mu4_L2MSonly_EFFS_passL2, EF_mu0_comm_NoAlg, EF_mu4_MSonly_MB2_noL2_EFFS, EF_mu10_tight, EF_mu6_MSonly, EF_mu20_NoAlg, EF_mu6_NoAlg, EF_mu4_j20_jetNoCut, EF_mu6_SiTrk, EF_e5_medium_mu4, EF_L1ItemStreamer_L1_MU0_J5, EF_mu4_L1J30_matched, EF_mu4_Jpsie5e3_FS, EF_mu6_MG, EF_mu6_MSonly_outOfTime, EF_mu13_MG_tight, EF_L1ItemStreamer_L1_2MU0, EF_mu10_NoAlg, EF_mu4_MSonly_EFFS_passL2, EF_mu10_MSonly, EF_mu20_MSonly, EF_mu0_NoAlg, EF_2MUL1_l2j30_HV, EF_mu6_passHLT, EF_mu4_mu6, EF_2mu10, EF_mu4_passHLT, EF_mu30_MSonly, EF_mu6_MSonly_MB2_noL2_EFFS EF_mu4_SiTrk	

Non-muon triggers fraction collecting the few last events:	$< 0.1\,\%$
EF_xe20_tight_noMu, EF_tau12_loose_EFxe12_noMu, EF_j50_jetNoCut, EF_tauNoCut_hasTrk6_EFxe15_noMu, EF_g17_etcut, EF_e20_loose_passEF, EF_2e3_medium_SiTrk, EF_tau12_loose_xe20_noMu, EF_te300_loose, EF_2j35_jetNoEF_xe30_noMu	

The configuration of the B-physics supporting and calibration triggers can be determined from the particular name of the given trigger decision. The following list explains the most common abbreviations:

- `2muX` **or** `muXmuY` / `muX` / `muX_Trk` - defines the B-physics trigger algorithm: topological / *TrigDiMuon* / muon+track. The **X** (and **Y**) value determines the muon p_{T} threshold(s) (in GeV).

- `mu` / `MU` - the capital "`MU`" refers to that there is no muon confirmation at trigger level L2 and thus the p_{T} threshold is coming from less precise measurement at L1, providing less stringent constraint on the muon identification and the p_{T} threshold.

- `Jpsi(mumu)` / `Upsi(mumu)` / `Bmumu` / `DiMu` - defines the $\mu^+\mu^-$ invariant mass window: J/ψ region $(2.5-4.3)$ GeV, Υ region $(8-12)$ GeV, B-hadron region $(4.0-8.5)$ GeV or full range $(1.5-14.0)$ GeV.

- `BmumuX` - identifies trigger algorithm devoted for semiletonic rare B-decays.

- `FS` - full-scan type of *TrigDiMuon* or muon+track trigger, allowing to find J/ψ candidates constructed from tracks in the whole Inner Detector instead of just in the L1 muon region of interest (which is default option of the algorithms). Thus accepting J/ψ candidates with very large opening angles.

- `noOS` - the muon tracks forming the J/ψ candidate are not requested to have opposite charge. This is useful to control the background level of the J/ψ triggers.

- `noVtx` - the muon tracks forming the J/ψ candidate are not requested to pass vertex fitting (in the trigger level L2 algorithm only, EF vertexing is always performed). The trigger is devoted for the study of possible bias coming from the vertexing at trigger level.

- `SiTrk` - uses alternative tracking algorithm *SiTrack* instead of default *IDSCAN* (trigger tracking nicely summarized in [63]).

- `MG` - uses alternative muon reconstruction algorithm [64].

- `loose` - softer cuts in the particular trigger (lower p_{T} threshold of the second muon or wider mass window).

- `passL2` - the decision at trigger level L2 is ignored and the event is always passed for further processing.

It should be noted that due to usually high output rates of the supporting and calibration triggers (because of the softer cuts), these trigger were always heavily prescaled or were active only during the very first data taking periods when instantaneous luminosity was low.

B Appendices of the B_d^0 Lifetime Measurement

B.1 Proper Decay Time Range Dependence

The selection of the B_d^0 candidates used to measure the B_d^0 lifetime via simultaneous mass-lifetime fit did not include any cut on the proper decay time τ_i. To probe validity of the model in the full τ_i range, the simultaneous mass-lifetime fit was performed in five τ_i windows. The dependence of the fit results on the selected τ_i range is shown in figures 36. The fitted B_d^0 mass and lifetime were found to be stable. However the τ_i range including only positive proper decay times is not able to properly determine the δ_{τ_i} errors scale factor as part of the prompt-J/ψ induced B_d^0 candidates is included in the fast decaying background exponential.

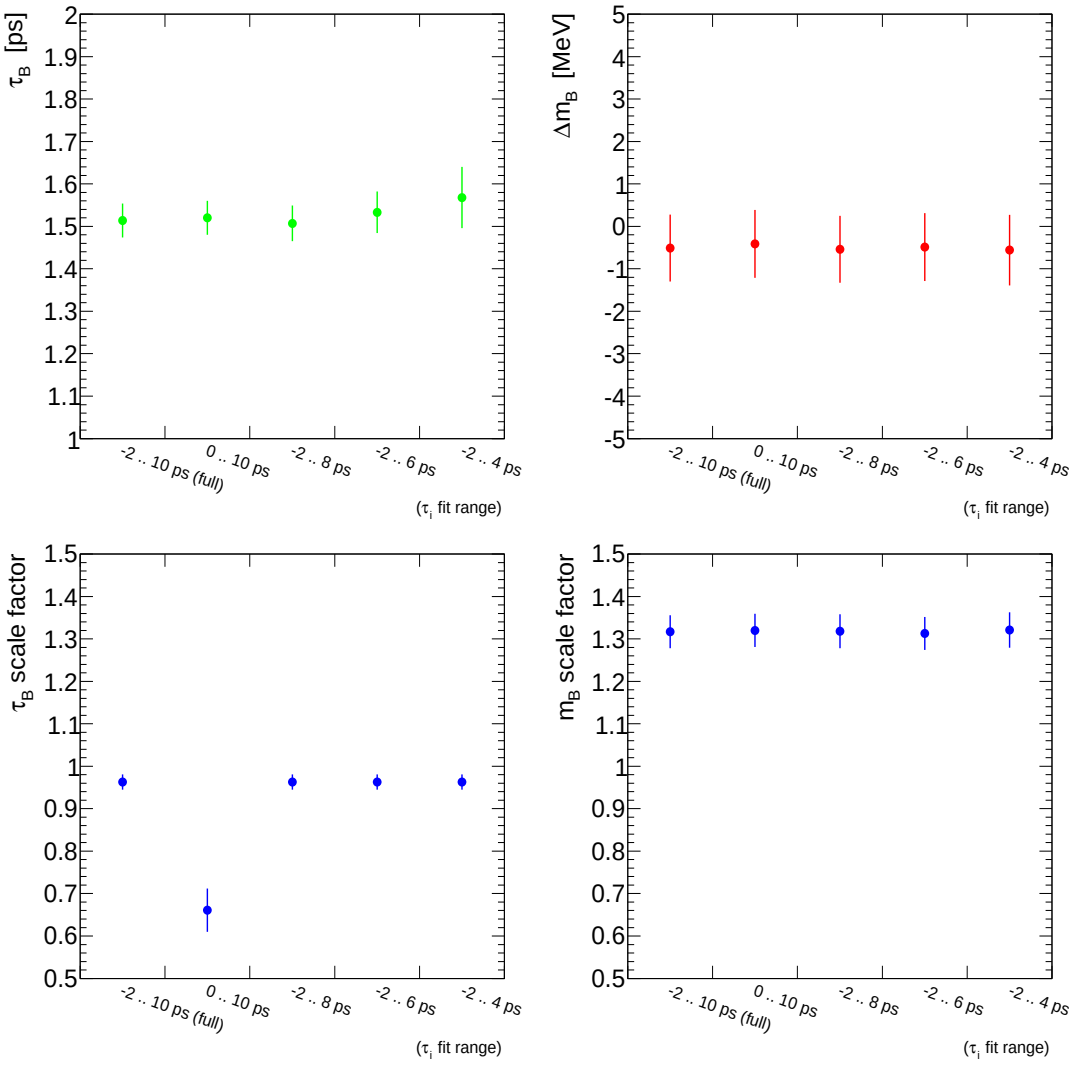

Figure 36: Variations of the fit results with the choice of the B_d^0 proper decay time window. The fitted B_d^0 lifetime is shown on the top left figure, the invariant mass (relative to the world average value $M_{\mathrm{PDG}}(B_d^0) = 5279.5 \pm 0.5$ MeV) on the top right. The bottom figures shows the stability of the mass (right) and proper decay time (left) error scale factors.

B.2 Fit Robustness with B_d^0 Vertex Quality Cut

This section presents the variations of the simultaneous mass-lifetime fit results with the quality cut on the B_d^0 candidates 4-track vertex. Table 10 shows the main fitted parameters for several vertex χ^2/n.d.o.f. cuts. The maximum observed difference of 0.03 ps. However, the quality of the 4-tracks vertex is connected with the per-candidate mass and proper decay time errors and with the used assumption that the distributions are the same for signal and background events. A systematic error assigned to that assumption was already evaluated in section 7.3.3 and the above difference is highly correlated with it. Therefore does not need to be included in the total systematic uncertainty of the B_d^0 lifetime measurement.

B_d^0 vertex χ^2/n.d.o.f. cut	τ_B [ps]	m_B [MeV]	f_{sig}	N_{sig}
1.8	1.480 ± 0.040	5278.97 ± 0.79	0.238 ± 0.007	2530 ± 79
2.0	1.497 ± 0.039	5278.65 ± 0.78	0.234 ± 0.007	2625 ± 81
2.5	1.513 ± 0.040	5278.93 ± 0.79	0.222 ± 0.007	2758 ± 88
3.0	1.511 ± 0.040	5278.98 ± 0.79	0.213 ± 0.007	2816 ± 92

Table 10: Table of the main mass-lifetime fit-results for different selection on the B_d^0 vertex quality. (The results for the default χ^2/n.d.o.f. < 2.5 cut are slightly different from the main document because of using tighter B_d^0 mass window in this particular study).